NTNU

Norwegian University of
Science and Technology

Clustering during Natural Aging and its Effect on Precipitation Hardening in Al-Mg-Si Alloys

Fredrik Aleksander Martinsen

Master of Science in Physics and Mathematics
Submission date: June 2011
Supervisor: Randi Holmestad, IFY

Norwegian University of Science and Technology
Department of Physics

Abstract

The effect of clustering during natural aging of three different Al-Mg-Si alloys with equal Mg/Si-ratios, but different Mg+Si contents have been studied through hardness measurements and transmission electron microscopy (TEM). Hardness measurements were performed both during natural aging (NA) and after various NA times followed by subsequent artificial aging for all alloys, while TEM-investigations were performed on selected samples. The results from the experiments were compared and the existence of three different clustering processes were discovered. The first process was established to be Si-Si clustering causing a slight hardness increase during natural aging and a strong hardness increase after subsequent artificial aging. The second process was found to be Mg-Mg clustering causing a significant hardness increase during natural aging, and a clear decrease in hardness after subsequent artificial aging. The third process was found to be Mg-Si clustering and simultaneous transformation of mono-clusters into co-clusters. This combined process causes a hardness increase both during natural aging and after subsequent artificial aging. The hardness increase is caused by a refinement of alloy microstructure including a higher number of smaller β" needles. This precipitate type was observed for all alloys and conditions. The negative effect of Mg-Mg clusters on precipitation hardness is suggested to be related to the repulsion of Si from these clusters. This hinders the co-clustering of Mg and Si in the areas surrounding these clusters.

Preface

This master's thesis was written during the spring of 2011 as the conclusion of my master's degree in applied physics at the Norwegian University of Science and Technology, NTNU. The experimental work was performed at the Department of Physics and at the department of Material Science and Engineering. The thesis was carried out at the division of condensed matter physics with professor Randi Holmestad as main supervisor.

This thesis is a continuation of my project thesis written during the autumn of 2010. Some of the results and other content presented in that thesis are also presented here in order to create an adequate coherence in the total presentation of the performed work. I also choose to include a rather detailed theory chapter in order to make a brief guide for future students performing similar work. Instead of spending a lot of time looking for information in the literature, they can now read this thesis as an introduction to the field.

I would like to thank my day-to-day supervisors Flemming Ehlers and Malin Torsæter for their guidance and our valuable discussions throughout this period, Bjørn Soleim and Calin Marioara for TEM-training and coaching, and Sigurd Wenner for the production of the software used in the analyis of TEM-images. Finally I would like to thank my main supervisor Randi Holmestad for her support and enthusiasm.

Trondheim, June, 2011

Fredrik Aleksander Martinsen

List of Abbreviations

3DAP - Three Dimensional Atom Probe
AA - Artificial Aging
AC - Atomic Cluster
APT - Atom Probe Tomography
CS - Cross Section
DFT - Density Functional Theory
DP - Diffraction Pattern
EDS - Energy Dispersive Spectroscopy
EELS - Electron Energy Loss Spectroscopy
EM - Electron Microscopy
FEG - Field Emission Gun
GP - Guinier-Preston
HS - High Solute
HV1 - Vickers Hardness at 1 kg load
LS - Low Solute
MS - Medium Solute
NA - Natural Aging
HRTEM - High Resolution Transmission Electron Microscopy
PEELS - Parallel Electron Energy Loss Spectroscopy
RT - Room Temperature
SAD - Selected Area Diffraction
SHT - Solution Heat Treatment
SSSS - Super Saturated Solid Solution
TEM - Transmission Electron Microscope
TLM - Transmission Light Microscope
VF - Volume Fraction
WDS - Wavelength Dispersive X-Ray Spectroscopy
wt% - Weight percent
ZLP - Zero-loss Peak

Contents

Chapter 1

Introduction

"Once upon a time, a goldsmith was given the privilege of meeting emperor Tiberius of Rome. The goldsmith wanted to show the emperor a dinner plate he had made out of a new and valuable metal. The metal he claimed to have made from plain clay and assured the emperor that only he knew the secret of extracting it. Afraid that the gold and silver in the vaults of Rome would loose value, the emperor ordered the goldsmith decapitated in fear of this new metal."

This story is based on a reference to what is believed to be aluminum, reported by Pliny the Elder in the first century AD [1]. Even with its validity greatly doubted, it makes one imagine what the world would be like if mankind got familiar with aluminum at that time. As knowledge of materials always have been crucial for the development of civilization, it is likely that the world would have been quite a different place.

Of all kinds of materials, metals are namely of the most widely used in todays society. Most of the common metals are relatively cheap to produce, and they may be used in a vast amount of applications such as buildings, street lighting poles, beverage cans, boats, planes, etc. This huge field of applications makes the development of metals into a big business, driven forward by the demand of increased functionality, lighter weight and higher strength. In particular with a growing concern about the worlds demand of energy, an increasing effort is currently made to produce light metals that may substitute heavy metals in many energy demanding application. One of the most up-and-coming light-weight metals for this purpose is aluminum in the form of aluminum alloys.

Aluminum (Al): The use of aluminum in the form of Al-alloys has been increasing rapidly during the last years mainly due to their high strength to weight ratio, resistance against corrosion and easy workability [2]. Since Al-alloys are so-called light weight alloys, they are constantly developed with the purpose of reducing the weight of certain applications by replacing heavier metals such as steels. For example the substitution of steels with aluminum in devices like cars and aeroplanes has contributed to an enormous reduction in emission from the the transport section and reduced the worlds consumption of fossil fuels. Aluminum alloys are not only strong compared to weight, but they are also very easy to recycle. Recycling require only 5% of the originally energy required to produce it, and Al-alloys have become popular in many disposable consumer products such as packaging, beverage cans and wrapping foils [3]. Due to their great ability to be recycled, as much as 75% of all the aluminum ever produced is still in use!

However with all their qualities, there are some problems with aluminum alloys that strongly restrict their field of application. For some purposes it is required from the material that its strength is above a certain limit and that it can withstand harsh conditions without getting its properties altered. Even though Al-alloys have a great strength to weight ratio, their maximum strength is still far lower than that of steels. Another weakness is that Al-alloys get their strength strongly reduced when being exposed to temperatures of only a few hundred degrees Celsius. With a lasting exposure to such high temperatures, the properties of the alloy will get altered and it will greatly loose its strength [4]. For such applications where aluminum alloys do not fulfill the requirements, metals like steels are still commonly used.

Precipitation: In the beginning of the 20^{th} century some aluminum alloys were discovered to display a significant hardness increase when being heat treated [5]. This motivated the exploration of different heat treatments that could alter their physical properties. In the recent years it has been discovered that the increase in strength due to these heat treatments is caused by small nano-sized particles called precipitates. They have later been the subject of numerous studies and several classifications of different precipitates for different alloying systems has been discovered. A typical alloy heat treatment is typically divided into three steps: (i) solution heat treatment (SHT) at high temperatures, (ii) natural aging (NA) at room temperature and (iii) artificial aging (AA) at medium intermediate temperatures [2]. During the artificial aging, the precipitates that result in the greatest strength are formed. Because of their great effect on hardness, these precipitates has been the subject to numerous studies during the last decades and our knowledge about them is rapidly increasing.

Natural aging was long assumed to have insignificant effect on the physical properties of the alloy compared to that of AA. It was only considered because it was inevitable due to the difficulties of moving huge amounts of metal from one oven to another during industrial production. In the later years however it has been discovered that the small nano-sized atomic clusters formed during this natural aging actually affects the final properties of the alloy after AA [6]. Even though we have been able to study the effect of the clusters on the physical properties of the alloy, we have not been able to study their atomic composition until recently. The problem has been that the clusters are coherent and too small to be studied in conventional TEM and hence require more sophisticated experimental techniques to be detected. However with the approach of techniques like atom probe tomography and positron annihilation spectroscopy, it is now possible to perform experimental studies of cluster sizes and compositions [7][8].

Atomic structures in condensed matter can also be investigated theoretically. With the rapidly increasing power of computers, it is now possible to perform detailed simulations on atomic structures and predict properties that are still not possible to investigate experimentally.

Scope of project: The scope of this project is to further investigate this concept of natural aging and its effects on three different Al-Mg-Si alloys both before and after artificial aging. The process of clustering itself will be investigated through hardness measurements of the selected alloys during natural aging. Further will the effect of NA on the final alloy hardness after AA be investigated, and a comparison of hardness before and after AA will hopefully result in some information about the effect of clustering. A detailed study of the microstucture of two of the three alloys will be performed using conventional TEM, where measurements of precipitate number density, average length, cross section and volume fraction will be made. Different samples naturally aged for different amounts of time will be studied in order to investigate the effect which the clustering has on the final microstructure of the different alloys. The investigation will be a continuation of the work earlier done by the author where hardness measurements were performed together with DFT calculations [9].

Chapter 2

Theory and Background

In this chapter, all information necessary to understand the later presented results and the applied method is presented. The chapter is written rather detailed in order to act as a introduction to the field for future students.

2.1 Aluminum

2.1.1 History of Aluminum

Aluminum (Al) is the third most common element in the earth's crust, but was not discovered as an atomic element until the discovery of bauxite in 1821 in Les Baux, France [10]. Rather than to exist in nature in its pure form it is found as aluminum oxide Al_2O_3 in different minerals with the reddish stone Bauxite as the most common one. It was first produced in its pure form in the late 1820's and remained an exclusive metal far more expensive than gold until the late 1800's. A known story is that the Emperor of France, Napoleon III, once invited to a banquet where the emperor's family and the most honored guests where given the privilege of eating from aluminum plates while the guests of lower ranks had to manage with gold. The age when pure aluminum was a precious metal ended in 1886 with the discovery that pure aluminum could be produced industrially from Al_2O_3 by electrolysis. Even though the methods from then are slightly changed, electrolysis still remains the principal method for producing pure aluminum. Today, however we have the possibilities of producing far more wast amounts of it.

Aluminum in its pure form is in general very soft and has none or few practical applications. However it was discovered that by adding small amounts of other elements to the metal, making an alloy, its strength strongly increased. Today the hardness of a typical aluminum alloy actually scales like $\sim$10 compared to the hardness of pure aluminum, and this has made Al-alloys to one of the most common materials used in everyday life.

2.1.2 Applications

Aluminum is what is called a lightweight metal with a density of 2700 kg/m^3 compared to eg. steel which has a density of 7800 kg/m^3 [2]. Even though it doesn't have the same strength as steel it has a higher strength-to-weight ratio which makes it suitable for many lightweight applications in eg. cars and airplanes. In addition to the high strength to weight ratio aluminum in the form of Al-alloys has many other excellent properties. These includes high electrical and thermal conductivity, high resistance to corrosion, no ductile to brittle transformation at low temperatures, easy shapeability and low energy amounts needed for recycling. With an energy demand for recycling of only $\sim$ 5% of the energy required to make it, Al-alloys are greatly used in different consumer articles such as packaging like in beverage cans [2].

However, despite of all its advantages, Al-alloys have some weaknesses that confines their areas of application. Their low endurance limit, low hardness compared to steel and a melting point of only $\approx 660^\circ$ make them unsuitable for many applications. For example certain parts of a car needs to be strong to withstand high forces, and hence need a strength higher than what can be obtained by Al-alloys. Improving today's Al-alloys so that they can overcome some of the mentioned weaknesses would be of great industrial significance. It would allow AL-alloys to substitute steels in a higher number of applications, meaning that great environmental advantages could be achieved.

2.1.3 Alloy types

When talking about alloys in general one refers to all possible mixings of aluminum with other elements. Since there are many different alloys, a system for classifying them are needed. Aluminum alloys can most roughly be sorted be into the two groups *wrougth* and *casting* alloys, depending on the way they are fabricated. Within these two groups, the alloys have their own designation system which sorts them

into different subgroups. They are sorted by using the labeling yxxx for wrought alloys and yxx.x. for casting alloys. For wrought alloys y denotes the main group of alloying elements and the remaining numbers xxx denote the modification and amount of alloying elements. The same applies for the casting alloys only that here the last digit stands for the product form. A complete overview of the different types of alloys are found in table 2.1.

In addition to the numbering system, all aluminum alloys can be divided into to two groups dependent on whether they are heat treatable [1] or non-heat treatable. By heat treatable one means that the alloy can be exposed to elevated temperatures for different amount of time to alter their atomic structure.

Table 2.1: The table is showing the designation system of aluminum alloys where the designation yxxx for wrought alloys and yxx.x. for casting alloys are related to alloying elements and whether the alloys are age-hardenable or not [2].

Wrought Alloys		
1xxx	Pure Al ($<$ 99%Al)	Not age-hardenable
2xxx	Al-Cu and Al-Cu-Li	Age-hardenable
3xxx	Al-Mn	Not age-hardenable
4xxx	Al-Si and Al-Mg-Si	Age-hardenable
5xxx	Al-Mg	Not age-hardenable
6xxx	Al-Mg-Si	Age-hardenable
7xxx	Al-Mg-Zn	Age-hardenable
8xxx	Al-Li, Sn, Zr or B	Age-hardenable
9xxx	Not currently used	
Casting Alloys		
1xx.x.	Pure Al ($<$ 99%Al)	Not age-hardenable
2xx.x.	Al-Cu	Age-hardenable
3xx.x.	Al-Si-Cu or Al-Mg-Si	Some are age-hardenable
4xx.x.	Al-Si	Not age-hardenable
5xx.x.	Al-Mg	Not age-hardenable
6xx.x.	Not currently used	
7xx.x.	Al-Mg-Zn	Age-hardenable
8xx.x.	Al-Sn	Age-hardenable
9xx.x.	Not currently used	

[1] Also referred to as age hardenable.

2.2 Strength of metals

Assume that you want to calculate the strength of a metal from an atomistic point of view. A reasonable approach would be to combine inter-atomic bonding energies with the crystal structure of the metal, and then sum up to get an estimate of the bulk strength. You would be surprised by the result of such a calculation, as the predicted strength is between 10^3 and 10^4 times higher than the actual physical strength of the metal [2]. Why is it so? How can the strength of the metal be so much smaller than the one calculated from its atomic bonding? To understand this, it is necessary to understand the concepts of dislocations and slip.

2.2.1 Dislocations

A dislocation can be interpreted as a line defect or imperfection in an otherwise ideal crystal. Dislocations are defined as one-dimensional and exist in two forms; line dislocations and screw dislocations.

Line dislocations A line dislocation exists when a crystallographic half-plane is introduced into or removed from the crystal structure, followed by a rebonding of the atoms close to the termination interface of this plane. A schematic drawing of a line dislocation is shown in figure 2.1a where the lower part of the central upper half plane is what defines the dislocation. If you go in equal numbers of atomic distances in a loop around the dislocation, you will find yourself in an atomic position different from the one you started at. The vector from the termination point to the starting point is called Burgers vector and is denoted as **b**. A line dislocation can be defined by this Burgers vector as it lies in the same plane as the path of propagation around the dislocation [2]. A visualization of this looping can be seen in figure 2.1a. Starting in position 1 before traveling around the dislocation by taking one step in every direction will lead you to position 5. To complete the loop, you must take one extra step to the right which defines the burgers vector.

Screw dislocation A screw dislocation can be visualized by a perfect crystal that have been sliced halfway though and then "screwed" to move the atomic bonding one crystal spacing. In other words the screwing is as shearing of each side of the cut in opposite directions. In this case, the burgers vector is not in the plane of propagation as with the line dislocation, but perpendicular to it [2]. This can be seen in figure 2.1b where the vector from point 5 to 1 lies perpendicular to the plane of propagation.

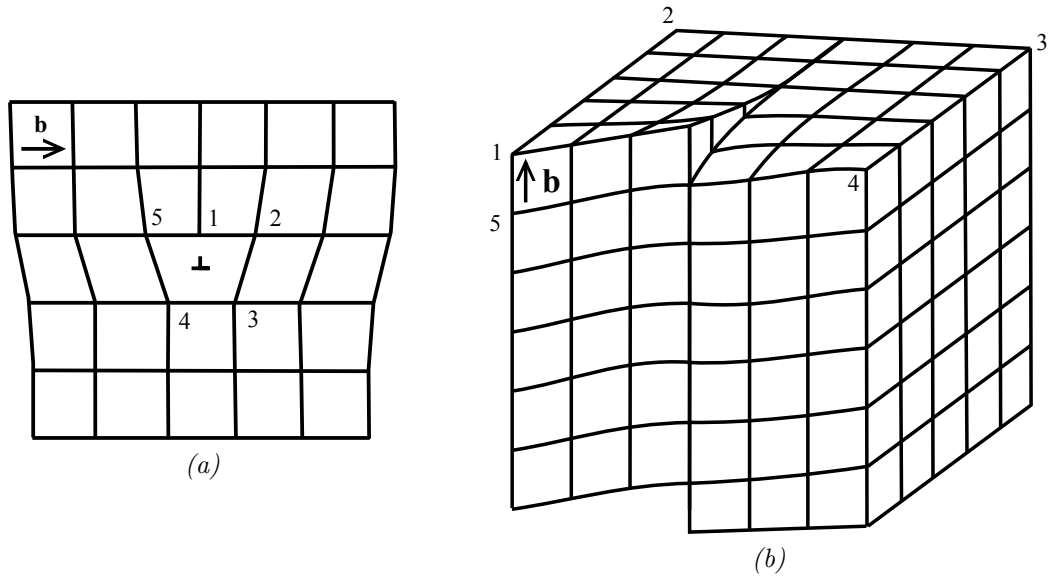

Figure 2.1: Illustrations of a line dislocation (a) and a screw dislocation (b). In the case of the line dislocation, Burgers vector can be seen to lie in the same plane as the plane 1 → 5, while it lies perpendicular to it in the case of the screw dislocation.

2.2.2 Slip

Dislocations are not stationary, but may move through the process called slip. The process happens in the direction of burgers vector for line dislocations and in the direction perpendicular to burgers vector for screw dislocations. The direction of motion is always called the slip direction, and together with the slip-plane formed by the dislocation itself and burgers vector, it makes up the so-called slip system.

Slip may be easily visualized through the motion of a line dislocation. For the dislocation to jump one atomic spacing in the direction of burgers vector, only a single column of atomic bonds has to be broken at any one time. After the breaking of the bonds, the dislocation is transfered to the neighboring column where new

bonds are created. This way the dislocation may move out of the system by breaking only one column of bonds at the time rather than all at once. It is this simple fact that explains why metals are not as strong as expected from their inter-atomic bonding energies.

For slip to happen, the local stress has to exceed the so-called Peierls-Nabaro stress τ given by the relation (2.1) [2];

$$\tau = c \cdot \exp(-kd/b) \tag{2.1}$$

Here c and k are constants specific to the metal, d is the inter-planar distance between two neighboring slip planes and b is the magnitude of burgers vector. The latter is important to keep in mind when discussing interference with dislocation movement.

2.2.3 Particle coherency

To understand later sections about precipitation hardening, it is necessary to be familiar with the concepts of *coherency*. Coherency can be understood by considering a particle of one phase dispersed in a matrix of another phase. Its fit with the host matrix may be described through what is defined as coherency. It is common to divide the degree of coherency into four groups, according to how well the dispersed phase fits in [11].

Fully coherent: The dispersed particle is said to be fully coherent if it fits perfectly with the host matrix in terms of crystal structure and lattice parameter. In other words, the atoms in the particle fills already existing lattice points in the host matrix (figure 2.2a).

Coherent: The dispersed particle is said to be coherent if it fits perfectly into the host matrix apart from a small variation in lattice parameter. This difference in lattice parameter causes a so-called coherency strain in the host matrix to get the particle to fit in (figure 2.2b).

Partially coherent: The dispersed particle is said to be partially coherent if it has interfaces with different coherency. This can be seen in figure 2.2c where there is fully coherency between the planes in the y-direction while there is coherency between the planes in the x-direction.

Incoherent: The dispersed particle is said to be incoherent if it does not fit with the host matrix at all. The host matrix will therefore be unstrained as the crystal structure of the dispersed phase is so different from the host lattice, that a coherency is unobtainable even through coherency strain (figure 2.2d).

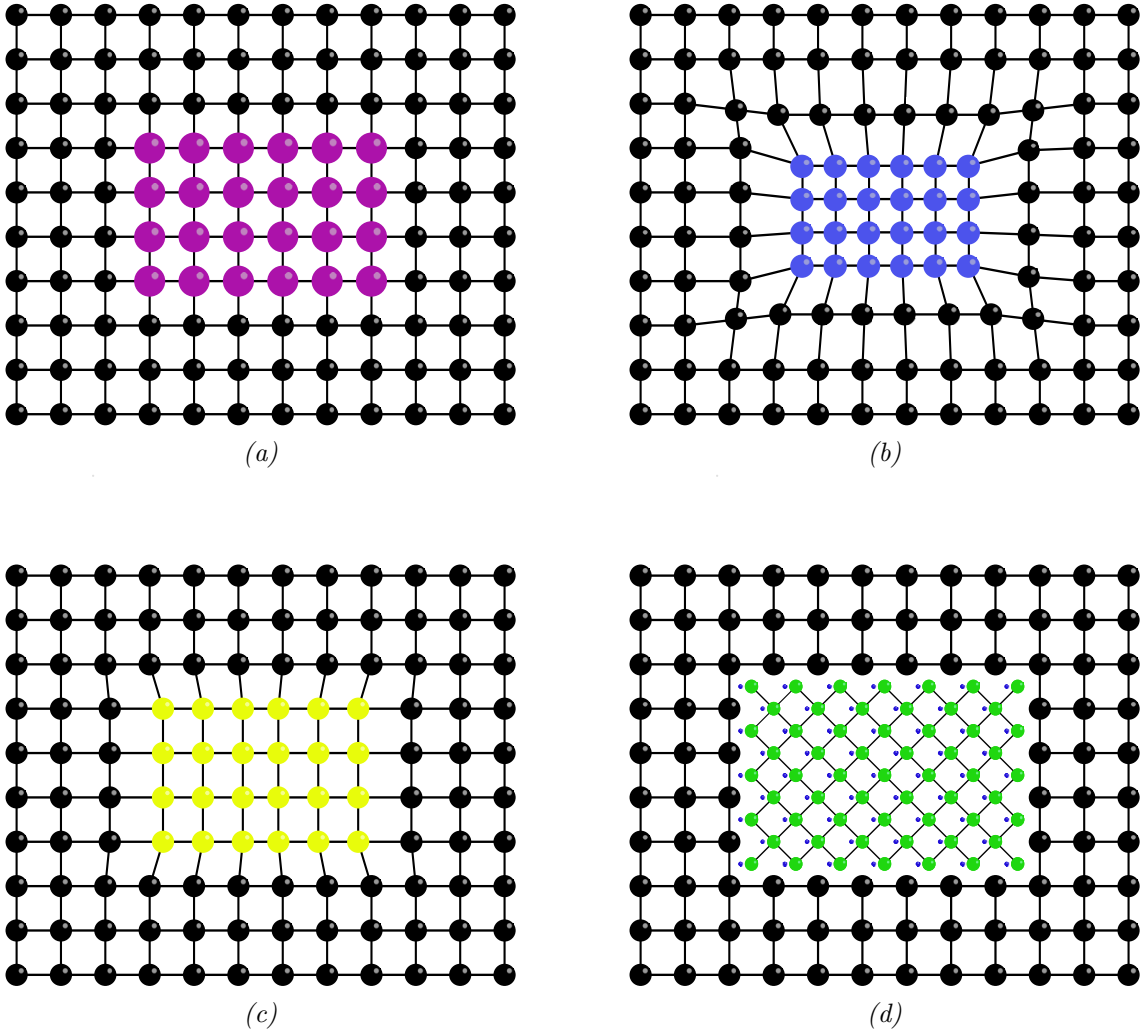

Figure 2.2: Figure (a) shows a fully coherent particle, figure (b) a coherent particle, figure (c) a partially coherent particle and figure (d) a non-coherent particle dispersed in the surrounding matrix.

2.2.4 Precipitation hardening

The strength of a metal may be increased through increasing its resistance against slip. In the case of aluminum, this is done through the process called *precipitation hardening* where a large amount of nano-sized precipitates are introduced into the metal which helps the metal withstand dislocation motion. The interference process between these precipitates and the dislocation motion may be described through three different mechanisms, coherency strain hardening, chemical hardening and dispersion hardening [12].

Coherency strain hardening is a hardening mechanism which results from the coherency strain fields created by precipitates in the matrix. The strain fields are created as the precipitates are not fully coherent with the matrix, but obtain coherency through bending and stretching of the surrounding matrix as can be seen in figure 2.2b. The hardness is obtained though the altering of crystallographic structure such that the Peierls-Nabaro stress (2.1) increases as the dislocation moves closer to the precipitate. This causes the precipitate to repulse the dislocation. The latter has consequences as the precipitates might also aid dislocation motion by repulsing them in the direction of their motion. The density of precipitates must therefore not be too high if maximum strength is to be obtained.

Chemical hardening is the hardening caused by the stress required to force a dislocation through the precipitate itself, called cutting. If the precipitate is coherent with the matrix, the dislocation may move by the same slip mechanism as in the matrix. However, as the dislocation moves though the precipitate, the precipitate will for the case of a line dislocation, increase in size due to the introduction of the extra half plane. The internal binding of the precipitate will also be altered, as the precipitate is inhomogeneous compared to the rest of the matrix. Both these events will together with additional effects result in a hardening because of the extra energy required to inflict them.

Dispersion hardening is the hardening obtained from larger incoherent precipitates called dispersoids. If the dispersoids are incoherent with the matrix, the dislocation may no longer pass though them through cutting as with coherent precipitates, but have to find alternative mechanisms to pass. The hardness is thus obtained by the strain required for the dislocation to pass the dispersoid by any of these alternative mechanisms.

2.2.4.1 Solute solution hardening

Hardening effects due to precipitation may not only be caused by nano-sized precipitates, but also by individual alloying elements being dissolved in the matrix. As the alloying elements are of different chemical character than the host element, they will cause local expansion or contraction of the lattice, resulting in coherency strain [13]. The coherency strain effect is visualized in figure 2.3, showing two different atoms dispersed in a host lattice.

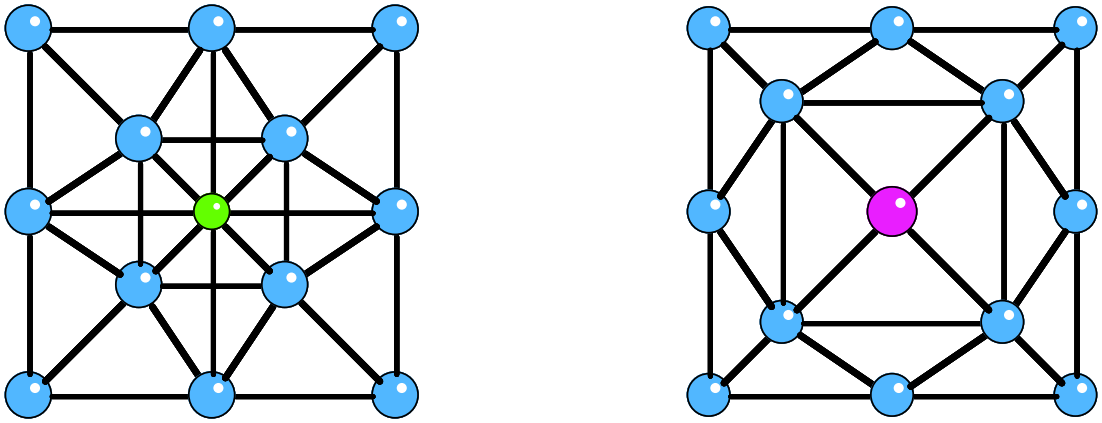

(a) *(b)*

Figure 2.3: Figure (a) shows a schematic drawing of an atom dispersed in the surrounding matrix which demand more space than the matrix atoms. Figure (b) shows a schematic drawing of an atom which requires less space than the surrounding matrix. Both can be seen to cause coherency strain [9].

2.3 Hardness measurements

The *hardness* of a material is not a very well defined term. It may refer to resistance against scratching, resistance against indentation (plastic deformation) or just the general strength of the material. There are various methods for measuring the hardness, i.e the Brinell, Rockwell and Vicker hardness tests that all use an indentor. In the present work we apply the Vicker hardness test for measuring hardness, and our definition of *hardness* will therefore be "the resistance of the material towards plastic deformation".

2.3.1 The Vicker hardness test

The Vicker Hardness test is performed with a pyramid shaped diamond being pressed into the material with a certain load and speed (load speed) during a given time (load time). The diamond then leaves a square-like mark on the material which size is defined by the length of its diagonals, d_1 and d_2. The mean of these diagonals measured in mm, $\bar{d}^2$ may together with the amount of load be combined in a relation to produce the so-called Vicker hardness number HVx, where x denotes the number of kilograms used as load. The relation for the Vicker hardness number reads as follows [14]

$$\mathrm{HVx} = \mathrm{x} \cdot \frac{2 \cdot \sin(\frac{136^\circ}{2})}{\bar{d}^2} \tag{2.2}$$

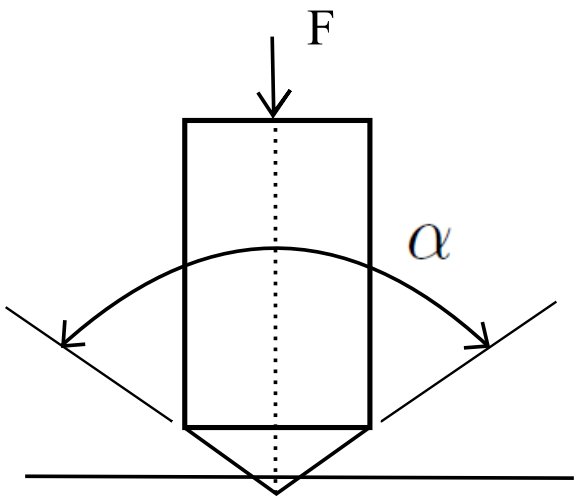

Figure 2.4: A schematic drawing of the intentor penetrating the surface of the sample. The angle between the faces of the diamond tip is denoted by α and is for the Vicker hardness test equal to 136°.

The length of the diagonals of the square indention is read manually using a microscope, and it is therefore very important how smooth the surface of the sample is. As seen in figure 2.5a[2], the indentor mark might be difficult to see, and the probability of getting inaccurate results is large. By performing a finer grind, and even polishing the sample, the indentor mark can be seen with sharply defined edges like the one shown on the schematic picture in figure 2.5b.

[2]The markings are seldom as good as these ones.

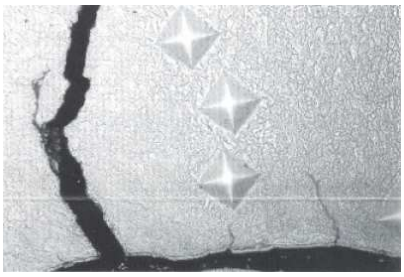

(a)

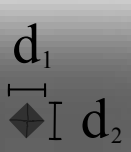

(b)

Figure 2.5: (a) A real image of the indentor mark, here made on brass [15]. (b) A schematic image of the indentor mark and what d_1 and d_2 refer to.

2.4 Heat Treatment of Metals

It is an important fact to keep in mind that the properties of aluminum alloys are not given entirely by the atomic composition of the alloys. This has already been mentioned by the fact that the two major types of aluminum alloys are defined by the way they are fabricated. The alloys may undergo different treatments to reshape their atomic structure to give them a desired set of properties. The different possible treatments can be summarized in 5 major groups denoted by the symbols F, O, H, W and T. The three first treatments meaning as-fabricated, annealed and cold-worked are not in the scope of this text and will not be discussed in any great detail. However they may appear in some context in later discussions. The last two, W and T, denote solution-treated and age-hardened and will be discussed in detail later. Solution treatment may in some cases be included as a part of the age-hardening, and a common term used in this case to include both is "heat-treating". A heat treatment is thereby a treatment where the alloy is kept at different temperatures for different amounts of time.

The hardness increase that age-hardenable alloys obtain during heat treatment was in the late nineteen hundreds discovered to be caused by nano size particles called precipitates.[3]. There are different precipitates with different morphologies, but they can commonly be interpreted as particles that jam the matrix in such a way that slip is less likely to occur. Slip is as described previously the movement of a dislocation, and a restriction against such movement will make the alloy hard. The

[3]This hardness increase is what defines an alloy to be age-hardenable

type of precipitate that is created is dependent on the temperatures used in the heat treatment and the corresponding storage times, and they can be represented in a temperature-wise succession called the precipitation sequence. In such a sequence, the precipitates formed at the lowest temperatures for shortest times are at the beginning and subsequently the precipitates formed at the highest temperatures are at the end.

2.4.1 Solute solubility

The first concept that needs to be explained to understand the reason for performing a heat treatment is *solute solubility*. When an alloying element is added to a metal there is limited amounts that can be added and dissolved before the solution splits into two separate phases. This is illustrated in the phase diagram of aluminum and silicon in figure 2.6 where the α-phase denote fully dissolved silicon in aluminum. As can be observed, the amount of silicon that may be dissolved in aluminum before pure silicon starts to form, is strongly dependent on temperature. By investigations of the phase diagram one observes that the maximum solubility of about 2 at% is found at 577°C.

It can be seen from figure 2.6 that the solubility of Si in Al varies with temperature. If 2 % of Si is completely dissolved in the host Al-matrix at 577°, a lowering of the temperature will result in a phase separation. Provided that the temperature is lowered quickly, a supersaturated solid solution would be the result. This is an unstable/metastable phase where the driving force for aggregation of Si atoms is very large.

The concept of super saturation can be explained by the analogy of a cup of tea where sugar is dissolved in the tea. It is known that one cannot dissolve infinite amounts of sugar in the tea before it forms solid sugar on the bottom of the tea cup. Also the solubility of the sugar depends on temperature of the tea such that if one dissolves as much sugar as possible in a hot tea and then cools is down, sugar crystals will form at the bottom of the tea cup. To dissolve the sugar, the tea has to be heated up again etc. If the cooling of the tea was done instantaneous, the sugar would not have had time to solidify during the cooling and would still be dissolved in the cold tea. In this short period of time the tea is what is called super saturated because more sugar is dissolved than is normally allowed. With time, however, the sugar will separate out from the solution.

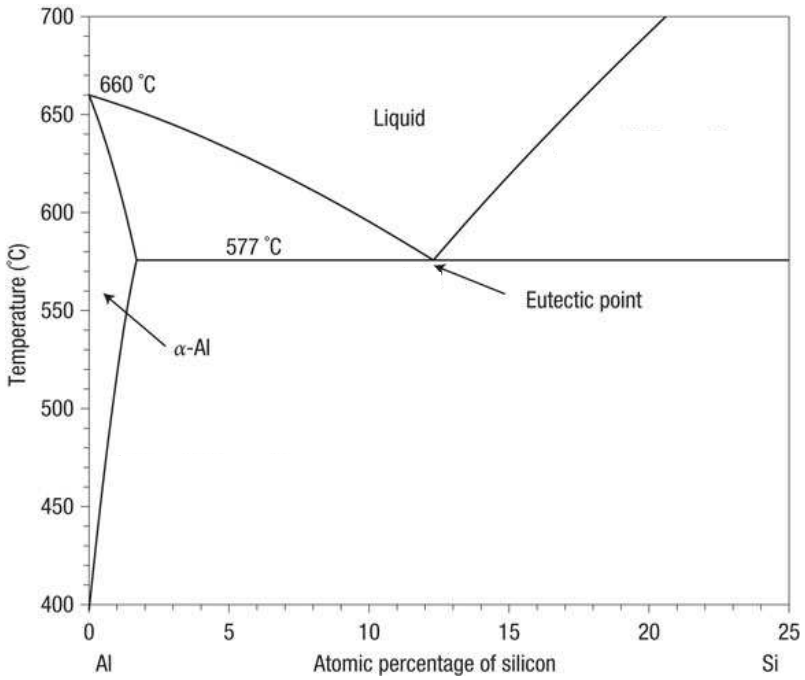

Figure 2.6: The phase diagram of silicon and aluminum. The α phase to the left is silicon fully dissolved in aluminum while the phase to the lower right is a combination of the α-phase and solid silicon. The horizontal line at 577°C is the solidus line. All phases above this line except for the α-phase consists partly or fully of a liquid state [16].

2.4.2 The usual heat treatment procedure for aluminum

An *Heat treatment* can be performed on aluminum alloys to alter their atomic structure for the purpose of producing desired properties. It consist of the alloy being kept at different temperatures at various times, and that the transition time from one temperature to another is as short as possible. The heat treatment is usually divided into three parts, namely solution heat treatment (SHT), room temperature storage[4] (RT-storage) and artificial aging (AA). A schematic diagram for explaining this procedure can be seen in figure 2.7. Different heat treatments are usually referred to by the abbreviation TX, where X is a number and T denotes that the alloy is subject to age hardening.

[4]Also referred to as natural aging (NA).

2.4.2.1 Solution heat treatment (SHT)

When an alloy is solution heat treated, it is heated to a high temperature ($\sim$500°C for aluminum) where it is kept for a time t_{SHT} which can vary from around 30 minutes to several hours. The temperature should be chosen such that the solubility of solute elements is the highest, but without any transition to the liquid form. Solution heat treatment has two purposes

1. To dissolve all phases consisting of solute elements in the aluminum matrix so that the solute elements are homogeneously spread out. This is a good starting point for constructing new phases.

2. To introduce vacancies in the Al matrix[5]. The density C_v of vacancies present in a metal increases exponentially with the temperature, and the vacancy concentration is explicitly given by [17]:

$$C_v = \text{constant} \cdot \exp\left[\frac{-E_f}{k_B T}\right] \tag{2.3}$$

   where E_f is the energy required to introduce one vacancy into the system, k_B is Boltzmann's constant and T is the absolute temperature in Kelvin. The diffusion of substitutional solute elements is dependent on vacancies, and vacancy diffusion is many orders of magnitude larger than the so-called self-diffusion of solute [18]. The process is therefore necessary to form clusters and cause growth of precipitates.

The next step is to quickly cool the alloy to room temperature, a process called quenching. The reason for this is that we wish to obtain a super saturated solid solution. The state of the system is then no longer stable, and it will undergo phase separation to lower its energy. After the quenching, the treatment enters the next phase which is called room temperature storage.

[5]A vacancy is a lattice position not filled by an atom

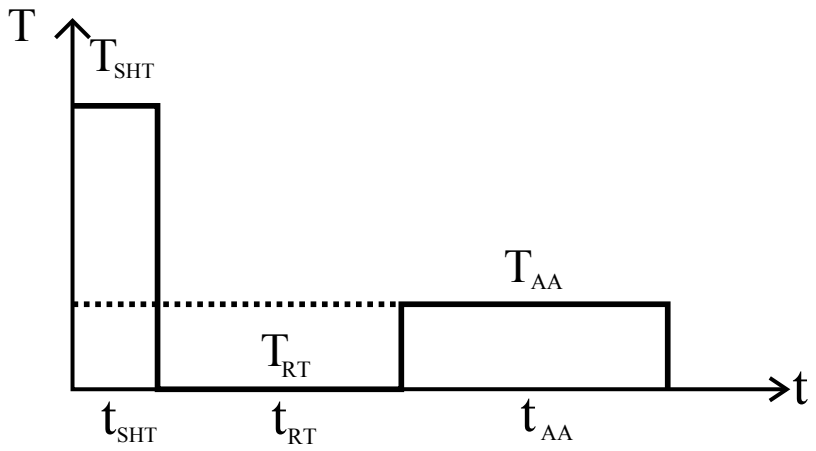

Figure 2.7: Schematic drawing of the heat treatment procedure. T_{RT}, T_{AA} and T_{SHT} denote room temperature (RT), temperature during artificial aging (AA) and temperature during solution heat treatment (SHT) respectively. The symbols t_{RT}, t_{AA} and t_{SHT} denote the times for the three steps. The vertical slopes in the temperature indicates an assumed instantaneous changes in temperature as the sample goes from one treatment to another.

2.4.2.2 Room temperature storage. (RT-storage)

During storage of the alloy at room temperature, the diffusion processes of solute elements often have enough energy to proceed. This may lead to favorable or unfavorable aggregations of solute atoms. The phases are constructed as the solute elements diffuse around in the matrix, and the time t_{RT} for which the process is allowed to proceed influences the process. In principle, the RT-storage step could go on until equilibrium is reached, but since diffusion at this temperature is such a slow process, it would take an infinitely long time [19].

2.4.2.3 Artificial aging (AA)

In this part of the treatment, the large precipitate particles are created during storage at elevated temperatures. The temperatures T_{AA} and time t_{AA} for this process are dependent of which precipitate phases are desired. For Al-alloys the AA treatment is typically performed at temperatures in the range 150-200°, but the exact temperatures and times are dependent on the alloy composition and solute content. When the desired precipitates are obtained, the alloy is again quenched and its then ready for use.

2.4.3 Early stage phase separation

When an aluminum alloy is being solution heat treated, all the solute elements are dissolved in the matrix. If the alloy is then quenched, the system gets a very high energy and is in an unstable/metastable super saturated state. To lower the total free energy of the system the solute elements cluster together by diffusion. The exact process governing the early-stage phase separation is dependent on whether the supersaturated solid solution is unstable or metastable, as will be outlined in this chapter. In the subsequent process of artificial aging the clusters might dissolve, or grow into precipitates.

2.4.3.1 Spinodal decomposition

Gibbs originally defined the stability of metastable binary phases by how well they could resist fluctuations in composition without going into a continuous transformation [20]. The metallurgical synonym for this is that the chemical potential for each component increases with increasing concentration of this component [21]. In other word, when a phase separation begins, the chemical potential continuously increases for both components in such a way that the separation is stopped. By metallurgical terms, the chemical potential is defined as the change of a system's molar free energy due to a small change in size, dn, of the system itself [18]. The change in the system's free energy can thus be written as

$$dG = \mu_A \mathrm{d}n_a \tag{2.4}$$

where G is Gibbs free enrgy, μ_A is the chemical potential for the component A and dn_A is the addition of a small quantity of A. The above relation is defined with constant pressure and temperature, which can be expressed in the above equation by solving it for μ_A.

$$\mu_A = \left(\frac{\partial G}{\partial n_A}\right)_{T,P} \tag{2.5}$$

The point of deriving this is are made clear by when equation (2.5) is differentiated with respect to the concentration of component A.

$$\frac{d}{dn_A}\left(\frac{dG}{dn_a}\right) = \frac{d}{dn_A}\mu_A \tag{2.6}$$

By combining this relation with Gibbs original definition of phase stability, a phase is defined to be unstable if it obeys the following relation.

$$\frac{d^2G}{dn_a^2} \leq 0 \tag{2.7}$$

This last equation is fulfilled within a spinodal and has resulted in the term spinodal decomposition used in metallurgy for barrier free separation of phases.

If an alloy now is quenched from a high temperature and into the area under this chemical spinodal, as for the alloy of composition X_0 in figure 2.8a, phase separation will occur by spinodal decomposition. In this process there is no barrier to the aggregation of solute, and the phases that form will not be allowed to dissolve as long as the degree of supersaturation is within the area under the chemical spinodal. As seen from figure 2.8b, the process of spinodal decomposition occurs when the curvature of the free energy is negative.

$$\frac{d^2G}{d^2X} < 0 \tag{2.8}$$

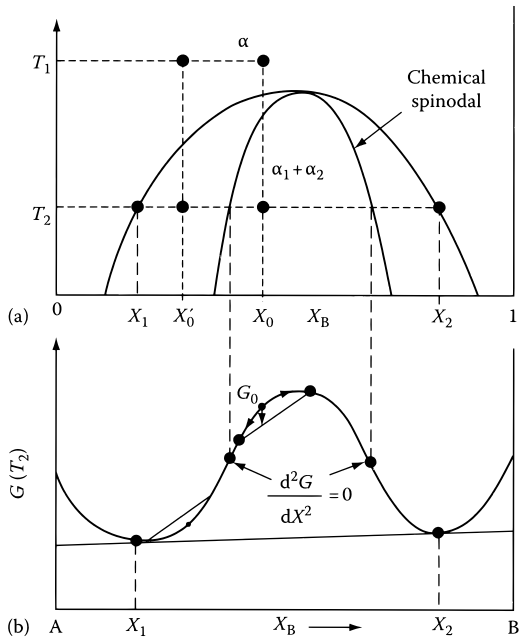

Figure 2.8: Figure (a) shows a temperature-composition diagram illustrating the quenching of a state represented by the upper right dot down from T_1 to T_2. The composition X_0' is quenched into the metastable region while the higher solute content in X_0 gives a quench into the unstable region. In both cases the phase is not stable as shown in the free energy graph in figure (b), and this leads to the formation of phases to lower the free energy of the system. Quenching into the inner parabolic area results in clustering by spinodal decomposition, while quenching into the intermediate region results in clustering due to nucleation and growth [18].

2.4.3.2 Homogeneous nucleation theory

If the composition lies outside the chemical spinodal, the transformation will occur by the process of nucleation and growth. This can be described by classical homogeneous nucleation theory. This states that clusters can be formed homogeneously when solute elements meet during diffusion, but the process can also expand already present aggregations of solute (such as clusters formed by spinodal decomposition). The latter process, which also describes the enhanced nucleation around lattice defects, is called heterogeneous nucleation.

A cluster of solute elements forming in the host matrix, will change the free energy of the system. If the metal is assumed to be homogeneous, the free energy can be described as:

$$G_2 = V_b G_v^b + V_s G_v^s + A_{bs}\gamma_{bs} \tag{2.9}$$

Here V_b is the volume of the bulk aluminum which has G_v^b as its free energy per volume, V_s is the volume of the cluster which has G_v^s as its free energy per volume and A_{bs} is the surface area of the cluster with a surface energy of γ_{bs} per unit area. By setting the free energy of the system equal to

$$G_1 = (V_s + V_b)G_v^b \tag{2.10}$$

the change in free energy ΔG due to the nucleation can be written as:

$$\begin{aligned} \Delta G = G_2 - G_1 &= V_s G_v^s + A_{bs}\gamma_{bs} - V_s G_v^b \\ &= V_s(G_v^s - G_v^b) + A_{bs}\gamma_{bs} \\ &= V_s \Delta G_v + A_{bs}\gamma_{bs} \end{aligned} \tag{2.11}$$

with $\Delta G_v = (G_v^s - G_v^b)$. By inspecting equation (2.11) it can be observed that for some critical radius r^* there is a balance between the surface energy and the energy per volume of the cluster. With the assumption of spherical clusters, equation (2.11) takes the form

$$\Delta G_r = \frac{4}{3}\pi r^3 \Delta G_v + 4\pi r^2 \gamma_{bs} \tag{2.12}$$

Minimizing equation (2.12)by setting dG=0 results in a critical cluster radius r^* of:

$$r^* = \frac{2\gamma_{bs}}{\Delta G_v} \implies \Delta G^* = \frac{16\pi\gamma_{bs}}{3\Delta G_v^2}. \tag{2.13}$$

Here ΔG^* is then the energy that is required to create a cluster with radius above the critical radius. Only when the radius of the cluster extends this size the cluster will continue to grow. Every cluster with $r < r^*$ is not stable and will tend to dissolve. The variables related to the process is depicted in figure 2.9. The stochastic

formation and dissolution of small clusters is characteristic for the process of homogeneous nucleation. It is only when enough energy is provided for the system to surpass the nucleation barrier $\Delta G*$ and form a cluster of radius larger then r^* that continuous growth of the cluster takes place.

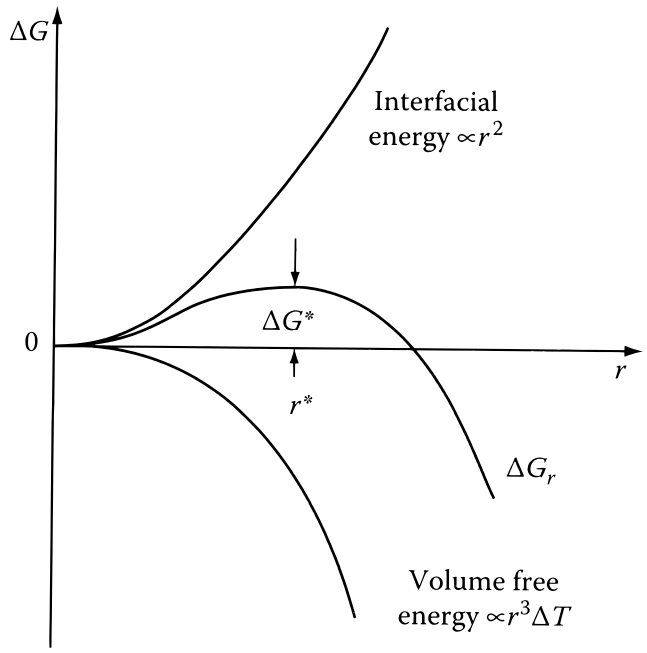

Figure 2.9: The Gibbs free energy associated with the nucleation of a spherical cluster. Because of that the surface and volume terms depends differently on the raduis r, a critical radius r^* can be found with a corresponding ΔG^* [18].

2.5 The Al-Mg-Si (6xxx) alloy system

Al-Mg-Si alloys or 6xxx alloys as they are labeled, are of the most commercially used Al-alloys today. Due to their good corrosion and welding properties, high strength to weight ratio and low cost, they can be used in everything from the transport industry to the consumer industry. In particular they are used as car body sheets, and this is mainly due to the way their strength is obtained. Such car body sheets are namely paint-baked at 180°C before they are being used, a temperature which is about the same as that which results in the peak hardness of these particular alloys [19]. This makes the age-hardenable 6xxx series Al-Mg-Si alloys optimal for such applications.

2.5.1 Precipitation sequence

As discussed in section 2.4 the hardness obtained for age-hardenable alloys during heat treatment is caused by the strain-field surroundings of nano-sized particles called precipitates. The precipitation sequence for the type 6xxx alloys studied in this thesis, has been reported as:

$$\text{SSSS} \rightarrow \text{AC} \rightarrow \text{GP zones[22][23]} \rightarrow \beta''[24] \rightarrow \beta'[25], \text{U}_1[26][27], \text{U}_2[26][28], \text{B}'[29] \rightarrow \beta/\text{Si} \tag{2.14}$$

with SSSS standing for super saturated solid solution, AC for atomic clusters and GP zones standing for Guinier-Preston zones (also called pre-β''). The rest of the symbols just denote the respective precipitate phases, with the uttermost right phase β (Mg_2Si) being the equilibrium phase. Phases listed to the right in the sequence are larger phases and they are created at higher temperatures and longer times than the ones to the left.

2.5.1.1 Atomic clusters

The formation of every kind of precipitate from a homogeneously distribution of solute has to begin with two solute atoms clustering together. This argument together with observation of structured precipitates proved the existence of clustering even before they could be studied by sophisticated techniques like atom probe tomography (APT). The definition of solute clusters in the precipitation sequence 2.14 ranges between two solute atoms being next to each other up to the point where the cluster begins to grow large. The clusters are coherent with the Al matrix and can hence not be observed in TEM because of the lack of contrast [30].

2.5.1.2 GP-zones

When a cluster continues to grow from a random distribution of solute, it will eventually grow into, what is a bit loosely defined as a GP-zone. GP-zones may exist several differently evolved phases, with one of the more evolved being the pre-β" precipitate [19]. Since GP-zones are much larger than clusters, coherency effects makes them possible to investigate with HRTEM. This has been done eg. by Marioara et. al [22] who discovered that needle-like GP-zones in the 6082 Al alloy were less coherent with the matrix than β". Three dimensional atom probe (3DAP) studies by Murayama and Hono [30] have shown that GP-zones in the same alloy system have a Mg to Si ratio close to 1. The term GP zone is however mentioned very generally in literature and usually defines a small particle with little but non-zero coherency with the matrix.

2.5.1.3 The β" precipitate

The β" precipitate, also called the GP-II zone, is the main hardening phase in 6xxx-alloys [31]. It has a needle shape morphology and is elongated along the $\langle 100 \rangle$-direction of the aluminum lattice with size $\sim$4x4x50 nm [24]. It is fully coherent with the Al-matrix along the b-axis and semi-coherent along the two others. The phase is created when the alloy is being stored at a temperature between 125° and 220° [19] (artificial aging). If aged at 250° and above the β"-phase will quickly start to dissolve/transform [32].

The crystal structure of the β" precipitate is monoclinic with $a = 1.516$ nm, $b = 0.405$ nm, $c = 0.674$ and $\beta = 105.3°$ (figure 2.10). The precipitate is ordered relative to the host aluminum lattice in such a way that $(001)_{Al}||(010)_{\beta''}$, $[\bar{3}10]_{Al}||[001]_{\beta''}$

and $[230]_{Al}||[100]_{\beta''}$. In other words the angle between the β'' a-vector and $[010]_{Al}$ is 33.69° and the angle between the β'' c-vector and $[100]_{Al}$ is 18.43° [24].

The composition of the β" phase was long believed to be Mg_2Si after the composition of the equilibrium phase β. However, in 1996, it was showed by Edwards et. al. [33] though APT investigations that the Mg/Si ratio was closer to one, and in 1997 Andersen et. al. [24] found the composition to be Mg_5Si_6. The latter result was adjusted through APT and DFT studies by Hasting et. al. [34] who found the composition more likely to include some aluminum, and concluded upon $Mg_5Al_2Si_4$ as all precipitates were Mg-rich, and not Si-rich, as suggested by Andersen et. al.

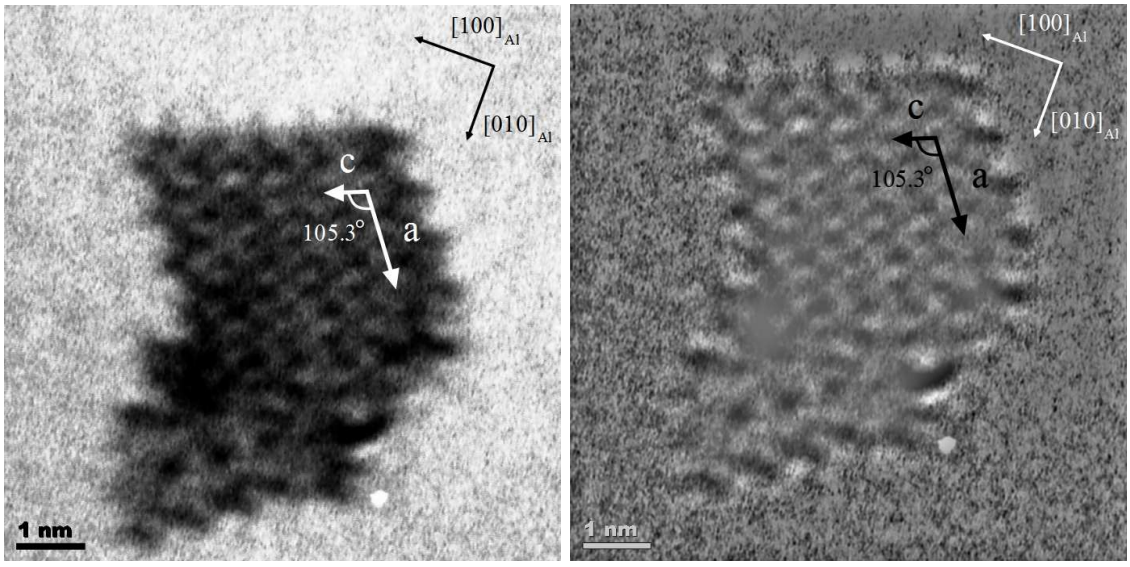

(a) *(b)*

Figure 2.10: Pictures of the β" precipitate taken with conventional TEM. (a) shows the original picture, while (b) shows a filtered version. The precipitate eyes [24] can be seen as small rings, and denote the unit cell centers. Picture taken by the author.

2.5.1.4 The β' precipitate

Upon further aging, or higher aging temperatures, the β" phases will start to dissolve/transform and one of the phases replacing it is β' [32]. The β' precipitate is a lot bigger than its predecessor with dimensions ∼10x10x500 nm (compared to ∼4x4x50 nm for β"). It has a hexagonal unit cell with $a = 0.705$ nm and $c = 0.405$ nm, with the latter coinciding with the 4.05 Å lattice parameter of fcc aluminum causing a fully coherency with the $\langle 001 \rangle_{Al}$. The hexagonal unit cell of the β' precipitate can be recognized figure 2.11. In contrast to β'', the unit cell of β' doesn't have

a required orientation in the aluminum (001)-plane and may therefore be observed with many different orientations [25].

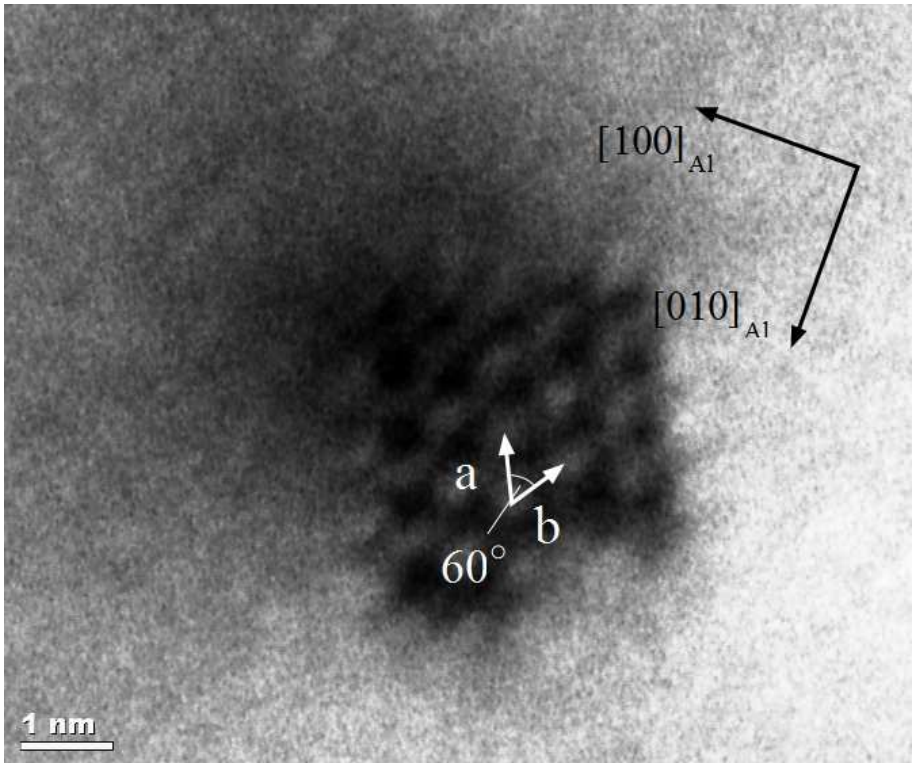

Figure 2.11: Picture of the β' precipitate taken with conventional TEM. The unit cell can be observed to be hexagonal with lattice parameters $a = b = 7.05$ Å. Picture taken by the author.

2.5.1.5 The B', U1 and U2 precipitates

The B', U1 and U2 precipitates or A, B and C as they are also known as [35] are as β' successors of β" [32]. They coexist with β', which explains the notation in the precipitation sequence (2.14). B is a hexagonal rod-shaped, semi-coherent phase which is often found on dislocations, U1 are Si-rich and belongs to the ionic Zintl-type structures with space group $P_{\bar{3}m1}$ while U2 is orthorhombic with space group P_{nma} [28]. More information about their crystal structure are listed in table 2.2 and a conventional TEM-picture of the B'-phase is shown in figure 2.12.

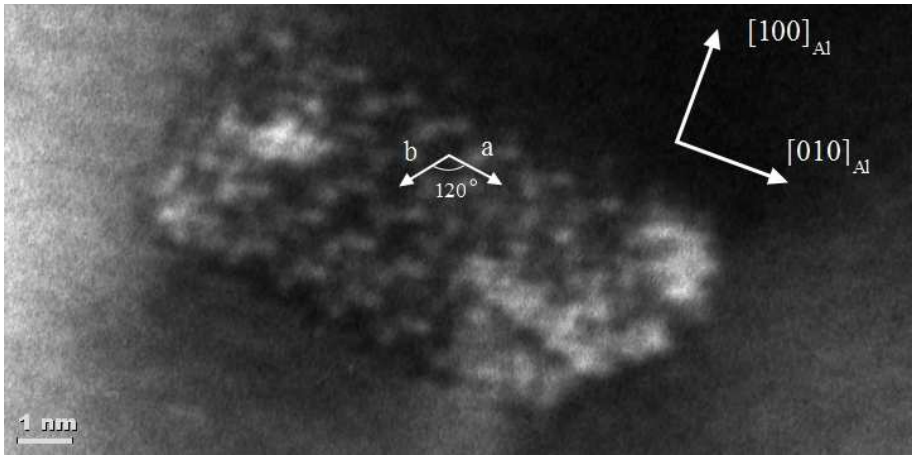

Figure 2.12: Picture of the B' precipitate taken with conventional TEM. The precipitate eyes can be seen as hexagonal rings, and denote the unit cell centers. The unit cell can be observed to be hexagonal with lattice parameters $a = b = 10.4$ Å. Picture taken by the author.

Table 2.2: Overview of the the precipitate phases U1,U2 and B' (A, B and C) [32]

Phase	Shape	Lattice parameters (nm)
U1 (A)	Needle	a=b=4.05, c=0.674, γ=120°
U2 (B)	Needle	a=0.675, b=0.405, c=0.794
B' (C)	Lath	a=b=1.04, c=0.405, γ=120°

2.5.1.6 The equilibrium phase β

If a 6xxx-alloy are heat treated at high temperature for long times, all solute locked up in precipitate phases will eventually end up in the equilibrium phase β. The β phase has the known crystallographic structure CaF_2 of the type f.c.c. with a=0.639 and composition Mg_2Si [36]. Because of this composition, it was long thought that all the hardening phases had the same composition until otherwise enfeebled by Andersen et. al. in the late 90's [24]. Compared to the other precipitate phases in 6xxx alloys, the β phase is very large with dimensions $\sim \mu$m.

2.5.2 Industrial alloys

In addition to the solute elements Si and Mg, some alloys also contain a small amount of Mn and Fe, making them so-called industrial alloys. The Mn and Fe atoms are present to form so-called dispersoids together with some ($\sim 0.12\%$) of the silicon [2]. These dispersoids are larger that the precipitates formed during heat treatment, and are wanted due to their ability to pin the grain boundaries in the alloy. Without going into details one can interpret grains as small parts of the alloy where the orientation of the matrix is different. The sizes of the grains decide several properties of the alloy, but for a given alloy condition they are of constant size and of no further interest for the study presented here.

2.5.3 Natural aging

As shown in the precipitation sequence for the 6xxx alloy system (2.14), many studies have been performed on the precipitates and how they affect the properties of the alloys. However, the formation and effect of atomic clusters in the first term in the sequence is not very well understood and has been subject to only a handful of studies.

The importance of the clustering process is that it can take place even during room temperature, which is inevitable when producing Al-alloys on an industrial scale. The engineerical difficulties of moving many tons of aluminum from one heat treatment to another makes the typical natural aging times used by industry approximately four hours. Knowledge and control over the solute clustering going on during this time could potentially result in great profit for the industry.

Natural aging at RT causes clustering of solute elements. Due to the small size and coherency of these clusters they are not observable in TEM and hence other methods have to be used [30]. The effect on macroscopic quantities however, such as hardness and tensile strength is straight forward to investigate. It is for example shown in studies by Banhart et. al [6] that the clusters formed during natural aging cause a hardness increase, hence proving that the clusters are straining the Al-matrix. Røyset et. al. showed in 1996 how this affects the strength of different alloys after AA, where the final strength of alloys with Mg+Si<1wt% were observed to show a positive effect of NA before AA, and alloys with Mg+Si>1wt% a negative effect [37]. The the results of Røyset et. al. have been showed to be directly caused by clustering during NA as this affect the precipitation during AA. It has been showed that alloys of high solute content (Mg+Si>1wt%) experience a decrease in precipitates when subject to intermediate NA before AA [38], while alloys of lower

solute content, get their precipitation boosted [39]. However, knowing the effect of the clustering does not give any information about how the clusters are formed, why they form, how they are composed etc. To study these things, studies of their micro-structure have to be performed.

In order to study the micro structure of these clusters, highly sophisticated experimental methods are required, and hence they have not been the subject to any direct studies before recently. Examples of recent studies are atom probe tomography studies by Torsæter et. al. [8] and De Geuser et all [40], and positron annihilation spectroscopy studies by Banhart et. al. [7].

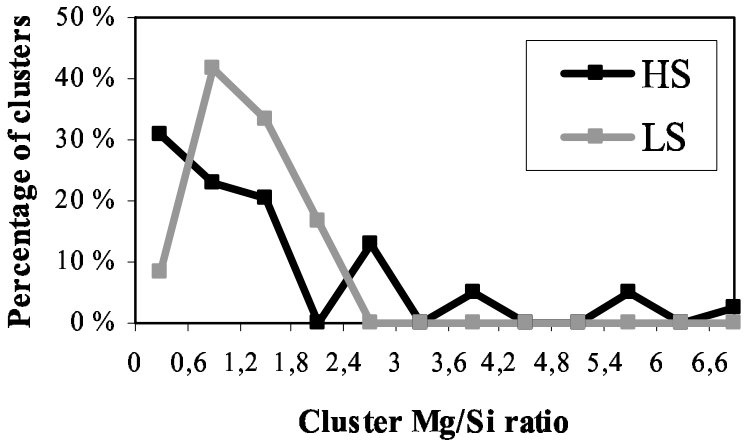

Figure 2.13: The figure shows the histogram distributions of the Mg/Si ratios in the observed clusters for both the HS and the LS alloys after 2 months of natural aging. The LS alloy has a peak around Mg/Si∼1 while the distribution for the HS alloy extends over a wide range of Mg/Si-ratios. [8]

In the study by Torsæter et. al, two alloys termed HS (High solute) and LS (Low solute) were studied. Both displayed the characteristic hardness change upon natural aging [6]. These two alloys are two of the exact same alloys that are to be studied in this thesis and the results found by Torsæter et. al are thus of great relevance. The number density of clusters can be seen in figure 2.14 and is numerically given as 3.42 $10^6/\mu m^3$ and 0.43 $10^6/\mu m^3$ for the HS and LS alloy respectively. This results in an approximately 8 times higher density of clusters in the HS alloy compared to in the LS alloy. The compositions of the clusters are illustrated in figure 2.13, which shows that the clusters formed in the LS alloy have a compositions peaked around Mg/Si∼1 while for the HS alloy the various cluster

[6]The hardness of the HS alloy decreased if NA was performed before the AA, while the hardness of the LS alloy increased.

Mg/Si-ratios are of a much wider extent. The percentages of solute elements trapped in clusters were also studied and it were found to be 12.2% for the HS-alloy and 2.07% for the LS-alloy.

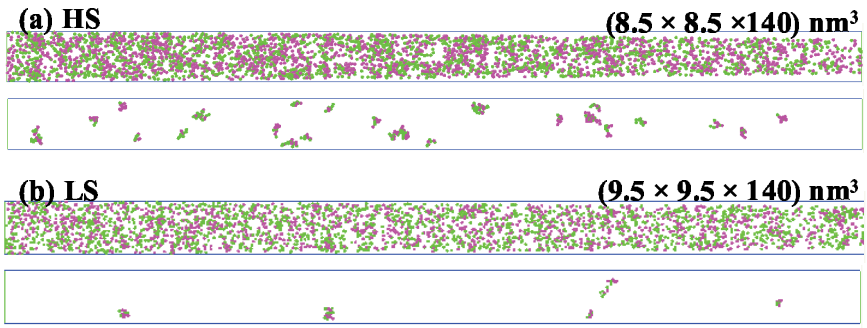

Figure 2.14: The figure shows two atom probe tomography (APT) volumes which illustrate the number of clusters within comparable parts of the HS and LS alloy both before and after the application of the maximum separation method. Note that the images only show the solute elements Mg and Si [8].

Although some studies have been performed on the micro-structure of these alloys during NA, there is no universally accepted theory that explains the phenomena causing the negative and positive effects. The phenomenon resulting in a positive effect on precipitation hardening is usually explained by the clusters acting as nucleation sites for precipitates and thereby resulting in an increased alloy hardness [38][41][42]. The phenomenon behind the negative effect on the high solute alloys is on the other hand, often explained by stating that some of the clusters of a type not formed in the low solute alloys are unable to act as nucleation sites for further precipitates. They then only lock up solute elements, and prevent them to take place in the precipitation reaction during aging [38]. Another explanation for the negative effect is that the clustering produce such a high number of competing clusters that the solute redistribution is hindered.

2.6 Transmission electron microscopy

Transmission electron microscopy (TEM) is a technique which was developed in the early nineteen hundreds to study details too small to be seen by traditional optical microscopes. TEM has during the years developed to be one of the leading techniques in the nano-age with the most sophisticated microscopes today being able to distinguish points closer than 1 Å to each other [43].

2.6.1 The Rayleigh criteria

The rule of thumb when measuring a length is that you can not measure something that is smaller than your measurement tool. This statement refers to the famous Rayleigh criterion for optical microscopes which states that the smallest distance that can be resolved, δ, is given by the relation [43];

$$\delta = \frac{0.61\lambda}{\mu \sin\beta} \tag{2.15}$$

where λ is the wavelength of the radiation, and μ and β are variables defining the viewing medium and depiction device. Using various βs it can from the Rayleigh criteria be understood why the naked eye has a resolution limit of at best 0.1 mm while the best optical microscopes may obtain a resolution down to 200 μm using the lowest visible light wavelength of violet which is about 400 μm. To further increase the resolution, one has to surpass the limitation from the visible light wavelength by the use of other sources of radiation.

After electrons were discovered to posses wave-like as well as particle-like behavior, it took less than 10 years before the first electron microscope was created. The advantage with electrons relative to photons, is their far shorter wave-length λ, shown by de Broglie in 1924 to follow the relation;

$$\lambda = \frac{h}{p} \tag{2.16}$$

where h is Planck's constant and p is the momentum of the electrons. An important point here is that the wavelength of the electrons can be controlled by controlling the momentum of the incident electrons. Introducing the relativistic expression $E = \sqrt{m_0^2c^4 + p^2c^2}$, for a particle with rest mass m_0, the wavelength of the electrons

can be given explicitly in terms of their kinetic energy $T = E - mc^2$.

$$\lambda = \frac{h}{\sqrt{2m_0T(1 + \frac{T}{2m_0c^2})}} \tag{2.17}$$

The wavelength can then be made very short by just accelerating the electrons by easily obtainable methods. For example an electron with energy of 100 keV has a wavelength of only 0.00365 nm, a distance far shorter than any interatomic spacing. Although this theoretical limit is not possible to reach due to e.g. problems with lenses, electrons are at present used in TEMs for resolving points closer than 1 Å from each other [43].

2.6.2 The instrument

A transmission electron microscope (TEM), can be easily understood by comparing it with a conventional transmission light microscope (TLM). In a TLM the light shines though the specimen giving information according to the light's transparency at different points in the specimen. The TEM works more or less the exact same way except that it uses electrons rather than visible light to generate a two-dimensional projection image of the three-dimensional specimen. With the far shorter wavelength of the electrons relative to light comes an additional property of electron microscopes as they are able to generate diffraction images of selected areas (SAD) of the specimen. This additional property makes electron microscopes very useful as they can simultaneously be used for both imaging and crystallographic investigations.

The transmission electron microscope consists of a main column including an electron source, a condenser system, a specimen stage, an objective lens, an imaging system and a viewing screen. In addition comes a series of apertures that can be used by the operator to control different aspects of the imaging and diffraction. An overview of the TEM column can be seen in figure 2.15 where the left column shows the TEM in imaging mode and the right column shows the TEM in diffraction mode with the selected area aperture inserted. Since electrons interact strongly with matter, the column is kept at high vacuum to avoid any unwanted electron interactions. Therefore a series of pumps like mechanical pumps, diffusion pumps, turbo pumps, ion pumps etc. are installed to keep the vacuum at a satisfactory level.

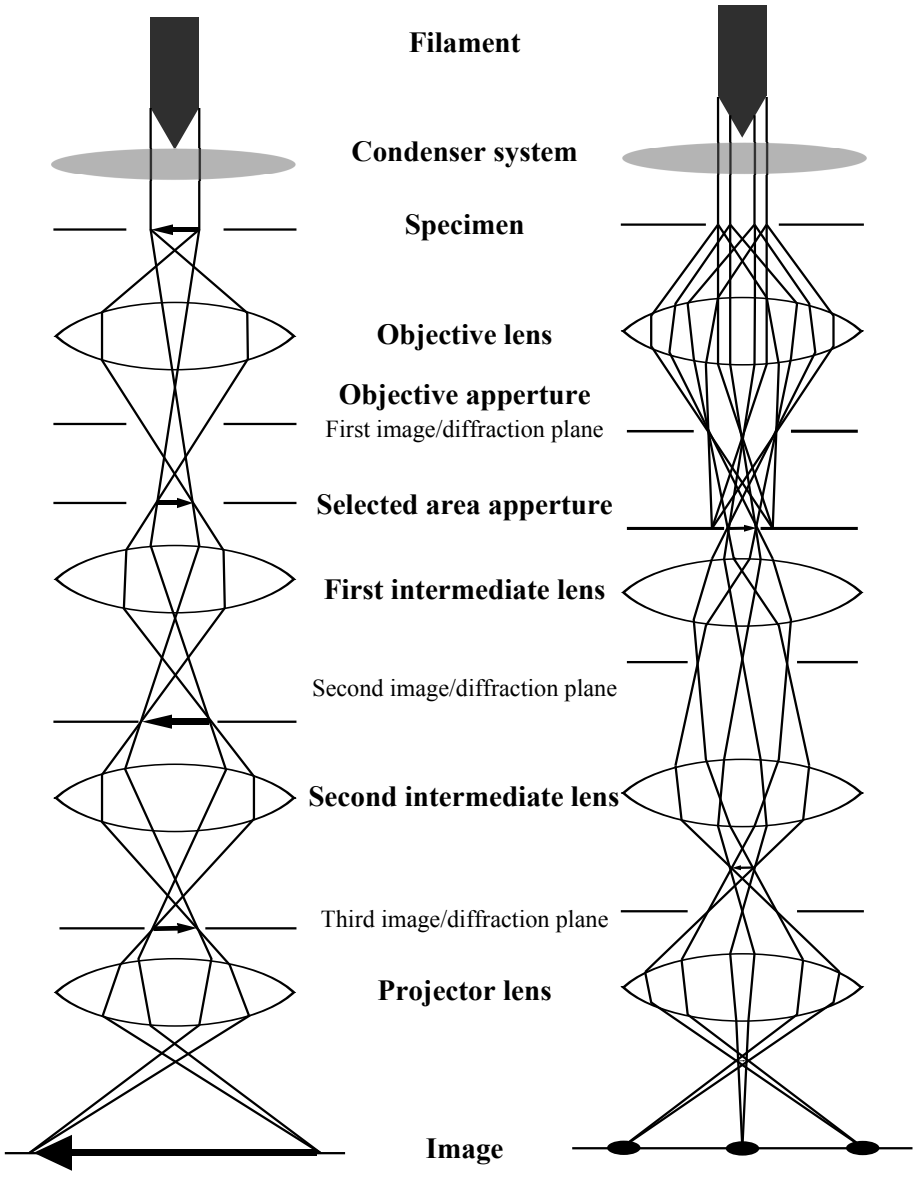

Figure 2.15: A schematic drawing of the TEM column as the TEM operates in normal imaging mode (left) and diffraction mode (right). The TEM consists of an electron source, several apertures and lenses which together creates an image in the bottom image plane. The different apertures may be used to isolate specific parts of the beam, making it possible for the operator to extract several types of information. An example are shown in the right picture where the selected area aperture are used to isolate the signal from a selected area of the specimen only, creating a so-called selected area diffraction (SAD) pattern.

2.6.2.1 Electron sources

The possible electron sources used in TEMs can be divided into two groups: thermionic sources and field emission sources. The thermionic sources work in a simple way, as they are heated to a high enough temperature that they emit electrons. A problem, however, is that the temperatures required to obtain electron emission are too high for most materials. Because of this, the thermionic sources used in TEMs are mostly tungsten (W) or lanthanum hexaboride (LaB_6) with their very high melting points. Thermionic sources don't require a very high vacuum and are quite cheap compared to other sources. However they produce a quite incoherent radiation, with LaB_6 being the most coherent having an energy spread of 1.5 eV [43].

Field emission sources of field emission guns (FEGs) work as the electrons tunnel out of a sharp tip under the influence of a strong electric field. The tip is commonly made out of tungsten and may be operated in hot or cold conditions. It is very needle like with a width of about 1 μm causing the effective emission radius to approach $\sim$0.01 μm [43]. This results in a very coherent beam with energy as low as 0.3 eV for cold FEGs [43]. Apart from all the advantages with FEGs, two downsides are the prize and the high vacuum requirement. For field emission to occur, it is required from the tungsten tip that it's free from oxides and other contamination. Because of this, the vacuum required may be as high as 10^{-9} Pa for cold FEGs, which is an incredible high vacuum [44].

2.6.2.2 Lenses

The lenses in an electron microscope (EM) are compared to optical microscopes not made out of glass, but are simply electromagnetic fields. These fields are generated by live coils where focus are adjusted by simply controlling the current in the coil. The lenses in a TEM are both used to control the incident angle on the specimen as well as generating the final picture.

Unfortunately, the creation of electromagnetic lenses is very hard, causing them to be the biggest restriction on resolution in a TEM [43]. The problem is the decreasing quality of the lenses as the distance from the optical axis increases (called spherical aberrations). Because of this, apertures are inserted to restrict the beam to an area close to the optical axis in such a way that spherical aberrations are kept at a minimum.

2.7 Scattering and contrast

When the incident electron beam hits the TEM specimen, some of the electrons will interact with the specimen through what is defined as scattering. Electron scattering is mainly divided into (i) elastic and (ii) inelastic scattering, where (i) is defined by no energy loss and (ii) by an energy loss for the incident electrons. The energy released when the electrons scatter inelastically generates, in addition to the electron signal itself, a series of different signals including *characteristic x-rays*, *secondary electrons* and many more. These signals are very useful because they provide information about the sample including composition, crystallographic orientation and topography. A collection of the different signals generated in the TEM is shown in figure 2.16

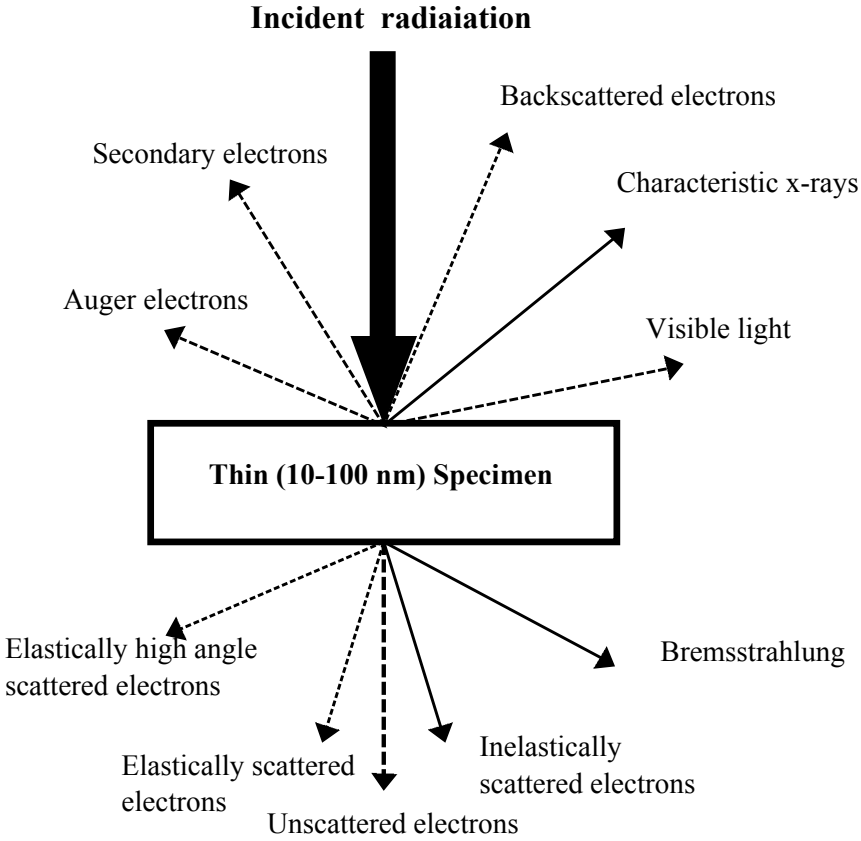

Figure 2.16: A schematic illustration of the different signals generated in a TEM because of electron interaction with the specimen. The electron beam can be seen to generate many signals where the forward scattered electrons are the ones used in conventional TEM.

Although many signals are generated inside the TEM, the main concern in this thesis is the primary forward elastically and inelastically scattered electrons. These two kinds of electrons are not only characterized by their energy interaction with the specimen, but also by their scattering angle and coherency. Elastically scattered electrons scattered less than 10 degs. are mostly coherent while an increasing scattering angle would decrease the degree of coherency. Inelastically scattered electrons are on the other hand, usually scattered less than 1 deg. and are almost always incoherent [43].

2.7.1 Contrast in TEM

The main source of contrast in a TEM image is the elastically scattered electrons [43]. Without going into too much detail, the contrast in a TEM may be dived into three, (i) mass-thickness contrast, (ii) diffraction contrast and (iii) phase contrast [44].

Mass-thickness contrast is, as the name suggests, caused by variations in mass and sample thickness. The atomic form factor or scattering factor f for electron scattering increases with increasing atomic number, and a contrast would hence be observable between objects of high mass and objects of low mass. Contrast due to thickness variations can easily be understood since a scattering event is more likely to happen in a thick specimen than in a thin specimen [44].

Diffraction contrast is the contrast associated with the diffraction amplitude from a set of planes hkl that fulfills the Bragg condition. Strain caused by for example lattice defects will alter the lattice parameter of the crystal and the Bragg condition will no longer be fulfilled at this spot. This will lead to a difference in amplitude at this spot, and will be observed as contrast in the image [44].

Phase contrast occurs due to scattering of electrons away from the optical axis. These scattered electrons now pass through the lens system similar til the directly transmitted electrons, but at a distance away from the optical axis. When the final image is created at the image plane, these off-axis electrons have traveled a longer distance than the on-axis electrons causing a phase shift. This phase shift may result in an interference pattern in the image plane causing the so-called phase contrast. Phase contrast is important in high resolution TEM (HRTEM), but gives little contribution at low magnification [44].

2.7.2 Diffraction in TEM

Diffraction in TEM happens as the wavelength of the electrons are smaller than the lattice parameters of the investigated sample. It is a very useful tool in TEM as it may be used to obtain a wide range of crystallographic information about the sample. Although this is not a text in crystallography, some simple diffraction theory will be discussed in order to understand the diffraction patterns obtained in TEM as well as Kikutchi diffraction.

2.7.2.1 Braggs law

For constructive interference to occur from scattering in a crystal, Bragg's diffraction law has to be fulfilled [45].

$$2d\sin\theta = n\lambda \tag{2.18}$$

Here d is the interplanar spacing, θ is half the scattering angle, n is an integer and λ is the wavelength of the radiation. This is shown in figure 2.17 where the path difference between the two rays has to be an integer number of wavelengths of the incident radiation in order to obtain interference.

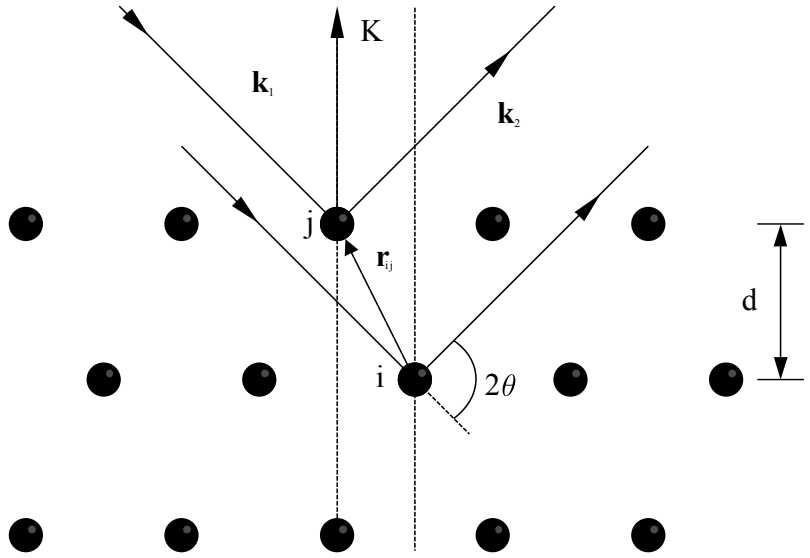

Figure 2.17: A schematic illustration of the diffraction from two scattering centers i and j with $\mathbf{k}_1$ *and* $\mathbf{k_2}$ *as the incident wave vector and diffracted wave vector respectively. The two exiting rays create constructive interference if the planar spacing d and scattering angle* 2θ *are according to Braggs law (equation 2.18).*

2.7.2.2 The Laue criteria

An alternative way to derive the Bragg diffraction law is through the so-called Laue condition. The derivation is based on the simple assumption that each set of atoms on the Bravais lattice radiates the incident radiation in all directions at the same frequency. The incident radiation are described by the plane wave $\exp[i\mathbf{k}_1 \cdot \mathbf{r}]$ and the radiated wave by $\exp[i\mathbf{k}_2 \cdot \mathbf{r}]$ with the scattering vector $\mathbf{K}$ given as $\mathbf{K} = \mathbf{k}_2 - \mathbf{k}_1$. Considering the scattering visualized in figure 2.17, the path different between the incident and scattered wave can through geometrical calculations be shown to be $(\mathbf{k}_2 - \mathbf{k}_1) \cdot \mathbf{r}_{ij}$. This results in a phase difference between the wave scattered from i relative to the wave scattered from j equal to $\exp[i\mathbf{K} \cdot \mathbf{r}_{ij}]$. For constructive interference to occur it is known from earlier that the phase difference between the two waves has to be zero. This inflicts the requirement that $\exp[i\mathbf{K} \cdot \mathbf{r}_{ij}] = 1$ which can be rewritten by exchanging $\mathbf{r}_{ij}$ with the Bravais lattice vector $\mathbf{R}$ to obtain a requirement for constructive interference on the form:

$$\exp[i\mathbf{K} \cdot \mathbf{R}] = 1 \tag{2.19}$$

With equation (2.19) only being valid when the scattering vector $\mathbf{K}$ is equal to the reciprocal lattice vector $\mathbf{G}$, we have obtained the Laue condition for diffraction.

$$\mathbf{K} = \mathbf{G} \tag{2.20}$$

2.7.2.3 The Ewald construction

The reason for deriving the Laue condition lies in its geometrical representation, the so-called Ewald construction. This construction can be visualized by drawing the incident wavevector $\mathbf{k}_1$ together with the respective reciprocal lattice of the investigated crystal in such a way that it terminates at one of the reciprocal lattice points. The so-called Ewald sphere is then drawn around the origin of $\mathbf{k}_1$ with a radius equal to $|\mathbf{k}_1| = 2\pi/\lambda$. If this sphere interferes with any other reciprocal lattice point, then the Laue condition is fulfilled and constructive interference is obtained [46].

An important part to remember is the $1/\lambda$-dependence of the radius of the Ewald sphere. Given a fairly large wavelength, the Ewald sphere will be rather small and a maximum of a few reflections will be observed in the diffraction pattern (DP). However, if the wavelength on the incident radiation is very small, the Ewald sphere will be extremely large such that the sphere may intersect with several reciprocal lattice points at once for certain orientations of the crystal. This is the case in a TEM because of the very small wavelengths of the electrons, and this is what is

causing the DPs in TEMs to include many diffraction spots at once. An schematic drawing of this can be seen in figure 2.18b where the Ewald sphere is very large compared to the lattice. Many spots are then approximately on the sphere resulting in a multi dot DP.

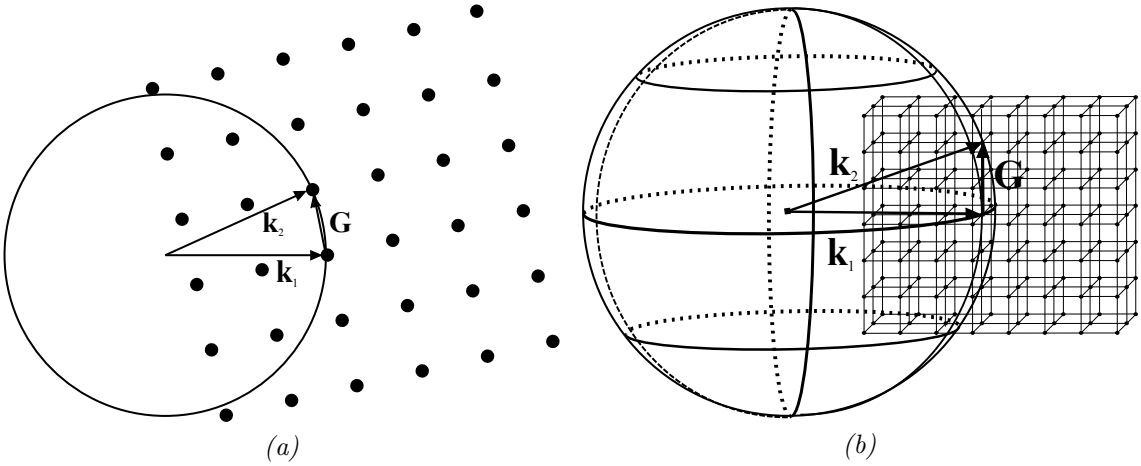

Figure 2.18: The Ewald construction for the Laue condition drawn in 2D (a) and 3D (b). The spheres are drawn as the incident wavevector is made to terminate at a reciprocal lattice point, using its starting point as origin and its magnitude $2\pi/\lambda$ as radius. Constructive interference is obtained if the Ewald sphere intersects with one or more other reciprocal lattice points.

The Ewald sphere in a TEM is somewhat better illustrated in a projection as shown in figure 2.19. In the figure, a simple cubic crystal is ordered with its [100]-axis parallel with the primary electron beam, and a projection of the sphere's interceptions with the reciprocal lattice are shown below. The Ewald sphere intercepts with reciprocal lattice points in several planes, defining the so-called Laue zones.

2.7.3 Kikuchi diffraction

When the primary electron beam passes through the specimen, some of them will get inelastically (diffusely) scattered in the meaning that they will loose energy in the process. These electrons will get deviated from their original path with a spread of about 1° and appear as a diffuse illuminated area around the center spot in the DP. After the first scattering event there is a small chance that the inelastically scattered electrons get elastically scattered by the crystal planes, resulting in an

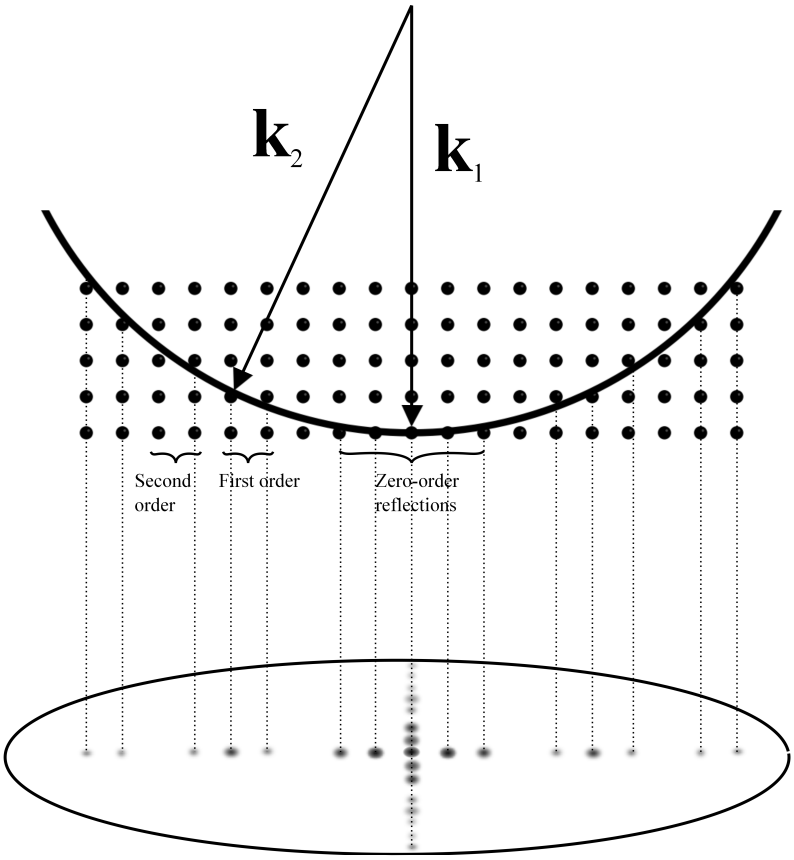

Figure 2.19: The interception between the Ewald sphere and a reciprocal cubic lattice as oriented with its [100] zone parallel with the incident radiation. With the very short wavelength of electrons, the Ewald sphere is very large and hence intercepts with more then one reciprocal lattice point at once. These interception projected down on a plane are how the diffraction pattern is observed in a TEM. For the specific orientation illustrated in the figure, the interception between the Ewald sphere and different lattice planes denote the different Laue zones. These are observed as diffraction spots far from the center. The cross-pattern are only meant to illustrate the 2D-appearance of the DP. In reality the DP would exist all over the disc, but for simplicity, only the cross pattern is included.

contrast variation in the diffusely illuminated area around the center spot. The contrast is present because the intensity of the diffusely scattered electrons falls off very rapidly with angle, and so the number of secondary scattered electrons will be higher at small angles then at large. The effect is illustrated in figure 2.20 where two inelastically scattered rays are considered, one with high intensity (ray 1) and one with low intensity (ray 2). Both rays get diffracted, resulting in ray 1 to the

left and ray 2 to the right of the plane projection. The intensity on the right side is then a sum of ray 2 and the lack of ray 1 who should originally be there if no second scattering had happened. Since ray 1 is more intense than ray 2, a dark area will appear on the right side of the plane projection and a bright area on the left. These areas will be lines as there will be cones of diffracted electrons rather than single rays due to the range of incident **k**-vectors. The cones are called Kossel cones, and the exact Kikuchi pattern in the DP will be the interception line between these Kossel cones and the Ewald sphere [47][44].

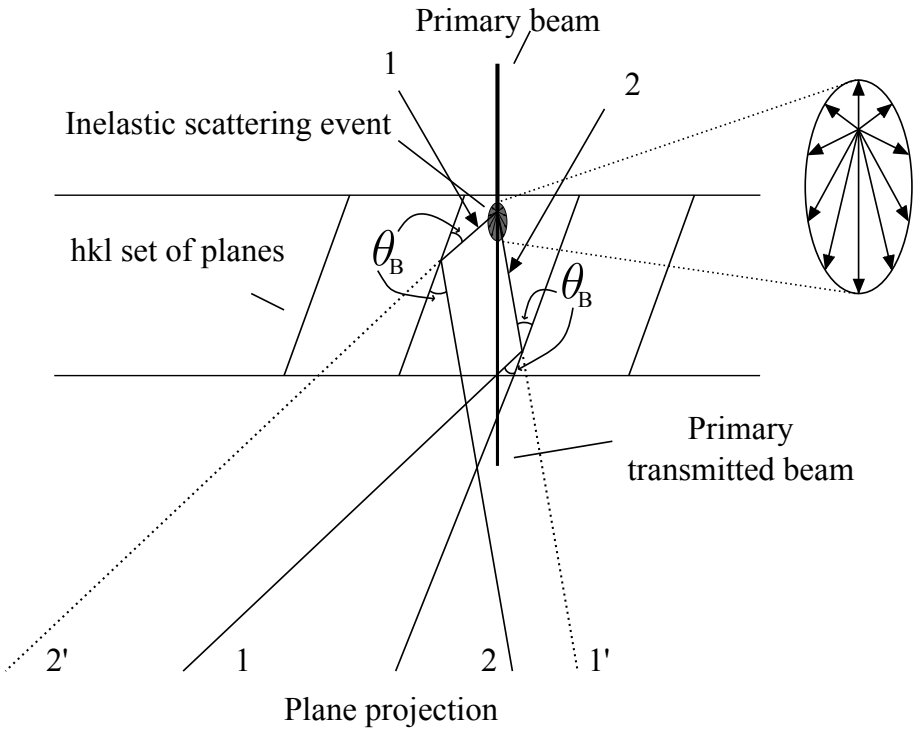

Figure 2.20: A schematic drawing of the creation of Kikuchi lines. The inelastically scattered beam is illustrated by two rays, 1 and 2, where ray 1 has high intensity and ray 2 has low. After both rays have been elastically scattered they leave a bright line to the left of the plane projection and a dark line to the right. There will be a line rather than a dot, as suggested in the image, because there will be cones of diffracted electrons rather than single rays due to the range of incident **k***-vectors*

Kikuchi lines are a very powerful tool when operating a TEM. They may be used for navigation in reciprocal space as well as for doing accurate adjustments of the orientation of the sample. The spacing between a pair of dark and bright Kikuchi lines can be used for accurately determining the spacing between crystallographic planes and can be shown to be proportional to the scattering angle 2θ [48]. With

very small scattering angles used in electron diffraction, these two lines may therefore be used as an accurate measure of the orientation of the crystallographic planes as these are projected into the observation plane between the pair of lines. The latter is a extremely useful property as it causes the Kikuchi lines to get symmetrically aligned according to the primary beam spot when the specimen crystal is oriented with its along a zone axis parallel to the incident electron beam. The very small spacing between a pair of Kikuchi lines can also be used for very accurately adjusting the tilt of a specimen. Compared to the diffraction spots who are approximately constant even for large variations in tilt, the Kikuchi pattern moves a lot even for tiny variations in tilt [47].

To summarize, the Kikuchi diffraction pattern works as a very detailed map of the reciprocal space and may be used for extremely accurate navigation. It may also be a useful source of information as its form is dependent on crystallographic properties of the specimen.

2.8 Electron Energy Loss Spectroscopy

When the primary electron beam hits the specimen, we know from earlier that some of them are inelastically scattered from the atoms in the sample. Electron Energy Loss Spectroscopy (EELS) is the analysis of the energy spectrum of these inelastically forward scattered electrons, where the intensity determines by arbitrary units the density of electrons with the given energy. By investigating the amount of energy lost in the interaction with the specimen, it is possible to obtain information about the specimen including atomic structure, dielectric response, free electron density and thickness among others. EELS may be used as a complementary technique to Energy Dispersive Spectroscopy (EDS) and Wavelength Dispersive X-Ray Spectroscopy (WDS), however EELS has advantages in both collection efficiency and resolution. The resolution of EELS may be as good as < 1 eV, and the collection efficiency is about 50% for EELS compared to $\sim 10^{-2}$ for EDS detectors [44][49].

2.8.1 Geometrical Setup

The electron energy loss detection system is based on very simple electro-magnetic principles. A magnetic prism is placed directly beneath the main column in such a way that it bends the incident beam onto a detector. Based on the energy of the incident electrons, the degree of bending will vary from electron to electron according to the Lorentz force and a spectrum will thus be generated in the detector.

An aperture is placed in front of the magnetic prism to prevent any Bragg scattered electrons from entering the system. In this way, only the non scattered and inelastically scattered electrons are allowed to enter the prism.

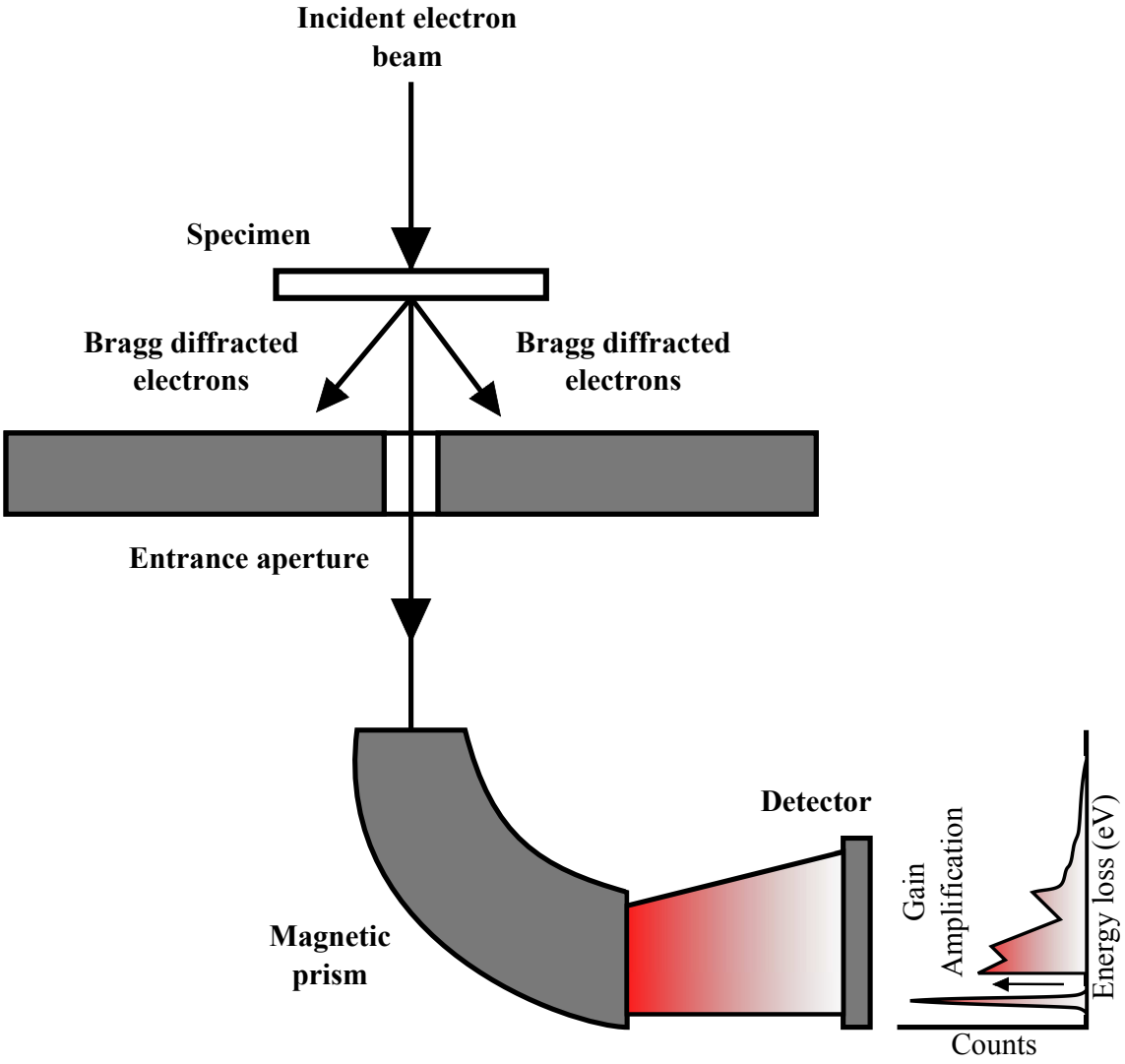

Figure 2.21: The figure shows a setup of a typical EELS-module. The transmitted beam is shown to be cut by an aperture, allowing only the non-scattered and the inelastically scattered electrons to pass. The beam is further bent by a magnetic prism and reflected onto the detector. Electrons with different energies will be bent differently, and hence a spectrum is obtained at the detector (which show the different energies). Drawing based on a figure in [44].

2.8.2 Understanding The Spectrum

To understand the energy spectrum obtained by EELS it is necessary to investigate how it is formed. Electrons are as known deflected in the magnetic prism (figure 2.21) according to how much energy they have lost in their interaction with the specimen. Electrons having lost little energy is deflected less that than those having lost much energy, and hence the latter causes a broadening of the spectrum. Since different kinds of interactions causes different energy losses, it is possible to recognize the different scattering events in the obtained spectrum.

In the following, some of the effects creating the spectrum will be discussed and possible utilizations will be mentioned.

2.8.2.1 The Zero Loss Peak (ZLP)

The zero loss peak (ZLP) is the peak in the energy spectrum which represents the non-scattered electrons. Without any scattering, no energy is lost and the peak is therefore centered around zero with a broadness defined by the quality of the electron source of the microscope. With a relatively thin sample, the ZLP will by far be the largest peak in the spectrum raging orders of magnitude above the second most intensive peak.

2.8.2.2 Plasmon Peak

The plasmon peak is usually placed between 5 and 50 eV and is created when the incident electrons interact with the specimen, creating a plasmon. A plasmon is as the word suggests a wave in plasma, which in the context refers to a wave in the free electron gas of the sample. Although plasmons may occur in any material, they are most common in metals because of their large Fermi surfaces resulting in a large free electron density. Also, plasmon peaks from metals are usually rather sharp while the plasmon peaks from non-conductors tens to be more diffuse. Plasmon peaks may appear several times if the electron is interacting with the plasmon several times.

The incident electrons can be shown have a classical mean free path in the specimen before they tend to interact with a plasmon. If this mean free path is known, it can be used to calculate the thickness of the specimen by comparing the intensity of the area containing both the plasmon peak and the ZLP (Low loss area) with the ZLP. If the specimen is thin enough to only allow one plasmon interaction per electron, the following relationship can be used to calculate the thickness;

$$t = \lambda \frac{I_l}{I_0} \tag{2.21}$$

Here t is the thickness, λ is the plasmon mean free path of the electron, I_l is the intensity of the low-loss area and I_0 is the intensity of the ZLP.

2.8.2.3 High Energy Peaks

The high energy loss peaks appearing in the high energy area above $\approx$ 50 eV are created by the primary electron's interaction with the core shells of the specimen contained atoms. The incident electron knocks out one of the electrons in one of the tightly bound shells transferring some of its energy in the process. The amount of energy transferred is dependent on the host element and the core shell (K, L, ...) and will be readable in the spectrum. Since the binding energy of the mentioned shells are characteristic for different elements, it is possible to get compositional information about the specimen. High energy-loss EELS is thus a very powerful tool for characterizing and has an advantage over EDS by better resolution and minimum detection limit.

Chapter 3

Experimental

3.1 Materials and hardness measurements

3.1.1 The Materials

In this master thesis, three different extruded made alloys have been studied. The three alloys are typed 6xxx as their main alloying elements are magnesium (Mg) and silicon (Si). They are all so-called industrial alloys, which means that they in addition to the main alloying elements include small amounts of manganese (Mn) and iron (Fe). The difference between the investigated alloys is that they include different amounts of the main solute elements, namely Mg and Si, but with equal Mg/Si-ratio. The alloy of the highest solute content is denoted HS, the alloy with the medium amount of solute is denoted MS while the one with the lowest solute content is denoted LS. More detailed information about the content of the alloys is found in table 3.1. The alloys are picked because they are equal in composition, but with different Mg+Si content. However, unfortunately the MS alloy does have a slightly different Mn content compared to the other two, but this difference will be neglected, as it is not believed to affect the investigated properties of the alloy.

3.1.2 Scope

The purpose of this master thesis is to study the clustering process which takes place in 6xxx-alloys during natural aging and its effect on the final condition after artificial aging. As the clustering process influences the hardness evolution of the aluminum

Table 3.1: Content of alloying elements in the different alloys in wt.%

Alloy type	Al	Mg	Si	Fe	Mn
LS	98.93	0.37	0.45	0.2	0.05
MS	98.511	0.555	0.718	0.2	0.016
HS	98.05	0.75	0.95	0.2	0.05

alloys [6], the hardness will be measured during NA in order to obtain information on the clustering kinetics. All three alloys are further measured for hardness after subsequent AA and two of them are studied in the transmission electron microscope to see how the initial clustering affected the final microstructure. The experiment was divided into three parts:

I. Study *the direct effect* of clustering on the hardness evolution of the three alloys during room temperature-storage before AA. This is done by solution heat treating the alloys at 540°C and then measuring their hardness as a function of time only.

II. Study *the effect* of the clustering process on the precipitation hardening after artificial aging. This is performed by solution heat treating several samples, then storing them for different amounts of time before they are artificially aged and subsequently measured for hardness. The samples undergo the following treatment:

   i) Solution heat treatment for 60 minutes at 540°C
   ii) Water quench
   iii) Storage a time t at room temperature (RT) $\sim$ 20°C
   iv) Artificial aging at 175°C for 36 hours
   v) Water quench
   vi) Ground by silicon carbide (SiC) grinding paper
   vii) Hardness measurements

III. Study the effect which the clustering has on precipitation after AA through micro-structural analysis by transmission electron microscopy. The two most extreme alloys, the HS and the LS alloys, will be studied through quantification of precipitate number densities, average lengths and cross section areas. A study of the precipitate types appearing at different conditions was performed in order to prove any relation between alloy hardness and precipitate type.

The solution heat treatment was performed using a salt bath and the artificial aging was performed using an oil bath. The temperature of both baths were measured to be within ± 2 °C of the quoted value using a Digitron Instrumentation K-type thermocouple.

3.1.3 Hardness measurements

3.1.3.1 Experimental procedure of hardness measurements

The Vickers hardness measurements were carried out on a Matzuzawa DVK-1S unit using 1000 gram load, 15 seconds loading time and a load speed of 100 μm/second. The equipment was consistently manually calibrated each time it was being used to obtain comparable results. This is actually very important, due to the sensitivity of the measurements to calibration. Differences in the way a sample is measured can often be more decisive than the physical effect that one desire to measure in the sample. It is therefore of uttermost importance that the preparation of the sample and the method of performing the measurement is performed absolutely consistently.

3.1.3.2 Sample preparation

The samples were initially cut into pieces of thicknesses >3 mm. The samples were then roughly ground by using a Knuth rotor grinding device mounted with silicon carbide (SiC) grinding paper. The exact roughness of the grind is not of great importance at this point, since the purpose of the grind only was to get rid of major unevenness on the sample surface. Since there were many samples, they were marked with a number and a label to recall the type of the sample using a sharp diamond-tipped scratcher.

With the hardness part of the experiment being roughly divided into two, the preparation of the samples used in part I and part II described in section 3.1.2 were a bit different. They will therefore be described separately.

I. It is very important that the surface of the sample is totally flat when it is to be measured for hardness. The samples therefore had to undergo a fine grind before they could be measured. Since grinding of the samples takes a couple of minutes to execute, it was performed before the samples were solution heat

treated. In this way the samples could be carried straight from the SHT to the hardness measurement device, and hence the RT-storage time could be kept at a minimum. However, the major drawback with this method is that a sample undergoing SHT has a tendency of getting faint. This is strongly unwanted due to the accuracy in the hardness measurements, and hence a grind after SHT was sometimes necessary. The fine grind used on the samples in this part of the experiment was performed using a silicon carbide grinding paper with a maximum of 1400 grains per cm^2.

II. The samples used in this part of the experiment were initially prepared as described in the beginning of this section. However, the need for a fine grind before going into the solution heat treatment bath was in this case unnecessary due to to the fact that these samples were subsequently going to be artificially aged. The samples were, however, ground before being measured for hardness using silicon carbide grinding paper with 4000 grains per cm^2. The time between AA and the hardness measurement was of no importance, since the alloy hardness does not evolve during RT storage after AA [2].

3.2 TEM

This section is dedicated to how the TEM specimens were prepared as well as how the microstructural analysis was executed.

3.2.1 Sample preparation

In transmission electron microscopy a good sample is crucial in order to get good images. Since operating the microscope is a difficult and very time consuming process, a good sample might save you a whole lot of work and more importantly, much frustration. Therefore a necessity for being a great microscopist is to have the patience and skills required to make good samples.

In the case of the aluminum samples used in this master thesis, the samples were made from the already existing alloy conditions used for hardness measurements. The following procedure was followed in the making of the TEM samples:

I. The already existing pieces of material used for hardness measurements were cut into thin slices using a Struers Accutom-50 mounted with a silicon carbide (SiC) blade. This was done instead of just grinding down the original sample

in order to increase the number of TEM-specimens as the original samples were very small. The process is anyway recommended because cutting is a much less time consuming process than grinding since the cutting device is able to cut very thin slices.

II. The thin aluminum slices from the previous step were further ground down to a thickness of about 100 μm using silicon carbide grinding paper of decreasing coarseness until a coarseness of 4000 grains per cm^2 was reached. It was important to decrease this coarseness in order to keep the amount of introduced dislocations to a minimum, as these will ruin the sample.

III. After the originally thin slices were ground down to a thin smooth foil, disks with diameter of 3 mm were cut out from the foil in order to get the aluminum to fit in the TEM specimen holder.

IV. The thin disks were finally electropolished using a Struers TenuPol-5 with an electrolyte held between -20 and -30°C made from one part nitric acid and two parts methanol. The electropolisher was operated in a single flow mode with voltage 20 V, a light stop value of 120 and a pump flow rate of 38. The electropolishing is a method of oxidizing the samples in order to thin them down to a thickness of $\sim$ 10 nm. At such a thickness, the samples are ready to enter the TEM.

3.2.2 The microscope

The microscope used for this thesis was a Philips CM30 TEM with a LaB_6 electron source operated at 150 keV. The instrument could perform imaging at resolutions raging from low magnification up to 750000x, making it an excellent general analytical facility. The specimens were placed in a double tilt holder in order to tilt the sample in both directions. The holder is able to tilt the sample 45° in one direction and 30° in the other, giving it a rather large span. The microscope is also equipped with a Gatan model 601 parallel electron energy loss spectrometer (PEELS) with EL/P software which was used to perform the thickness measurements. Unpublished internal research has shown that thickness measurements done with the microscope used for this thesis have an error approaching 20%.

3.2.3 TEM on aluminum

When investigating precipitates in aluminum by TEM, it is a necessity to adjust the tilt of the specimen such that one of the [100]-zones are parallel with the incident electron beam. This is because the precipitates in 6xxx alloys are elongated along this direction in the matrix and have cross sections perpendicular to it [24] [25] [28]. The precipitates oriented like this will cause diffraction contrast, making their unit cell possible to observe. The precipitates oriented perpendicular to the viewing direction will also be visible due to the coherency strain field imposed by these on the surrounding matrix. A typical TEM picture is shown in figure 3.1 where (a) shows a typical TEM image of a 6xxx alloy and (b) shows a diffraction pattern of its [100]-zone axis. The Kikuchi lines can also be observed to be symmetrically aligned relative to the center spot. This indicates that the incident beam is aligned exactly along the zone axis of the crystal. In figure 3.1a the precipitates growing perpendicular to the incident electron beam can be seen only in terms of their cross sections as dark spots. The precipitates growing in the perpendicular directions are seen on the picture as needles being perpendicular to each other.

3.2.3.1 Searching for the zone

As mentioned above, the sample has to be aligned with one of the [100]-zones in the direction of the electron beam in order to see any precipitates. Therefore, much of the work done on the TEM is based on adjusting the sample according to this tilt. This might be searching through different grains for this zone axis or just fine tuning the tilt when hunting for the perfect picture. The first is perhaps the most challenging, as the sample may initially be far from the zone with little hint of what way to tilt. In both cases, knowledge of the Kikuchi line pattern is very helpful as it tells you what way to tilt. It might, however, seem a bit too challenging to interpret these patterns, but in the case of aluminum, a great deal of knowledge is not needed in order to find the zone. From section 2.7.3 it's known that the Kikuchi lines will appear in pairs resulting in so-called Kikuchi bands. The trick for finding the [100]-zone is then to tilt the sample towards major convergences of these bands as they will converge in different zones. Even with the rather restricted tilt possibility of the specimen holder, this approach should easily lead to one of the three zones [100], [110] or [111]. If either [110] or [111] is discovered, [100] can not be aligned in that grain and a different grain has to be investigated. The latter is because TEM specimen holders usually don't allow for a larger tilts than 45° and the [100] axis is 45° and ≈55° away from the [110] and [111] axes respectively. The Kikuchi patterns for the three above mentioned zone axes are shown in figure 3.2

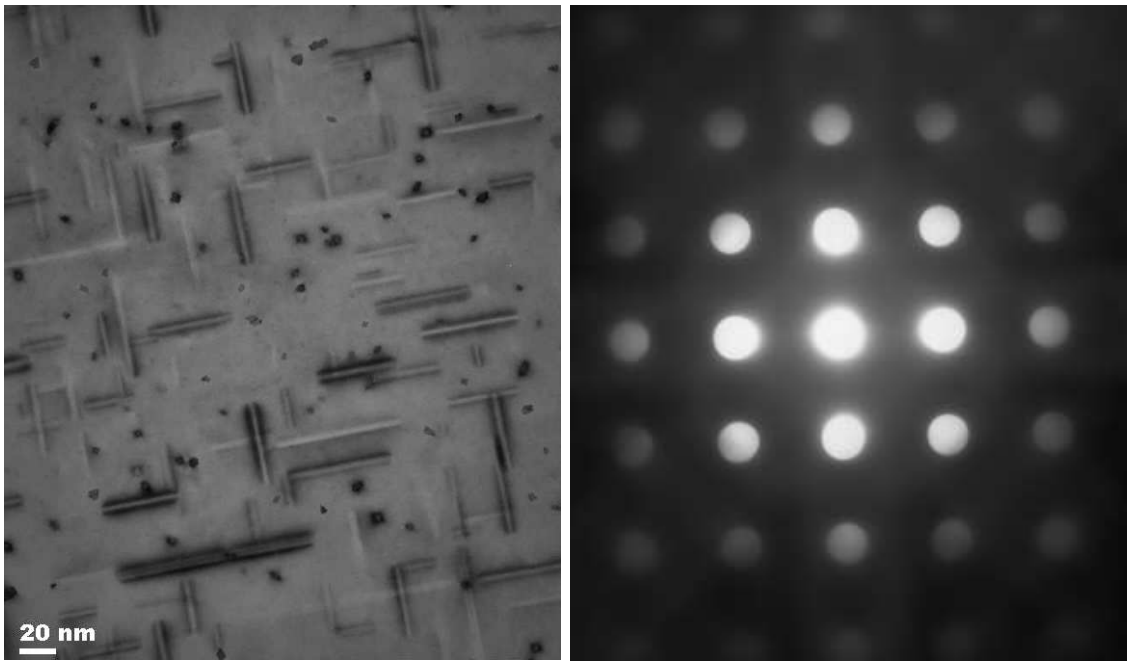

(a) *(b)*

Figure 3.1: A typical TEM overview picture of an aged 6xxx Al-alloy (a). The dark dots are the precipitates in projection and the needles are the precipitates seen from the side. (b) shows a diffraction pattern of the [100] zone-axis in aluminum. It is necessary to be aligned with this axis to see the precipitates due to their ordering relative to this direction. The Kikuchi lines can be observed to cross over the center spot, meaning that the zone is perfectly aligned.

together with the respective diffraction spot pattern. The patterns are generated using Ideal Microscope 1.0a.

3.2.4 Execution of the analysis

One purpose of the TEM analysis was to find the average number density, length, cross section and volume fraction of the precipitates in the five investigated samples. A problem with TEM is that you get a very poor sampling rate as the investigated specimens are very small (see section 3.2.1). To make things worse, the investigated area captured on each image is even smaller as the magnification required to see the precipitates clearly, is very high. As the lowest magnification used in these studies is 144k, the area of a typical picture gets only ≈300x400nm. Together with a typical thickness of ∼50 nm, the total investigated volume per picture gets very small.

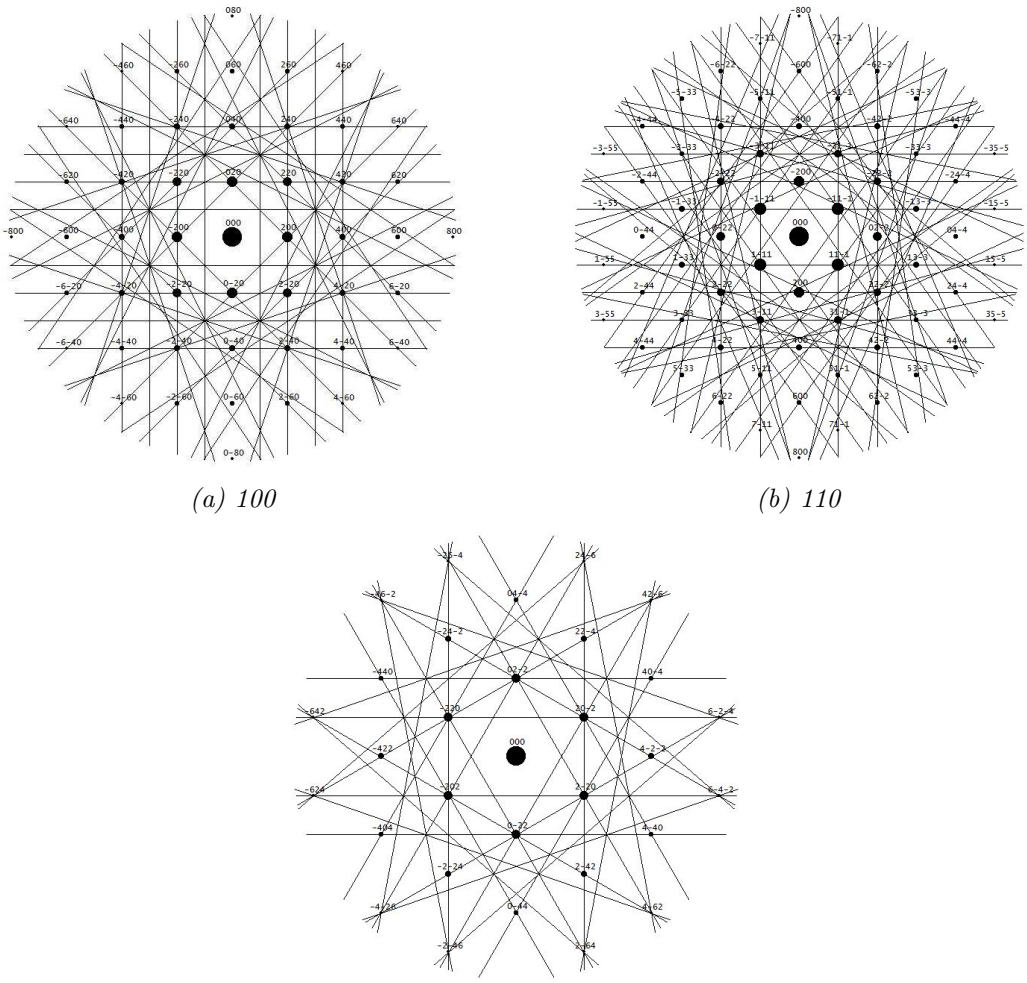

(a) 100 *(b) 110*

(c) 111

Figure 3.2: The Kikuchi patterns together with their respective diffraction spot patterns for the the zones (a) [100], (b) [110] and (c) [111] as seen in aluminum. The patterns are generated using Ideal Microscope 1.0a.

With such a small volume of investigation comes the need of statistical sampling. Each of the quantities found through the TEM studies in this thesis are therefore an average over 10 pictures. The pictures used for measuring number density and average length taken at 144k, and the pictures taken to measure the cross section and to recognize the precipitate types taken at a magnification of 491k. For the low magnification pictures, this results in ∼1000 precipitates counted for each sample and ∼100 for the high magnification pictures.

Since TEM pictures show the projection of the specimen, it is necessary to

know the thickness of the sample to calculate the number density of precipitates. All the TEM pictures taken for this purpose was therefore taken together with an EELS measurement in order to get as exact data as possible. For the EELS measurements a mean free path of 111 nm was used for 150 keV electrons and an error of 20% was expected for these measurements. These values are taken from earlier unpublished calculations done for the microscope.

The volume fraction (VF) of precipitates in the investigated alloys is not something that can be explicitly extracted from the TEM images. Instead, this quantity can be found by simply multiplying the average cross section, length and number density.

$$VF = \langle CS \rangle \cdot \langle l \rangle \cdot \langle \rho \rangle \tag{3.1}$$

Here $\langle CS \rangle$, $\langle l \rangle$ and $\langle \rho \rangle$ denote the mean cross section, length and number density respectively.

3.2.5 Picture interpretation and counting procedure

The precipitates were counted by using an in-house software that detects continuous areas of color in the picture and returns the number of such areas, their length and area, the area of the picture and standard deviations of these variables. The volume fraction are further calculated from these quantities according to the relation in equation (3.1). The quantities desired to measure from the pictures can therefore be found by coloring the precipitates in such a way that the program returns the correct quantity. The pictures have to be colored in four different ways in order to extract the four quantities precipitate length in two directions, number density and cross section. It is necessary to count the two length-directions separately because the precipitates in these directions overlap. Since the program is only able to measure continuously colored areas, it can not distinguish overlapping precipitates. Examples on how the precipitates were marked is shown in figure 3.3.

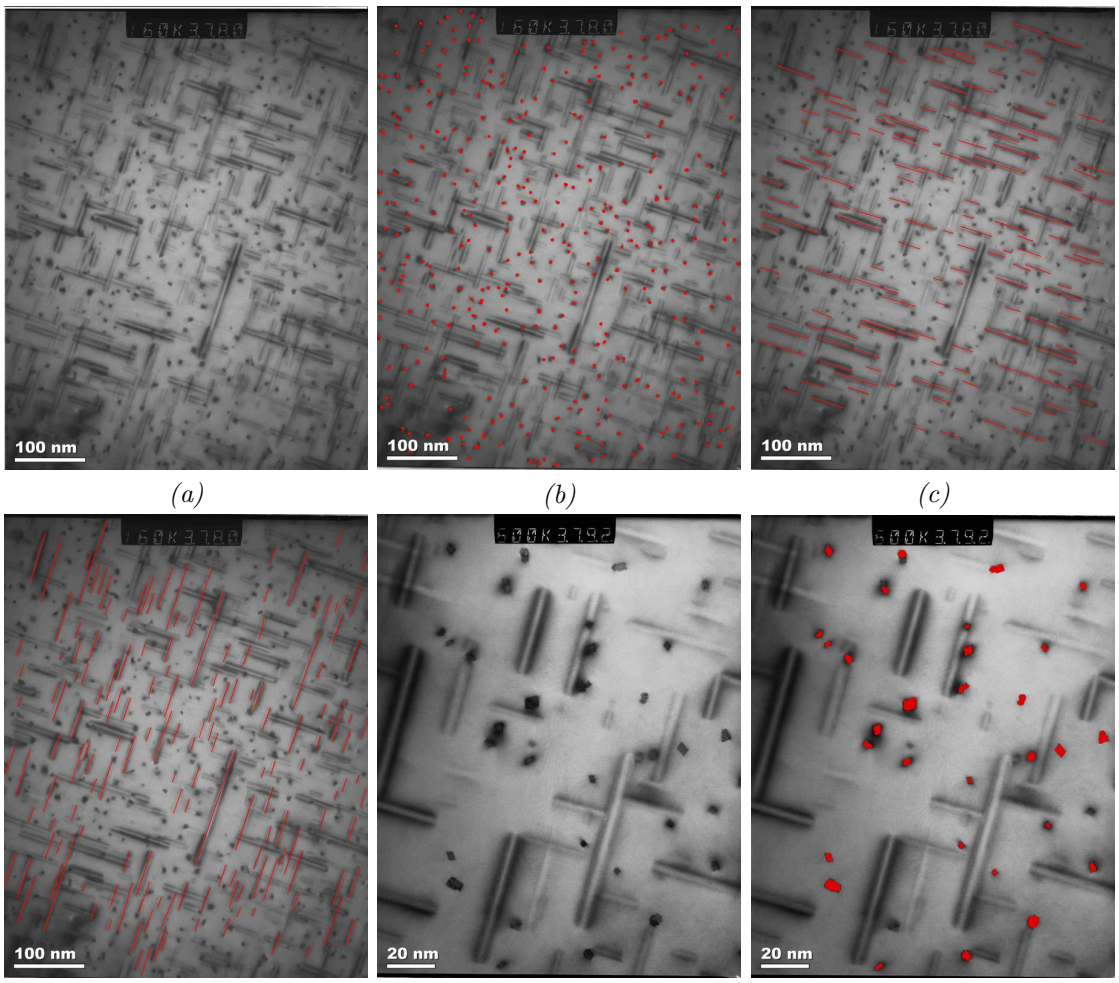

(a) *(b)* *(c)*

(d) *(e)* *(f)*

Figure 3.3: How the TEM-pictures were interpreted in order to find from (a), the average number density (b), precipitate length (c and d) and from (e), the cross section area (f).

3.2.6 Correction procedure

In the 6xxx aluminum alloy series, the main hardening precipitates have needle-like morphology [50]. With the needles varying in length from ∼10 nm to ∼100 nm [32], it is inevitable that some of these are cut during sample preparation as the typical thickness of investigated areas in the TEM is ∼50 nm. These cut needles will appear in the TEM pictures just like any non-cut precipitate, as they are impossible to distinguish due to the fact that TEM images are projection images. This fact causes two problems when interpreting the images.

1) The needles oriented in the viewing direction do actually belong to a larger volume than the investigated one. The thinner the sample and/or the longer the needles, the more pronounced will this effect be. The calculated number density of precipitates will therefore be overestimated as very few of the counted precipitates will be fully reticent in the specimen. The effect is illustrated in figure 3.4 where the dotted lines parallel with the viewing direction illustrate the needles cut this way.

2) As the zone axes seldom are oriented parallel to the viewing direction, some of the needles seen from the side are cut due to the tilt of the specimen. These will therefore appear shorter in the image than what they originally are, and will cause an underestimate in the calculated average length. The effect is illustrated in figure 3.4 where the dotted lines perpendicular to the viewing direction indicate the needles cut this way. However, as the illustration is drawn with one zone pointing into the specimen, it only includes the cutting of the needles in one direction. The tilt of the specimen is usually oriented such that needles in both directions perpendicular to the viewing direction are cut.

To correct for the errors discussed above, it is necessary to apply certain corrections to make the results representative for the actual microstructure. Without going into details on the geometry involved, the equation correcting for the average length $\langle l \rangle$ is given as [51];

$$\langle l \rangle = \frac{\langle l \rangle_m}{1 - \frac{\langle l \rangle_m}{t} \cos\theta \tan\Phi} \tag{3.2}$$

and the equation correcting for the number density is given as [52];

$$\rho = \frac{3N}{At(1 + \frac{\langle l \rangle}{t})} \tag{3.3}$$

where

- $\langle l \rangle$ = the true precipitate length.
- $\langle l \rangle_m$ = the average precipitate length measured in the TEM images.
- t = the thickness of the sample.
- θ = the angle between the orientation of the [010] and [001]-direction relative to the specimen tilt (defining the viewing direction along [100]). If $\theta = 90°$, one of the two directions will lie parallel to the specimen surface and the precipitates pointing this way will not get cut. As an approximation, it's assumed that $\theta = 45°$, meaning that precipitates in both the [010] and [001] directions will get equally cut [51].
- $\Phi = \arccos[\cos\alpha_1 \cos\alpha_2]$ = the angle between the sample normal and the direction of the electron beam. $\alpha_{1,2}$ = the tilt in the two perpendicular directions 1 and 2 respectively.

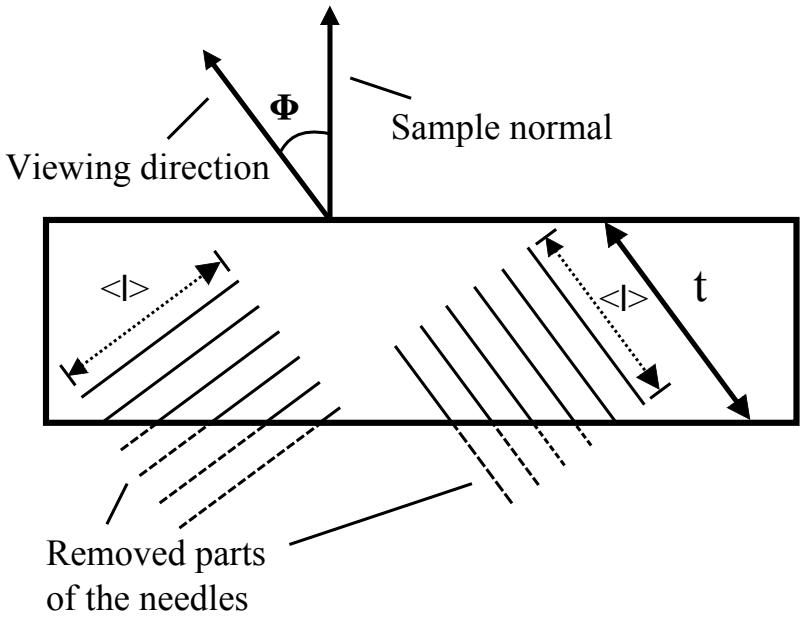

Figure 3.4: The cutting of needle-shaped precipitates due to the thin morphology of the TEM-specimen. Needles cut in both the direction parallel and perpendicular to the viewing direction are shown and the quantity t denote the transition thickness of the specimen.

Chapter 4

Results

4.1 Hardness results

In this section the results from the hardness measurements is presented. The work is a continuation of that described in [9], and relevant results are therefore repeated here.

4.1.1 Hardness after solution heat treatment and natural aging (T4)

In this section the hardness evolution of the three investigated alloys during natural aging are presented. The hardness is given both for long natural aging times with slow sampling rate and for short times with rapid sampling rate. For the case of the long time measurements, the results are presented as a mean of 10 indentations with errors equal to two standard errors. For the rapid measurements, only one indentation was made for each presented data point and hence no basis for statistical error estimates exists.

4.1.1.1 The low solute alloy

The hardness of the low solute alloy as a function of long RT-storage times t is given in figure 4.1. The Vicker hardness of the alloy is observed to increase more or less proportional to the logarithm of time, resulting in a hardness increase of ≈ 14 during the first 3500 hours of RT-storage. although a steady increase, small sudden variations in gradient can be observed between 1 and 12 hours and after 100 hours of NA.

A plot of the hardness evolution for short RT-storage times is given in figure 4.2. It represents how much the hardness fluctuates within the series of measurements that give rise to the first data-point in figure 4.1. It is observed that the increase in hardness is about 1 during the first 150 minutes of RT-storage of this alloy.

4.1.1.2 The medium solute alloy

The hardness of the medium solute alloy as a function of long RT-storage times t is given in figure 4.1. The Vicker hardness evolution is seen to increase very slowly at short times before it after about 30 minutes starts increasing more rapidly. This rapid increase continue for about 10 hours before the evolution returns to a similar state as for short times. The hardness is overall observed to increase from $\approx$40 Vicker hardness at $\sim$ 1 min of RT-storage to $\approx$60 after 1000 hours.

A plot of the hardness evolution for short RT-storage times is given in figure 4.2. The alloy is observed to undergo a minor increase in Vicker hardness during the first 30 minutes of RT-storage. The hardness is then observed to suddenly increase rapidly after about 30 minutes, and this rapid increase is observed to gradually decline during the next three hours. The alloy is observed to increase from $\approx$40 Vickers hardness to $\approx$55 during the first three hours of RT-storage.

4.1.1.3 The high solute alloy

The hardness of the high solute alloy as a function of long RT-storage times is given in figure 4.1. The alloy is observed to undergo a rapid increase in hardness during the very first hours of RT-storage. The slope of the hardness curve then slowly decreases, before the hardness becomes approximately proportional to the logarithm of time after 5 hours. The total hardness increase is observed to be ≈ 35 during the investigated time interval.

A plot of the hardness evolution for short RT-storage times is given in figure 4.2. The measurement is performed in the time interval 3.5 to 210 minutes and supplies the information missing in the early parts of figure 4.1. The hardness is observed to increase in a smooth arc from ≈45 at $t = 3.5$ minutes to ≈72 at t=210 min. The slope of the hardness is observed to decrease during the entire measured time interval.

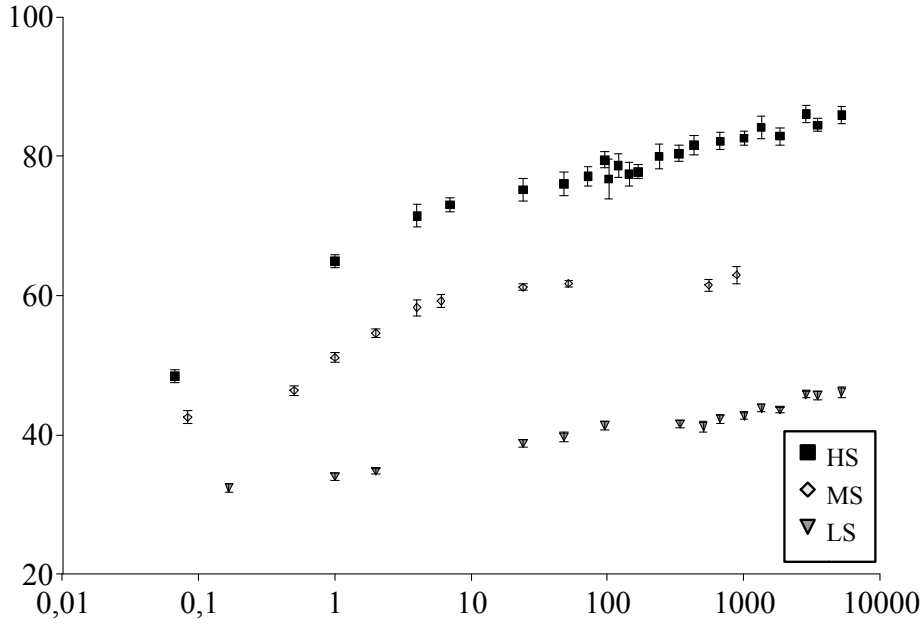

Figure 4.1: The Vickers hardness as a function of RT-storage for the LS-alloy, MS-alloy and the HS-alloy. The hardness of the LS-alloy is observed to increase proportionally with the logarithm of time during the entire time interval, while the hardness MS-alloy is observed to increase very slowly at short times, rapid between ≈1 and 5 hours and then slowly again afterwards. The hardness of the HS-alloy is observed to increase rapidly at times < 5 hours before finally getting approximately proportional with the logarithm of time.

4.1.2 Hardness after solution heat treatment, natural aging and artificial aging (T6)

The results in this section are the hardness of the three alloys after subjected to a T6 treatment (NA+AA) for various times at NA. All hardness values are represented as a function of NA storage times and are given as a mean of series of ten measurements. The error bars are given as two standard errors.

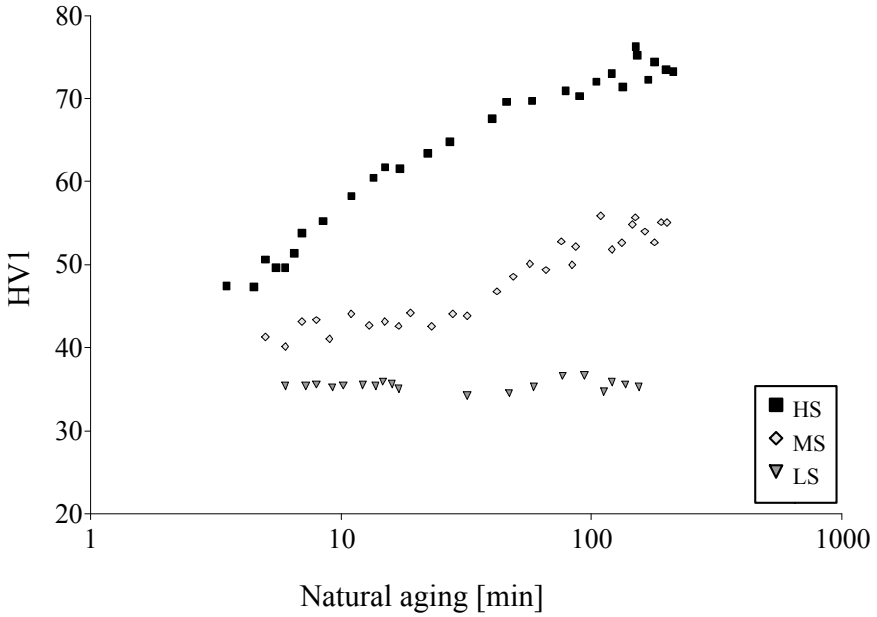

Figure 4.2: The Vickers hardness evolution of the three investigated alloys as a function of short RT-storage times. From the top, the HS-alloy, MS-alloy and the LS-alloy. This plot can be combined with the plot in figure 4.1 to get a more complete overview of the hardness evolution for the three alloys.

The hardness of the LS-alloy is observed to increase more or less proportionally with the logarithm of time for the entire observation period. The only exception is a small bump in the hardness curve at about 1 hour of NA. Here the hardness is seen to increase rapidly before falling back to the trend for larger times. The total hardness is observed to increase from about 70 to 90 Vicker hardness during the investigated time interval.

The MS-alloy is seen to rapidly increase in hardness as a function of NA for storage times shorter than ≈30 minutes. The hardness is then observed to decrease for prolonged NA before it flattens out as the NA times get very long. It increases from about 100 to 110 during these 30 first minutes before it drops back to 100 during the next few hours. The hardness is then, in total, not observed to change noticeably between no NA and long NA.

The hardness of the HS-alloy is observed to decrease rapidly from ≈125 to ≈115 for NA shorter than one hour. It then stays more or less the same between ≈1 and 100 hours of NA before a clear increase is observed which continue for the remaining measured NA times. After about one year of natural aging, the hardness is observed to almost have reached the maximum hardness obtained for very short NA.

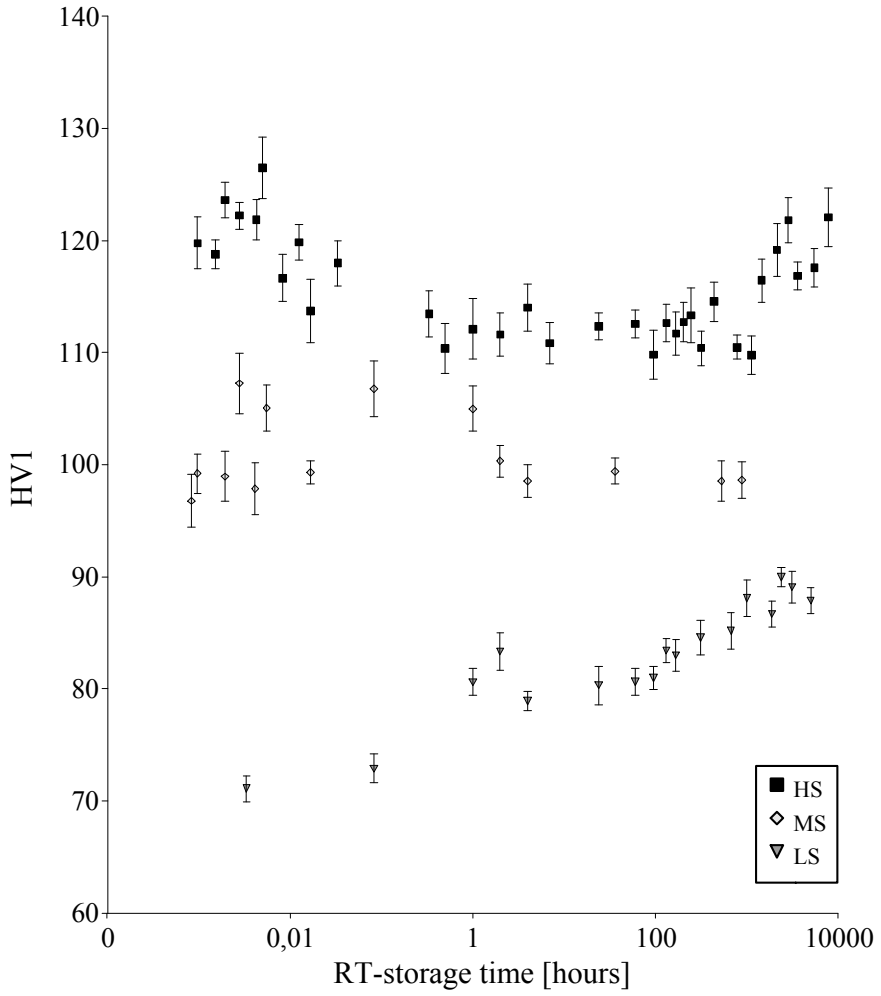

Figure 4.3: The Vickers hardness after NA + AA for the three investigated alloys as a function of NA time. From the top down: the HS-alloy, MS-alloy and the LS-alloy. Each point is a mean of ten measurements and the error bars are given as two standard errors.

4.2 Microstructural results

In order to find a correlation between hardness values and microstructure, TEM-investigations were performed on selected conditions of the HS and LS-alloy. The sample conditions were selected according to the extrema of the hardness curves at a specific point in time. More extreme points may thus be observed on the curves, but these are obtained after the selection of TEM samples and are hence not investigated. Three samples from the NA+AA heat treatment were chosen for the HS-alloy and two for the LS alloy. Due to time restrictions, the MS-alloy was not investigated by TEM.

By investigation of the hardness curves in figure 4.3, HS-samples at short, intermediate and very long storage times were chosen. More precisely samples stored at 18 seconds, 7 hours and 119 days with hardness values of 126.47, 110.84 and 121.8 respectively. For the LS-alloy, the chosen samples were stored 12 seconds and 209 days with hardness values of 71.09 and 87.85 respectively. Typical TEM images for the selected conditions for the HS-alloy are shown in figure 4.4 and for the LS-alloy in figure 4.5. Qualitative numbers of the number density, average length, cross section and volume fraction of the precipitates for the investigated samples can be seen in table 4.1, 4.2 and figure 4.6.

Table 4.1: Qualitative numbers of the number density, average length, cross section and volume fraction of the precipitates in the HS-alloy. The errors are given as two standard error generated from 10 different picture averages.

Storage time (hours)	Needle length (nm)	Number density (μm^{-3})	Cross section (nm^2)	Volume fraction (10^{-3})
0.005	31.11±1.3	44844±5013	6.82±0.71	9.51±1.44
7	59.37±1.69	11789±840	13.95±1.04	9.76±1.05
2856	43.16±1.38	27849±1040	11.26±1.11	13.534±1.49

A difference in microstructure can be observed directly from the images taken at the three different conditions for the HS alloy. Short NA are seen to result in a fine microstructure with many short precipitates with small cross sections, while for prolonged NA, the microstructure is seen to greatly coarsen before it again gets finer for even longer NA. The evolution of this microstructure is clearly seen in figure 4.4 (d), (e) and (f) where the cross section can be observed to have a

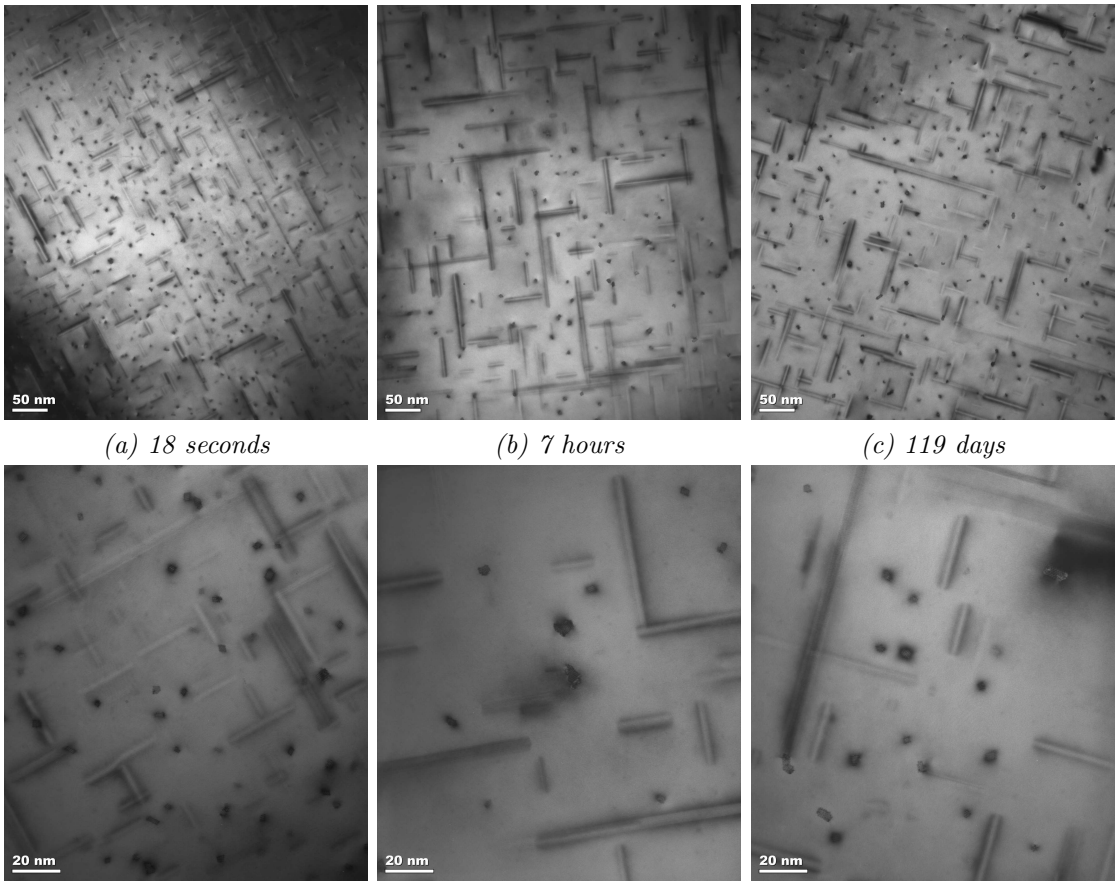

(a) 18 seconds *(b) 7 hours* *(c) 119 days*

(d) 18 seconds *(e) 7 hours* *(f) 119 days*

Figure 4.4: TEM images of the microstucture of the HS alloy. (a)-(c) are taken at low magnification while (b)-(f) are taken at high magnification. The sample used for pictures (a) and (d) has been naturally aged for 18 seconds, the sample used for pictures (b) and (e) has been naturally aged for 7 hours, while the sample used for picture (c) and (f) has been aged for 119 days.

small → *large* → *medium* pattern, the average length a *short* → *long* → *medium* pattern and the number density a *high* → *low* → *medium* pattern. This evolution is better shown in the plots (a)-(c) in figure 4.6 where the microstructure shows a *fine* → *coarse* → *medium* pattern for all the three calculated quantities. This volume fraction is observed to be approximately equal for the samples stored 18 seconds and 7 hours at room temperature, but is observed to increase as the samples are stored even further.

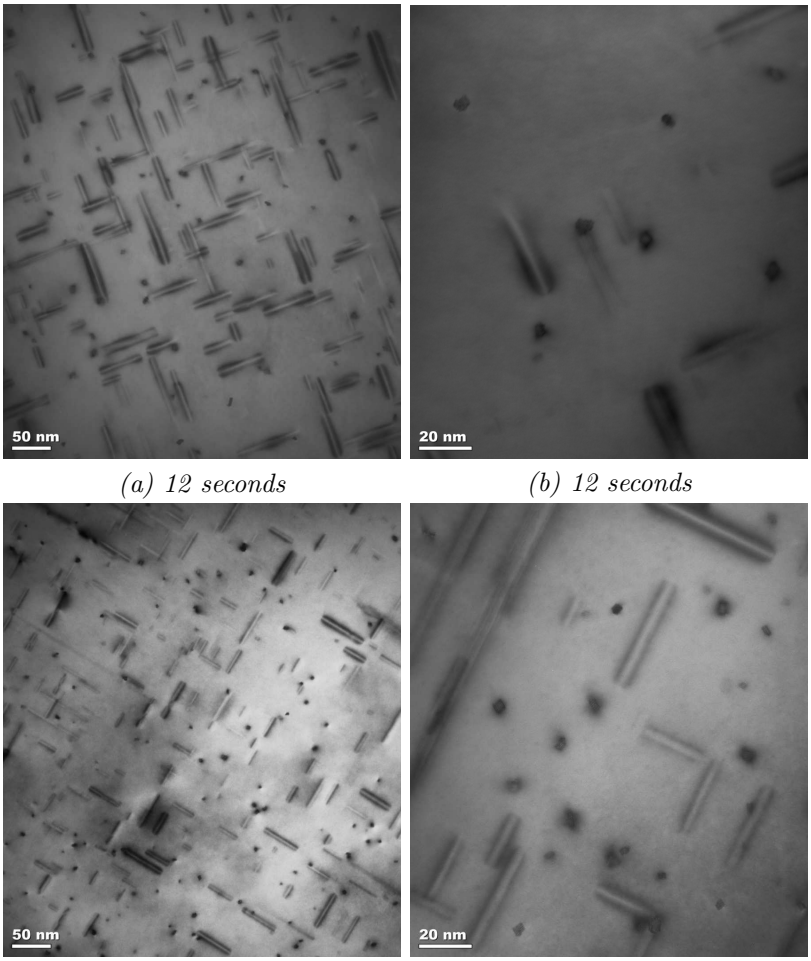

(a) 12 seconds *(b) 12 seconds*

(c) 209 days *(d) 209 days*

Figure 4.5: TEM images of the microstucture of the LS alloy. (a) and (c) are taken at low magnification while (b) and (d) are taken at high magnification. The sample used for pictures (a) and (b) has been naturally aged for 12 seconds while the sample used for pictures (c) and (d) has been aged for 209 days.

Similar to the HS-alloy a difference can also be observed in the TEM pictures in figure 4.5 taken at different conditions for the LS-alloy. The microstructure can be seen to get finer for prolonged NA as the precipitates gets smaller and more numerous. A more detailed analysis are shown in figure 4.6 and in table 4.2 which shows a clear *coarse* → *fine* evolution for increased NA. The Volume fraction is not observed to vary noticeably between the two conditions.

Table 4.2: Qualitative numbers of the number density, average length, cross section and volume fraction of the precipitates in the LS-alloy. The errors are given as two standard error generated from 10 different picture averages.

Storage time (hours)	Needle length (nm)	Number density (μm^{-3})	Cross section (nm^2)	Volume fraction (10^{-3})
0.003	57.04±3.04	5259±630	18.67±2.12	5.6±0.97
5016	43.31±3.36	13356±1407	9.32±1.17	5.39±0.98

4.2.1 Precipitate types

In addition to measuring the average size and number density of the precipitates, an investigation of their types were performed. Their unit cell parameter and orientation in the matrix were compared to the data for known precipitates listed in section 2.5 to prove their type. The precipitates were found to be dominated by β" for both alloys at all conditions, with some precipitates recognized as β' and B'. These latter, however, appeared randomly with no preference to either alloy type nor specific NA.

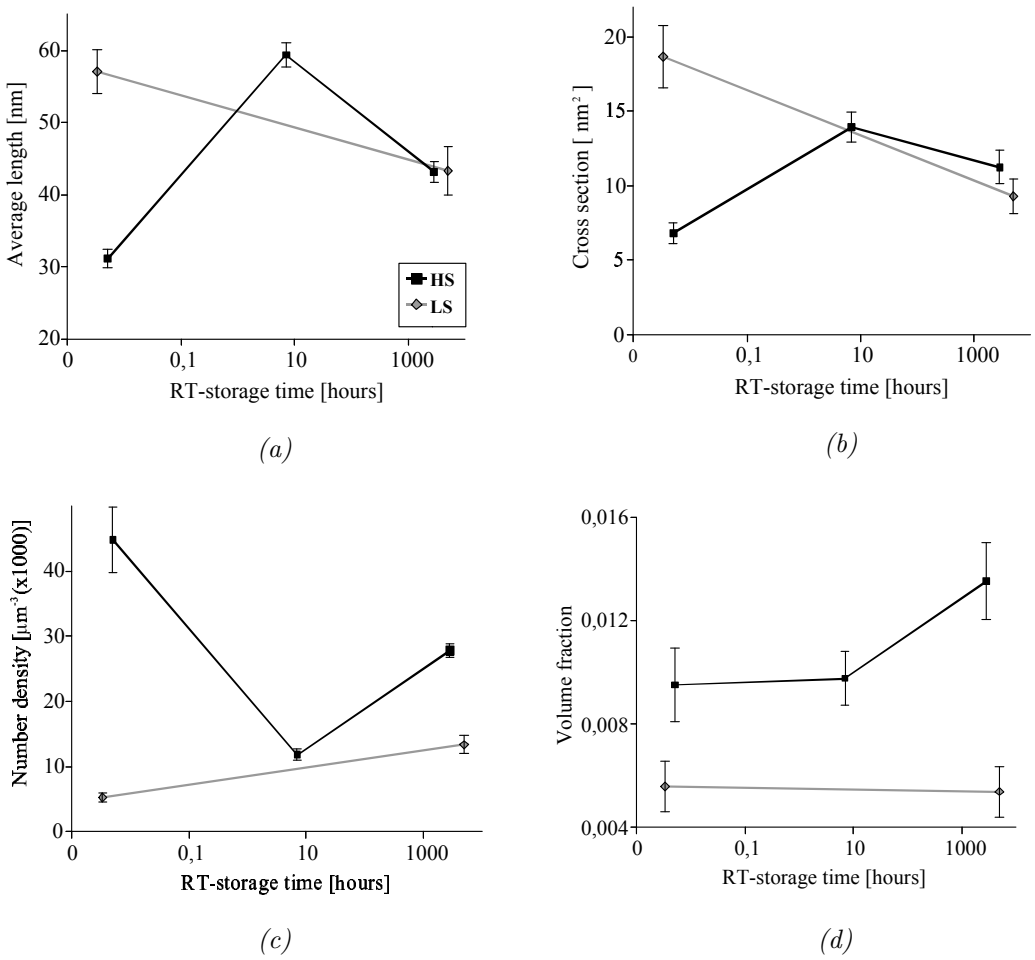

Figure 4.6: An overview of the evolution in microstructure for the LS and the HS alloy as a function of NA time. (a) the evolution in average precipitate length, (b) the evolution in average cross section and (c) the evolution in precipitate number density. (d) the volume fraction of precipitates in the respective alloys (obtained by multiplying the other three quantities).

Chapter 5

Discussion

5.1 Relevant DFT results

The theory of spinodal decomposition (2.4.3.1) gives a useful description of barrier free aggregation. For example studies by I. Sato et. al. [53] have showed that the theory of spinodal decomposition can describe the behavior observed in AlMg-alloys with Mg content of 5% and more. Although useful, the theory doesn't give any explanation for why chemical potential changes with composition in the first place. In other words, it does not answer the question of what is causing the phase separation?

A possible explanation of barrier free aggregation might have been found in the previous work done by the author, where a DFT-based model on solute diffusion in aluminum was created [9]. The fact that Mg fills up more space than Al in the Al-matrix, and Si less, causes Mg to expand the matrix and Si to contract it. It was discovered that its energetically favorable for Mg to diffuse into areas of the matrix with less external pressure than into areas with more, and the opposite for Si. A trivial result in some ways since it is most energetically favorable for the system to be in a non-pressurized condition, and therefore to cluster Mg and Si to neutralize the stress they cause on the matrix. Hirozawa et. al. [54] showed in 2007 through first principle calculations that the clustering of Mg with Si was associated with a barrier, causing the arrangement to be fairly stable.

Even if the most favorable condition for the two alloying elements is to cluster together, the process of clustering is not only based on the final arrangement, but also on the process of getting there. It was shown in [9] that the two elements can be considered as being under different external pressure from the surrounding matrix, as Mg experiences a positive pressure and Si a negative pressure. When the two atoms then approaches each other, they will actually be repulsive to each other because of their different effect on the matrix. Mg will be attracted to Mg rather than Si and the other way around. Why this is so can be understood by an analogy with the ancient Greek battle formation *phalanx*. When the ancient Greeks went into battle, they fought in a tight formation called a phalanx in order to increase their strength against enemy attacks. Every man in the phalanx carried his shield in order to not only protect himself, but also to protect the man to his left. This caused the relative defensive strength of the phalanx to be higher as a unit compared to the sum of each man fighting on his own. The same argument can be used in order to explain clustering of equal solute elements. Considering i.e. two magnesium atoms at a large distance from each other. They would both experience maximum stress from the surrounding matrix as they don't fit into the matrix. On the other hand, if they are close to each other, they can co-operate against the external pressure and thus reduce the relative external pressure caused on each atom. A schematic illustration of this argument can be seen in figure 5.1.

The above argument turns the original picture of clustering around, making it energetically favorable for Mg atoms to diffuse against other Mg atoms rather than towards Si. The conclusion from [9] is that the size difference of the two alloying elements makes it favorable for them to lump together separately, making Mg-rich zones and Si-rich zones. This model thus gives an atomistic explanation for barrier free aggregation based on a simple size difference argument. A plausible description for the concentration dependent chemical potential used in the theory of spinodal decomposition.

5.2 The high solute alloy

The hardness of the HS-alloy during NA is observed to increase very rapidly in early stages before it gradually becomes more or less proportional with the logarithm of time. Since the hardness increase is caused by a clustering of solute elements, the changes in slope of the hardness plot suggest that clustering happens much more rapid at short NA times than at long, or that different kind of clusters are formed. By combining the plot in figure 4.1 with the one in figure 4.2, the plot shown at the bottom of figure 5.2 is obtained, where the rapid regime can be seen to end after

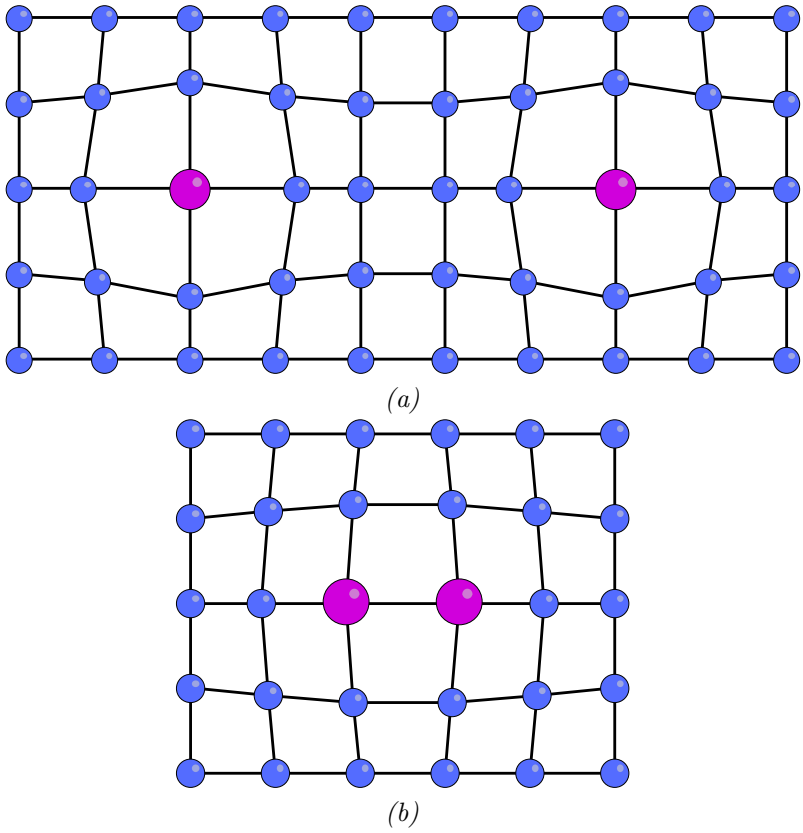

Figure 5.1: A schematic illustration of how magnesium expands the surrounding Al-matrix. In (a) two magnesium atoms are isolated from each other, while in (b) they are allowed to cluster. In (a) both atoms have to withstand the pressure from the surrounding matrix on their own, while in (b) the two atoms co-operate in order to withstand the strain.

about 10 hours of NA. This result is in agreement with results obtained by Banhart et. al [6] who discovered a similar hardness evolution in an alloy with similar Mg+Si content.

The final strength of the alloy after NA+AA is observed to cause a decrease in hardness for short NA, an effect known as the *negative effect*. This effect is reported many times in the literature [37] and attempts to prevent this effect has been made, i.e. by Yamada et. al [38] who investigated how this effect was affected by different quenching conditions. A most interesting result, which is observed in the present work but not reported before, is that the hardness of the HS alloy is observed to increase when the NA is made very long. After 325 days of NA before subsequent AA, the hardness has almost reached the maximum hardness of 126 which is observed for NA of 18 seconds before AA.

Another interesting discovery is made when the hardness plots during NA and after subsequent AA are compared. The rapid increase in hardness during NA seems to coincide with the decrease in hardness after AA, as they both seem to experience a turning point after about 5 hours. This coincidence makes it plausible that the clusters formed during early stages of NA acts preventive against precipitation and thus results in a lower hardness after AA.

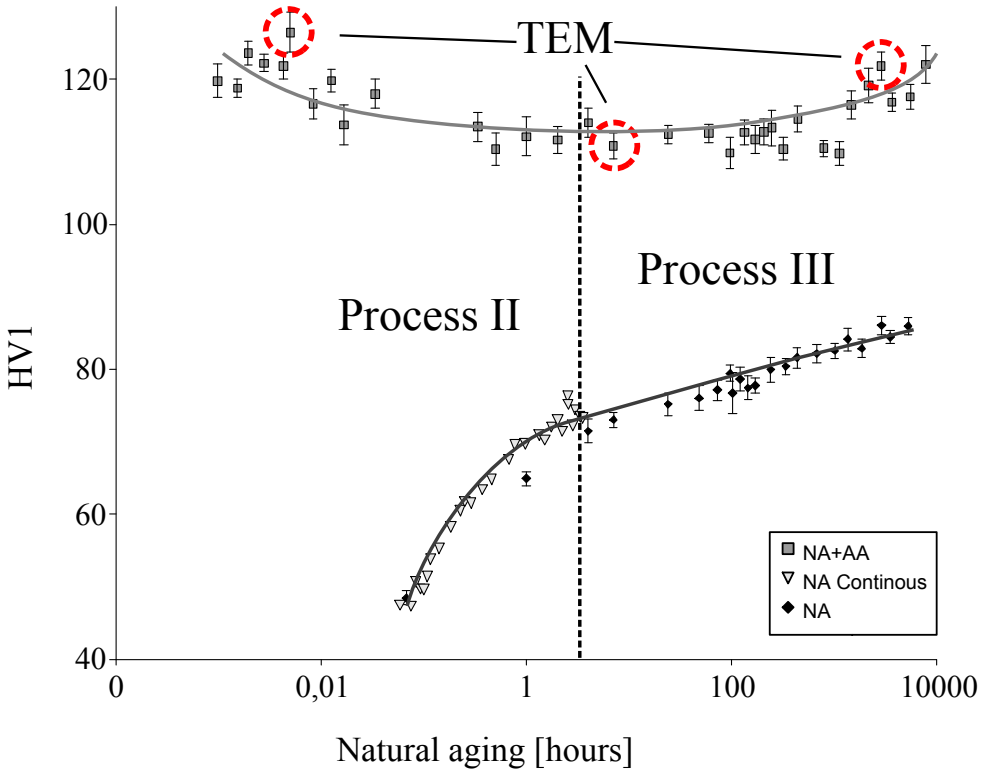

Figure 5.2: All the hardness results for the HS-alloy plotted together. The hardness increase during NA can be interpreted together with the hardness after AA to separate the process going on during NA into two parts. Process II happens at short NA times (5 hours). This causes a rapid increase in hardness during NA and a decrease in hardness after AA. Process III, which is favorable causes a steady increase in hardness both before and after AA. The labeling of the two processes as II and III will get clear during the discussion of the two other alloys.

To justify these hardness results, a microstructural analysis was made on the three samples marked with red rings in figure 5.2. The results can mainly be summarized by the so-called coarseness of the precipitates which is a combination of their

size and number density[1]. For the shortest NA investigated, the alloy is observed to have a very fine precipitate structure with many short and thin precipitates. The coarseness then increases markedly as the NA is increased, before it gets finer for even pronounced NA. This is in agreement with the result obtained by Chang et. al. [39] who reported that a finer microstructure results in a higher hardness compared to a coarser. Especially is the number density of precipitates of interest, as it decreases by a factor close to 4 with only 7 hours of NA before it again doubles for 119 more days of NA.

In addition to variations in coarsening, the volume fraction of precipitates are observed to increase with very long NA, but are equal for the two samples with the shortest NA. This is interesting because equal amount of solute are in precipitates for the two samples with the shortest NA, but their hardness differs by more than 15 Vickers. As no difference in precipitate types were found, the only difference between the two are the size and number density of the precipitates.

By combining the results obtained for the HS-alloy, it is observed that two processes take place during NA in this alloy. Why the labeling starts with process II, rather than I, will get clear during the discussion of the two other alloys.

Process II: Approximately lasts between 0 and 5 hours of NA, causing a rapid increase in hardness before AA and a decrease in hardness after AA. It also causes the microstructure to greatly coarsen as the number density of precipitates are reduced by a factor $\approx$4.

Process IIII: Approximately begins after 5 hours and lasts throughout the residual NA. The process causes a slow and steady increase in hardness during NA and also an increase in hardness after consecutive AA. It causes a reduction of the microstructural coarseness as the number density is observed to double after 119 days of NA compared to that observed after 7 hours of NA.

[1]An alloy is defined to have a coarse microstructure if it has few large precipitates. If it has many small precipitates, the microstructure is referred to as fine.

5.3 The medium solute alloy

The hardness evolution of the MS-alloy during NA can be seen in the previous chapter to be tripartite. The alloy experiences a weak hardness increase during short NA aging before it suddenly begins a rapid [2] increase after about 30 minutes of NA. This rapid increase continuous until about 10 hours of NA where it stops, and the hardness experiences a minor increase for the remaining investigated time interval. The split up behavior of the clustering at short times for this alloy strengthens the earlier mentioned idea that different clusters are created during NA.

The hardness after AA shows a peculiar dependency on NA as the hardness is observed to increase for short NA, then decrease, and finally flatten out for long NA. By comparing the hardness during NA and after AA (figure 5.3), one observes that the decrease in hardness after AA coincides very well with the rapid increase during NA. Both begin and end at the same NA-values. The clustering process which causes the rapid increase in hardness before AA are thus suspected to cause the negative effect after AA.

By combining the results obtained for the MS-alloy, it is observed that three processes takes place during NA in this alloy.

Process I: Approximately lasts between 0 and 30 minutes of NA, causing an increase in hardness both before and after AA.

Process II: Lasts between approximately 30 minutes and 10 hours of NA, causing a rapid increase in hardness before AA and a decrease after AA.

Process III: Begins after approximately 10 hours and lasts for the remaining NA. The process causes a minor increase in hardness before AA, but has no effect on the hardness after AA.

[2] With a logarithmic time scale the term "rapid" is a bit misleading because the kinetics actually are decreasing. However, the term rapid will be used when the exponential dependency of time are higher than the average.

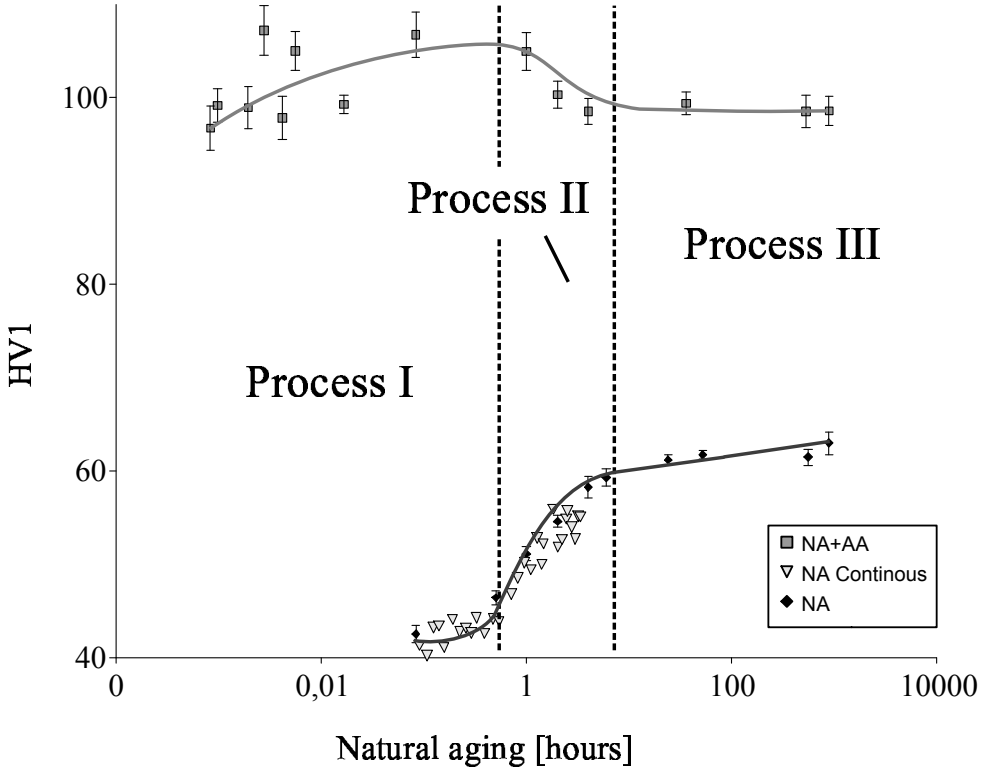

Figure 5.3: The hardness results for the MS-alloy plotted together. The hardness during NA and after AA can be interpreted to divide the process which happens during NA into three. The first process causes an increase in hardness both before and after AA, the second causes a rapid increase before AA, but a decrease after, while the third are observed to cause an increase before AA and no change after.

5.4 The low solute alloy

The combined hardness evolution for the LS-alloy during NA can be seen in figure 5.4 and can be used to observe a transition in the hardness gradient between being zero to getting non-zero after a few hours of NA. A steady increase in hardness may then be observed for the remaining of the investigated time, with only minor variations. Although the transition between a zero and non-zero hardness gradient is somewhat difficult to prove, it might suggest that different clustering processes are present in this alloy.

In figure 4.3 the low solute alloy can be observed to in general have a positive effect of NA after AA. This is the effect known in the literature as the "positive effect" of NA on 6xxx alloys and are reported e.g. by Røyset et. al [37] in 2006 and Chang et. al. [39] in 2009. The hardness after AA is seen to experience a small bump for NA around two hours, preceded by a gradual increase in hardness and succeeded by a sudden drop in hardness. Although it's difficult to prove any clear variations in hardness during NA, the bump seems to coincide with the claimed gradient variations in hardness during that time. It may anyway be suggested that the decrease after the bump is caused by the same processes which caused the negative effect in the other two alloys as well.

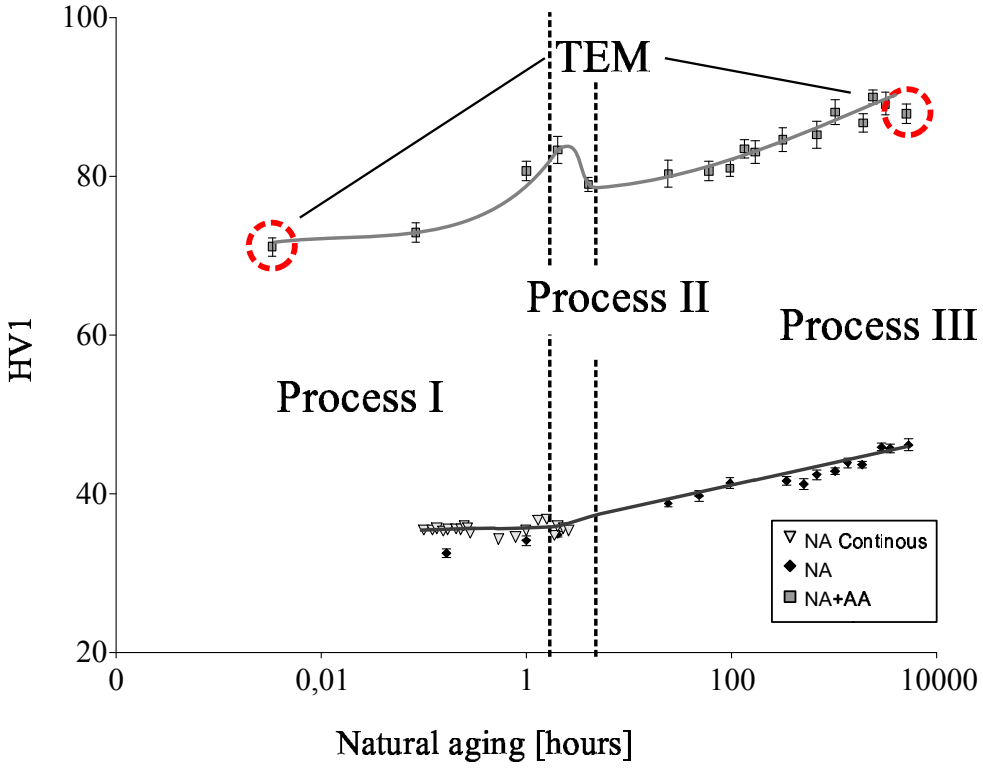

Figure 5.4: Figure showing the hardness results for the LS-alloy plotted together. The hardness before and after AA can be interpreted to divide the process which happens during NA into three. The first process causes a hardness increase both before and after AA, the second causes a hardness increase before, but a decrease after AA, while the third causes an increase in hardness both before and after AA.

Similarly to the HS-alloy, the LS-alloy was also investigated by TEM. Due to smaller variations in the hardness curve, only the two samples marked with red rings in figure 5.4 were selected. The result in figure 4.6 shows a decrease in the coarsening, but a constant volume fraction of precipitates for increased NA before AA. Again in agreement with [39]. However, none of the TEM samples are from the area around the bump found in the hardness plot after AA, so that no further information can be obtained about this phenomena.

As no difference in precipitate types were found between the two conditions, the clustering process during NA are proved to have no effect on type of precipitates formed during AA for this alloy.

By combining the results obtained for the LS-alloy, it is observed that three processes take place during NA in this alloy. The three processes can be suggested as follows:

Process I: Approximately lasts between 0 and 2 hours of NA, causing a steady increase in hardness both before and after AA. The process results in a very coarse microstructure[3] with very few and very large precipitates.

Process II: Starts after approximately 2 hours of NA and lasts up to about 5 hours of NA. The process causes a minor increase in the hardness gradient before AA and a decrease in hardness after AA.

Process III: Begins after approximately 5 hours of NA and lasts for the remaining NA. The process causes a steady increase in hardness both before and after AA.

[3]A purely relative statement, based on comparison with the results obtained on the HS-alloy and the other sample from the LS-alloy.

5.5 Alloy-comparison

By comparing the above discussion for the three alloys, a striking resemblance is observed. The different processes observed for the three alloys can be combined, and results in a total of three processes believed to be common for all alloys in the 6xxx-series. All three processes are observed to be shifted towards shorter NA for increasing solute content, explaining why only two processes are observed for the HS-alloy as the first one is assumed to have finished before the measurements began.

Process I: This process is observed for short NA depending on the alloy composition. It causes an increase in hardness both before and after AA, with its effect on microstructure being unknown.

Process II: This process starts after relatively short NA ($\sim$ seconds $\rightarrow \sim$ hours), depending on the alloy composition. The process is in any way observed to last for $\sim$ hours and is observed to cause a rapid increase in hardness during NA and a decrease in hardness after AA. This process is then believed to be what is causing the "negative effect" of NA on precipitation hardening in 6xxx-alloys. The process is observed to cause a major coarsening in microstructure, but no change in the volume fraction of precipitates.

Process III: This last process starts after $\sim$ hours of NA and continuous for all further NA times. It causes a steady increase in hardness both during NA and after AA, which seems to continue with a proportionality to the logarithm of NA-time. This process is observed to reduce the coarseness of the microstructure and to increase the volume fraction of the precipitates. By simple interpolation, the process is believed to stop when a maximum of solute elements are in precipitates, leading to an ideal structure with the predicted maximum hardness observed for the given alloy type.

The existence of multiple processes during natural aging has earlier been suggested by Banhart et. al. [6] who, through a multi-method approach, suggested that 4 processes were taking place in 6xxx alloys during NA. Banhart, however, also included vacancies in his consideration, adding another degree of freedom to the process. In any case, the numerous processes observed in the present and earlier work are clearly relating to physical clustering reactions going on in the alloys.

5.6 Clustering

The early stages of precipitation of 6xxx-alloys are a debated topic which has been studied by a wide range of techniques over the years. Already in 1972, Kovacs et. al. [55] showed through simple resistivity measurements and comparison with available data on Al-Si alloys that the precipitation in the 6xxx alloys had to begin with Si-Si clustering aided by quenched-in vacancies. This suggestion was in 1990 supported by Dutta and Allen [56] who through differential scanning calorimetry (DSC)-studies concluded upon the formation of Si-Si clusters in the early stages of NA. Later, in 1994, Edwards et. al. [57] showed through DSC-studies that two processes happened in this early stage of NA, and by APFIM, they found evidence that these two processes are the formation of Mg and Si-clusters. More studies have later been performed in the field, reporting findings of two cluster types. This includes atom probe studies by Esmaeili et. al. [58][59] and by Esmaeili and Lloyd [60] who observed similar effects to be present in AlMgSi alloys also including a slight copper addition.

In addition to the separate Mg-Mg and Si-Si clusters, Murayama et. al [61] and Murayama and Hono [30] showed through three dimensional atom probe studies (3DAP) and Gupta et. al [62] through DSC-studies that Mg+Si co-clusters were indeed forming upon long NA storage times. This has later been verified by 3DAP studies by De Geuser et. al. [40] in 2006 and Torsæter et. al. [8] in 2010 where all three kinds of clusters were observed in both studies. De Geuser et. al performed their study on a Si-rich alloy where they discovered that the Mg-Mg clusters tended to dissolve during RT-storage of more than one week. All the previous mentioned studies strongly suggest the existence of three kinds of clusters, Si-Si clusters, Mg-Mg clusters and co-clusters. The direct effect of the different clusters are still unknown, but Si+Mg clusters are repeatedly mentioned to act as nucleation sites for precipitates [38][41][42]. A combined DSC and positron annihilation (PAL)-study made by Banhart et. al [63] in 2011 shows that it is an early clustering effect is causing the negative hardness response after AA. This adds one more piece to the puzzle, but still doesn't explain the reason for the negative effect.

To summarize the above mentioned studies, they all seem to be in agreement regarding the sequence of the clustering during NA. The sequence starts with the formation of Si-Si-clusters due to their high diffusivity and is further followed up by Mg-Mg clustering. Upon prolonged NA storage, clusters of Mg and Si starts forming and this eventually leads to the transformation of the mono-clusters as these becomes co-clusters. This may be postulated due to the fact that very few mono-clusters were discovered in the study of Torsæter et. al. [8] for very long NA. The above information may finally be combined with the results from the present work as well as earlier work by the author [9] to generate a sequence of events and their effects, appearing with prolonged NA.

Process I: The formation of Si-Si-clusters: Resulting in a weak increase in hardness during NA, but leading to a strong increase in hardness after AA. The event is not connected to any energy barrier, and hence happens spontaneously.

Process II: The formation of Mg-Mg-clusters: Resulting in a rapid increase in hardness during NA, but leading to a *negative effect* after AA. The event is not connected to any energy barrier, and hence happens spontaneously.

Process III: The formation of Mg+Si-clusters and the transformation of mono-clusters into co-clusters: Resulting in a hardness increase both during NA and after AA. The hardness increase is either caused by a positive effect from the Mg+Si-clusters, a reduction of the negative effect from the Mg-Mg-clusters or a combination of both.

This last result causes the precipitation sequence (2.14) to change, resulting in a new sequence:

$$\begin{aligned} &\text{SSSS} \rightarrow \text{Si-clusters} \rightarrow \text{Si-clusters}, \text{Mg-clusters} \rightarrow (\text{Si-clusters}), (\text{Mg-clusters}), \\ &\text{Mg-Si-clusters} \rightarrow \text{GP zones} \rightarrow \beta'' \rightarrow \beta', U_1, U_2, \text{B}' \rightarrow \beta/\text{Si} \end{aligned} \tag{5.1}$$

Mono-clusters are in brackets in the fourth term since they gradually transforms into co-clusters.

5.7 Explanation for the negative effect

The *negative effect* of NA aging on AlMgSi-alloys has in the previous section been established to be caused by the formation of Mg-Mg-clusters. To find an explanation

for why this is so, the diffusion model described in section 5.1 is considered. The model shows that it is energetically favorable for one magnesium atom to diffuse towards another in order to reduce the overall stress they cause on the matrix. No energy barrier is connected with this formation, and hence the process happens spontaneously. The same happens for Si-Si-clusters, only that these are quicker diffusers and thus cluster before Mg. According to the theory, the clustering of these mono-clusters then continue until the super saturation-induced driving force for aggregation is lowered, and hence silicon-rich and magnesium-rich zones are formed in the matrix. With the clustering relying on diffusion in the solid state, this process has to be rather slow as is also observed from the hardness evolution plots in the previous chapter[4].

As the mono-clustering continues, formation of co-clusters will eventually happen (see section 5.6). This will not happen spontaneously, as for the mono-clustering, since their creation is connected with a barrier. The barrier is present due to the fact that Mg and Si expand and contract the matrix respectively, and a diffusion of these two towards each other thus will be unwanted since both elements have to cross a barrier and enter regions of the matrix that are opposite of what they prefer. However, when this barrier gets surmounted depending on attempts, as for quantum mechanical tunneling, more stable co-clusters will form with the same barrier acting against the dissolution of the clusters. In time, the co-clusters will surpass the mono clusters as the latter will transform into a more mixed cluster. A turning point will therefore arise where the size/number of magnesium-rich areas reach a maximum. This is the point where the maximum negative effect is obtained.

Imagine a situation where a lot of Mg-rich areas are present in the matrix at the point when the sample is subjected to artificial aging. For precipitates to form, a combination of Mg and Si atoms is required, and hence Si has to diffuse towards the Mg-rich zone in order to create a precipitate here. As described earlier, however, the zone will repel Si, making it difficult for precipitates to form within the zone. If many of these zones are present, a coarseness will be observed in the microstructure, since the Mg-rich zones will hinder both growth of already existing precipitates and creation of new ones. The growth of new precipitates will be restricted to areas between Si-rich and Mg-rich zones, with the Si-rich being more hospitable due to their higher diffusivity. This reduction in area where the precipitates can grow will cause the precipitates that grow in the few allowed zones to be a lot larger than normal as the solute has fewer original precipitates to go into.

The Si-rich zones can actually not be restrictive against precipitation as the exact opposite is observed. The explanation of their positive effect then has to be

[4]By slow, one means not instant.

based on their higher diffusivity rate which somehow has to enhance precipitation. Perhaps the diffusivity causes the boundaries of this enriched zone to be so fluctuating at high temperatures, that these act as good nucleation sites for further precipitation during AA. By being fluctuating, they increase the chance of the dissolution of the zone itself and also the chance for the acceptance of a Mg atom.

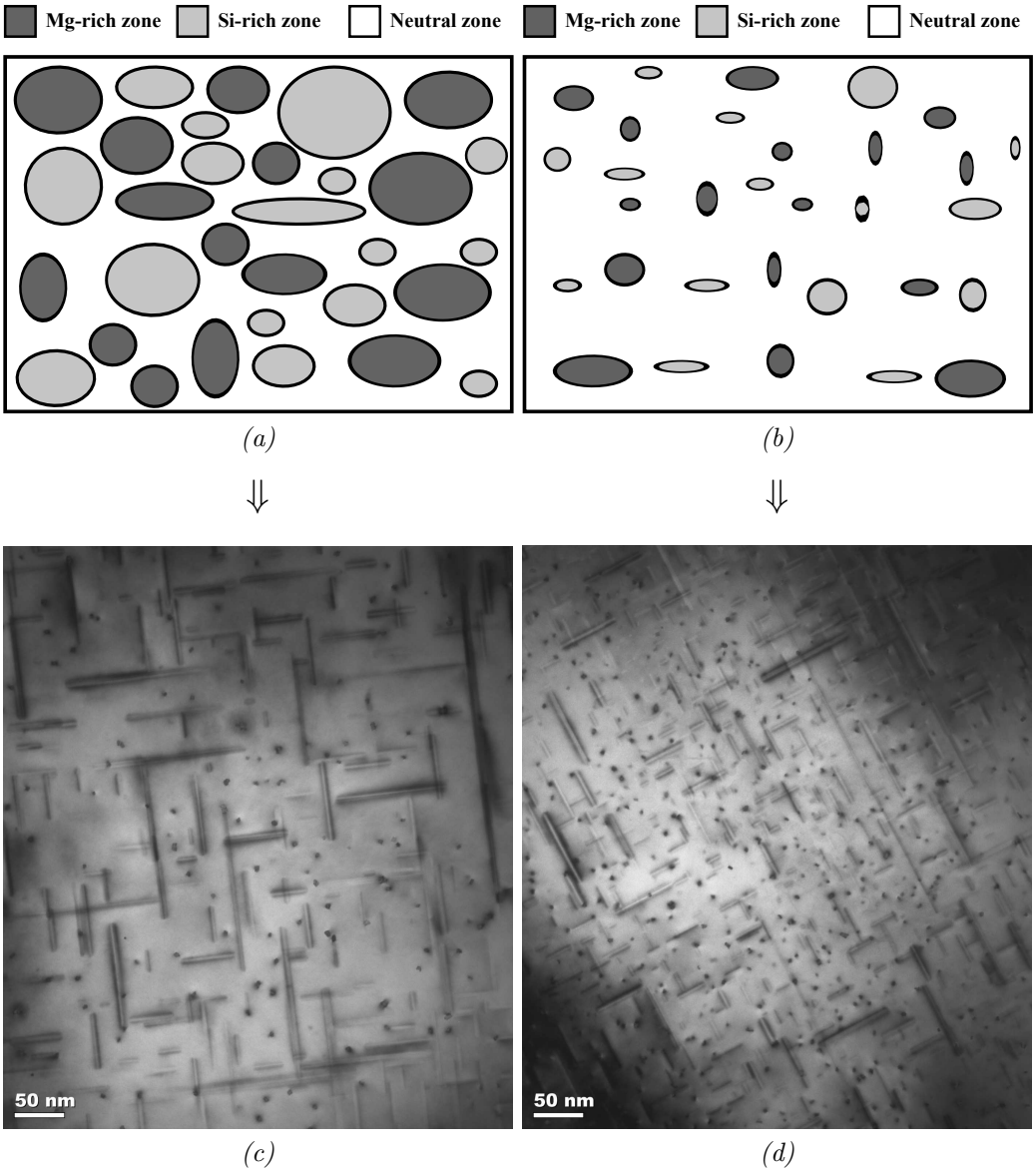

Figure 5.5: Schematic drawing of the cause for the negative effect. The formation of the Mg-rich zones (a) causes inhospitable areas for precipitation to happen. Insted the precipitates are restricted to grow in the Si-rich zones and in the in-between zones, causing a coarseness of the microstructure (c), and a lower hardness value. In the case of (a), the Mg-rich zones have not yet grown large and will not cause a coarsening of the microstructure (d).

5.8 Error discussion

5.8.1 Hardness measurements

The error bars in the hardness plots in section 4.1 result form the fact that the measurements are performed in series of ten. Although this estimate includes errors like reading errors, roughness errors, inhomogeneity errors and other single measurement errors, they don't include sources of errors causing a systematic error throughout the measurement series. Such systematic errors may be caused by in-optimal calibration, different degrees of work hardening, temperature differences etc. The errors might be constant for a given measurement series, but not constant for different series, and this may contribute to additional uncertainties. The guideline is therefore that one can not interpret all the small fluctuations in the hardness plots, but one is restricted to consider only the major trends.

In the following, two major sources of error are discussed, and a procedure of making them as small as possible is described.

5.8.1.1 Inhomogeneous surfaces due to recrystallization

Due to the fact that the alloys investigated in this experiment are created by extrusion, they experience a so-called recrystallization effect [18]. Without going into details on this subject it is stated that this effect may cause inhomogeneous surfaces in terms of variations in the grain sizes at the surface. When performing hardness measurements on such surfaces, the hardness will be strongly dependent on where on the surface the measurement is performed. Anything affecting the hardness not caused by clustering or precipitates, is strongly unwanted and hence need to be removed. Especially since this effect is inhomogeneous it prevents the hardness measurements from being comparable. A solution to the problem is found by exploiting the fact that this inhomogeneous surface layer has a thickness of maximum 100 μm [18]. The layer can therefore easily be removed by grinding the samples very well before they are measured for hardness.

5.8.1.2 Work hardening

Work hardening is the hardening effect on a material due to the material being deformed. For example if your bend you ski pole by accident, it will most likely break when you try to bend it back. The reason why it breaks when it's bended back instead of when it was bended the first time, is because the work hardening made it more brittle [2].

When a material is being cold worked [5], a great amount of dislocations are introduced into it. An increased number of dislocations in a metal will enhance the strength of it due to the ability of the dislocations to resist propagation of other dislocations (slip). In other words: if the density of dislocations becomes too large, the slip motions of the dislocations begin to interfere. This results in the material getting hardened. The dislocations may, however, be removed by annealing (=SHT) it such that the material regains its former properties.

Work hardening may occur with any form of cold working eg. bending, stretching and grinding. It is the latter which is relevant in the present work. If samples investigated in this experiment are ground after being solution heat treated, they are affected by work hardening. The purpose of the experiment is to study the effect for which the clustering affects the hardness of the material, and hence a varying hardness increase due to work hardening is strongly unwanted. However, this problem may be overcome by preparing every sample which is to be compared the exact same way. This way the same amount of work hardening is performed on each sample, and the variation in hardness of the samples relative to each other may be coupled with the clustering effects or precipitation.

5.8.2 The TEM-investigations

In the TEM-results presented in table 4.1, table 4.1 and figure 4.6, every datapoint is obtained through investigation of ten different TEM-images taken with the same magnification. The respective quantities are found for each image and the presented value is given as the mean of the values obtained for the ten images. This approach should achieve an acceptable sampling as the pictures are taken at various locations on the specimen with between 100 and several thousand precipitates measured for

[5]Cold working = altering the shape or size of a metal by plastic deformation.

each datapoint. With corrections for tilt and thickness taken into account, the accuracy of the measurements are further improved, even though certain assumptions included in these corrections makes them somewhat inaccurate.

The error of the measured quantities are only calculated from the mean values of each picture, with local variations not included in the final results. This may cause a small underestimate in the given errors, but since global variations are considered larger than the local, this underestimate is assumed to be small. Errors related to the tilt of the specimen are also excluded, but these can be considered small due to a small tilt used during the investigations.

Even though all precautions are made in order to get the most accurate measurements, the total values can still not be considered representable for the alloy itself. Certain errors, including thickness variations, long-range density variations of precipitates, measurement errors, microscope induced errors, image-quality induced errors and many more, sums up to a very large error. However, as the exact values of the investigated quantities are of no interest, the only thing that matters is that the large scale errors are constant. With a very good sampling rate and all measurements done exactly the same way, the relative variations of the investigated quantities can be considered good, and the results are considered trustworthy.

Chapter 6

Conclusion

The effect of clustering during natural aging of three different Al-Mg-Si alloys with equal Mg/Si-ratios, but different Mg+Si contents have been studied through hardness measurements and transmission electron microscopy (TEM). Based on the results presented and discussed, the following conclusions may be drawn:

- Clustering during NA of Al-Mg-Si alloys is found to be dominated by three different processes. These processes may be labeled I, II and III, and appear during NA in the same order as listed below:

  Process I: The formation of Si-Si-clusters. Found to cause a positive effect on hardness during NA and after subsequent AA with unknown effect on the microstructure. The clustering is not connected to any energy barrier, except for a diffusional one, and hence happens spontaneously.

  Process II: The formation of Mg-Mg-clusters. Found to cause a major increase in hardness during NA, and a decrease in hardness after subsequent AA. The process is observed to cause a major coarsening in microstructure after AA, and is the cause for the lowering in strength of the material. The clustering is not connected to any barrier, except for a diffusional one, and hence happens spontaneously.

  Process III: The formation of Mg+Si-clusters and transformation of mono-clusters into co-clusters. Found to cause an increase in hardness both during NA and after subsequent AA. The Mg+Si-clustering is connected with an energy barrier, causing the clusters to be more stable than the mono-clusters, but making the process slower than I and II.

However, since the co-clusters are more energetically stable they will eventually become dominant over the mono-clusters as the latter will gradually transform into co-clusters. This leads to a refined alloy microstructure leading to a higher alloy hardness.

- A new precipitation sequence is suggested, adding the three above processes in an early part of the sequence. The proposed sequence is as follows

$$\begin{aligned} &\text{SSSS} \rightarrow \text{Si-clusters} \rightarrow \text{Si-clusters, Mg-clusters} \rightarrow \text{(Si-clusters),} \\ &\text{(Mg-clusters), Mg-Si-clusters} \rightarrow \text{GP zones} \rightarrow \beta'' \rightarrow \beta', U_1, U_2, \text{B}' \rightarrow \beta/\text{Si} \end{aligned} \tag{6.1}$$

  where the mono-clusters are in brackets in the fourth term, denoting their gradual transformation into co-clusters.

- A possible explanation are suggested for why Mg-Mg clusters cause the negative effect on hardness after AA. With Mg and Si repelling each other, the formation of pure Mg-clusters will cause inhospitability against Si in these areas. Since precipitates in the 6xxx-system consists of both Si and Mg, these clusters will act with a detrimental force against precipitation. Pure Si-clusters are on the other hand not believed to cause a negative, but rather a positive effect on hardness after AA. This is believed to be caused by their much higher diffusion rate and ability to connect with vacancies.

- The precipitate types formed during AA are found to be independent of NA. For the investigated heat treatment of 1 hour SHT at 540°C and 36 hours at 175°C, the resulting precipitate types are dominated by β".

Chapter 7

Further Work

The main achievement in this thesis is the postulation of a clustering sequence for 6xxx alloys during NA and the effect of the different events on the alloy after subsequent AA. However, the conclusions are drawn without any direct evidence that the postulated clustering actually causes the predicted effects, but are only based on a comparison of own experimental results with events reported by others. A more direct atomistic study is thus needed which directly compares the cluster composition with macroscopic effects for one or more fixed alloys at short NA.

Theoretical investigations are also needed to further investigate the cause for the negative effect. A reasonable approach would be to first model accumulations of equal solutes in order to check if their binding energies support further additions of the same element. A positive result here is necessary in order to prove the model as a whole and has to be verified before further studies are to be made. More detailed studies can then eventually be performed to further check the postulation that Mg-rich zones actually repulses Si, so that no eventual error in the applied model induced the wrong conclusions.

References

[1] Pliny the Elder.
History Naturalis vol XI. 77.

[2] Donald R. Askeland and Pradeep P. Phulé.
The Scence and Enginering of Materials. Thompson, 5^{th} edition, 2006.

[3] The International Aluminum Institute.
http://world-aluminium.org/Sustainability/Environmental+Issues. November 2010.

[4] Jon Holmestad.
High-Temperature Stability of Al-Mg-Si-Cu Alloys, Master project. Tapir forlag, 2009.

[5] A. Wilm.
Physikalisch-metallurgische Untersuchungen uber magnesiumhaltige Aluminiumlegierungen. *Metallurgie*, 8:650, 1911.

[6] John Banhart, Cynthia Sin Ting Chang, Zeqin Liang, Nelia Wanderka Matthew D. H. Lay, and Anita J. Hill.
The Kinetics of Natural Ageing in 6000 Alloys - a Multi-method Approach. *Proceedings of the 12th International Conference on Aluminium Alloys, Yokohama, Japan, September 5-9*, 1:381–388, 2011.

[7] John Banhart, Cynthia Sin Ting Chang, Zeqin Liang, Nelia Wanderka Matthew D. H. Lay, and Anita J. Hill.
Natural Aging in Al-Mg-Si Alloys - A Process of Unexpected Complexity. *Advanced Engineering Materials*, 12, 2010.

[8] Malin Torsæter, Williams Lefebvre, Sigmund Andersen, Calin D. Marioara, John C. Walmsley, and Randi Holmestad.
Clustering Behaviour in Al-Mg-Si Alloys Investigated by APT. *Proceedings*

of the 12th International Conference on Aluminium Alloys, Yokohama, Japan, September 5-9, 1:1385–1390, 2010.

[9] Fredrik Aleksander Martinsen.
The Effect of Natural Ageing on Precipitation Hardening in AlMgSi-alloys. Tapir forlag, 2010.

[10] S. Venetski.
"Silver" from clay. *Metallurgist*, 13:451–453, 1969.

[11] P.B Hirsch.
Electron Microscopy of thin crystals. Butterworths, 1^{th} edition, 1965.

[12] European Aluminium Association (EAA) and MATTER.
http://aluminium.matter.org.uk. May 2010.

[13] Ruslan P. Kurta, Volodymyr N. Bugaev, and Alejandro Diaz Ortiz.
Long-Wavelength Elastic Interactions in Complex Crystals. *Physical Review Letter*, 104, 2010.

[14] CEN Comité Européen de Normalisation.
Metlliske materialer Vickers hardhetsmåling Del 1: Prøvingsmetode ISO 6507-1. 1997.

[15] New Hampshire Materials Laboratory.
http://www.nhml.com/resources/2002/7/1/hardness-testing. November 2010.

[16] T. B. Massalski.
Binary Alloy Phase Diagrams. ASM International, 2^{th} edition, 1998.

[17] B. Chalmers.
Physical Metallurgy. Cambridge University Press, 1961.

[18] D. A. Porter, K. E. Easterling, and M. Y. Sherif.
Phase Transformations in Metals and Alloys. CRC Press, 3^{th} edition, 1961.

[19] C.D Marioara, S.J Andersen, J. Jansen, and H.W Zandbergen.
The influence of temperature and storage time at RT on nucleation of the β'' phase in a 6082 Al-Mg-Si alloy. *Acta Materialia*, 51:789–796, 2003.

[20] J. W. Gibbs.
The Collected Works of J. Williard Gibbs. Longmans, Green and co., 1^{th} edition, 1928.

[21] J. W. Cahn.
On spinodal decomposition. *Acta Metallurgica*, 9:795–801, 1961.

[22] C. D. Marioara, S. J. Andersen, J. Jansen, and H. W. Zandbergen.
Atomic model for GP zones in a 6082 Al-Mg-Si system. *Acta Materialia*, 49/2:321–328, 2001.

[23] J.H. Chen, E. Costan, M.A. van Huis, Q. Xu, and H.W Zandbergen.
Atomic Pillar-Based Nanoprecipitates Strengthen AlMgSi Alloys. *Science*, 312:416–419, 2006.

[24] S.J. Andersen, H.W. Zandbergen, J. Jansen, C. Træholt, U. Tundal, and O. Reiso.
The crystal structure of the β'' phase in Al-Mg-Si alloys. *Acta Materialia*, 46:3283–3298, 1998.

[25] R. Vissers, J. Jansen M.A. van Huis, H.W. Zandbergen, C.D. Marioara, and S.J. Andersen.
The crystal structure of the β' phase in Al-Mg-Si alloys. *Acta Materialia*, 55:3815–3823, 2007.

[26] A. Frøseth, R.Høier, P.M. Derlet, S.J. Andersen, and C.D. Marioara.
Bonding in MgSi and AlMgSi compounds relevant to AlMgSi alloys. *Physical Review*, 67, 2003.

[27] S.J. Andersen, C.D. Marioara, R. Vissers, A. Frøseth, and H.W. Zandbergen.
The structural relation between precipitates in Al-Mg-Si alloys, the Al-matrix and diamond silicon, with emphasis on the trigonal phase U1-$MgAl_2Si_2$. *Materials Science and Engineering A*, 444:157–169, 2007.

[28] S.J. Andersen, C D. Marioara, A. Frøseth, R. Vissers, and H.W. Zandbergen.
Crystal structure of the orthorhombic U2-$Al_4Mg_4Si_4$ precipitate in the Al-Mg-Si alloy system and its relation to the β' and β" phases. *Materials Science and Engineering A*, 390:127–138, 2005.

[29] C. Wolverton C. Ravi.
First-principles study of crystal structure and stability of Al-Mg-Si-(Cu) precipitates. *Acta Materialia*, 52:4213–4227, 2004.

[30] M. Murayama and K. Hono.
Pre-Precipitate Clusters and Precipitation Process in Al-Mg-Si Alloys. *Acta Materiala*, 47:1537–1548, 1999.

[31] M. Takeda, F. Ohkubo, T. Shirai, and K. Fukui.
Stability of metastable phases and microstructures in the ageing process of Al-Mg-Si ternary alloys. *Journal of materials science*, 33:2385–2390, 1998.

[32] C. D. Marioara, H. Nordmark, S. J. Andersen, and R. Holmestad.
Post-β" phases and their influence on microstructure and hardness in 6xxx Al-Mg-Si alloys. *Journal of materials science*, 41:471–478, 2006.

[33] G.A.Edwards, K. Stiller, G.L Dunlop, and M.J Couper.
The Composition of Fine-Scale precipitates in Al-MgSi-Alloys. *Materials Science Forum*, 217-222:713–718, 1996.

[34] Håkon S. Hasting, Anders G. Frøseth, Sigmund J. Andersen, John C. Walmsley Rene Vissers and, Calin D. Marioara, Frédéric Danoix, Williams Lefebvre, , and Randi Holmestad.
Composition of β'' precipitates in Al-Mg-Si alloys by atom probe tomography and first principles calculations. *Journal of Applied Physics*, 106, 2009.

[35] K. Matsuda, Y. Sakaguchi, Y. Miyata, Y. Uetani, T. Sato, A. Kamio, and S Ikeno.
Precipitation sequence of various kinds of metastable phases in Al-1.0mass% Mg2Si-0.4mass% Si alloy. *Journal of materials science*, 35:179–189, 2000.

[36] M. H. Jacobs.
The structure of the metastable precipitates formed during ageing of an Al-Mg-Si alloy . *Philosophical Magazine*, 26:1–13, 1972.

[37] Jostein Røyset, Tore Stene, Jan Anders Sæter, and Oddvin Reiso.
The Effect on Intermediate Storage Temperature and Time on the Age Hardenable Response of Al-Mg-Si Alloys. *Materials Science Forum*, 519:239–244, 2006.

[38] K.Yamada, T. Sato, and A. Kamino.
Effects of Quenching Conditions on Two-Step Aging Behavior of Al-Mg-Si Alloys. *Materials Science Forum*, 669:331–337, 2000.

[39] C.S.T.Chang, I. Wieler, N. Wanderka, and J. Banhart.
Positive effect of natural pre-aging on precipitation hardening in Al-0.44 at%Mg-0.38 at% Si alloy. *Ultramicroscopy*, 109:585–592, 2009.

[40] F. De Geuser, W. Lefebvre, and D. Blavette.
3D atom probe study of solute atoms clustering during naturaal aging and pre-aging of an Al-Mg-Si alloy. *Philosophical magazine Letters*, 86:227–234, 2006.

[41] A. Serizawa, S. Hirosawa, and T. Sato.
3DAP Characterisation and Thermal Stability of Nano-scale Clusters in Al-Mg-Si Alloys. *Materials Science Forum Vols.*, 519-521:245–250, 2006.

[42] A. Serizawa, S. Hirosawa, and T. Sato.
Three-Dimensional Atom Probe Characterization of Nanoclusters Responsible for Multistep Aging Behavior of an Al-Mg-Si Alloy. *Metallurgical and materials transactions A*, 39:243–251, 2008.

[43] David B. Williams and C. Barry Carter.
Transmission Electron Microscopy Part 1: Basics. Springer, 2^{th} edition, 2009.

[44] David Brandon and Wayne D. Kaplan.
Microstructural Characterization of Materials. Wiley, 2^{th} edition, 1984.

[45] Charles Kittel.
Introduction to Solid State Physics. Wiley, 8^{th} edition, 2005.

[46] Stephen Elliot.
The Physics and Chemistry of Solids. Wiley, 1^{th} edition, 1998.

[47] David B. Williams and C. Barry Carter.
Transmission Electron Microscopy Part 2: Diffraction. Springer, 2^{th} edition, 2009.

[48] H.R Wenk, P.E Champness, J.M Cowley, A.H Heuer, G. Thomas, and N.J Tighe.
Electron Microscopy in Mineralogy. Wiley, 1^{th} edition, 1976.

[49] David B. Williams and C. Barry Carter.
Transmission Electron Microscopy Part 4: Imaging. Springer, 2^{th} edition, 2009.

[50] R. Holmestad, C.D Marioara, F. Ehlers, M. Torsæter, R. Bjørge, J. Røyset, and S.J Andersen.
Precipitation in 6xxx aluminum alloys. *Proceedings of the 12th International Conference on Aluminium Alloys, Yokohama, Japan, September 5-9*, 1:30–39, 2010.

[51] C. D. Marioara and S. J. Andersen.
Methodology for microstructure quantification in 6xxx aluminium alloys. *SINTEF materials and chemestry memo*, pages 1–6, 2009.

[52] S.J. Andersen.
Quantification of the Mg_2Si β" and β' Phases in AlMgSi Alloys by Transmission Electron Microscopy. *Metallurgical and materials transactions A*, 26:1931–1937, 1995.

[53] I. Sato, Y. Kojima, and T. Takahashi.
Modulated Structures and Gp Zones in Al-Mg Alloys. *Metallurgical Transactions A*, 13:1373–1378, 1982.

[54] S. Hirozawa, F. Nakamura, and T. Sato.
First-Principle Calculation of Interaction Energies between Solutes and/or Vacancies for predicting Atomistic Behaviors of Microalloying Elements in Aluminum Alloys. *Materials Science Forum*, 561-565:283–286, 2007.

[55] I. Kovacs, J. Lendvai, and E. Nagy.
The Mechanism of Clustering in Supersaturated Solid Solutions of Al-Mg_2Ai Alloys. *Acta Metallurgica*, 30:975–983, 1972.

[56] I. Dutta and S.M. Allen.
A clorimetric study of precipitation in comercial aluminium alloy 6061. *Journal of Materials Science Letters*, 10:323–326, 1991.

[57] G.A.Edwards, K. Stiller, and G.L Dunlop.
APFIM investigation of fine-scale precipitation in aluminium alloy 6061. *Applied Surface Science*, 76/77:219–225, 1994.

[58] S. Esmaeili, D.J Lloyd, and W.J Poole.
Effect of natural aging on the resistivity evolution during artificial aging of the aluminium alloy AA6111. *Materials Letters*, 59:575–577, 2004.

[59] S. Esmaeili, D Vaumousse, M.W. Zandbergen, W.J Poole, A Cerezo, and D.J Lloyd.
A study on early-stage decomposition in the Al-Mg-Si-Cu alloy AA6111 by electrical resistivity and three-dimensional atom probe. *Philosophical Magazine*, 87:3797–3816, 2007.

[60] Shahrzad Esmaeili and David.J Lloyd.
Effect of composition on clustering reactions in AlMgSi(Cu) alloys. *Scripta Materialia*, 50:155–158, 2004.

[61] M. Murayama, K. Hono, M. Saga, and M. Kikuchi.
Atom probe studies on early stages of precipitation in Al-Mg-Si alloys. *Materials Science and Engineering A*, 250:127–132, 1998.

[62] A.K Gupta and D.J Lloyd.
Study of Precipitation Kinetics in a Super Purity Al-0.8 Pct Mg-0.9 Pct Si Alloy Using Differential Scanning Calorimetry. *Metallurgical and Materials Transactions A*, 30:879–884, 1999.

[63] J. Banhart, M.D.H Lay, C.S.T Chang, and A.J Hill.
Kinetics of natural aging in Al-Mg-Si alloys studied by positron annihilation lifetime spectroscopy. *Physical Review B*, 83:014101, 1–13, 2011.

Appendix A

Microstructure details and TEM images

A.1 The high solute alloy

Table A.1: Table listing the microstructural details about the HS alloy sample naturally aged for 18 seconds before AA. The ten listed pictures were used to generate the data presented in section 4.2.

Picture number	Thickness (nm)	# of needles [010] #	Length needles [010] (nm)	# of needles [001] #	Length needles [001] (nm)	Area picture ($10^5 \cdot$ nm^2)	# of needle cross sections [100] #
3713	54.12	87	28.43	97	31.84	3.44	406
3715	56.07	114	30.01	102	32.76	3.41	362
3716	76.28	103	30.33	92	30.67	3.37	346
3718	59.19	121	28.33	136	26.58	3.41	517
3719	58.28	107	27.84	118	35.29	3.44	466
3720	59.17	78	26.68	110	35.21	3.39	486
3721	58.15	109	28.08	126	26.82	3.43	482
3722	58.83	86	28.92	105	28.94	3.37	511
3724	89.45	139	31.38	171	30.79	3.41	639
3728	60.58	106	26.05	133	26.74	3.41	549

Table A.2: Table listing the microstructural details about the HS alloy sample naturally aged for 7 hours before AA. The ten listed pictures were used to generate the data presented in section 4.2.

Picture number	Thickness (nm)	# of needles [010] #	Length needles [010] (nm)	# of needles [001] #	Length needles [001] (nm)	Area picture ($10^5 \cdot$ nm^2)	# of needle cross sections [100] #
3745	44.28	38	57.53	45	45.42	3.44	136
3746	36.10	51	46.73	51	53.18	3.46	135
3747	46.49	49	59.95	49	51.90	3.39	133
3748	51.27	49	48.66	58	57.32	3.44	142
3750	45.79	39	52.72	52	49.09	3.45	114
3751	48.66	62	41.08	46	62.35	3.48	159
3752	43.58	44	48.56	49	58.68	3.45	172
3753	44.33	37	46.97	56	48.58	3.49	132
3754	46.63	49	60.05	42	46.67	3.44	137
3756	78.21	65	51.75	65	58.97	3.46	207

Table A.3: Table listing the microstructural details about the HS alloy sample naturally aged for 119 days before AA. The ten listed pictures were used to generate the data presented in section 4.2.

Picture number	Thickness (nm)	# of needles [010] #	Length needles [010] (nm)	# of needles [001] #	Length needles [001] (nm)	Area picture ($10^5 \cdot$ nm^2)	# of needle cross sections [100] #
3771	42.21	78	41.59	63	37.92	3.32	266
3775	47.87	99	37.03	108	31.47	3.38	277
3777	43.01	89	37.77	103	36.59	3.41	253
3778	37.60	98	40.42	99	34.69	3.45	262
3779	45.78	79	40.21	107	35.15	3.37	285
3780	70.41	135	39.74	160	40.67	3.40	382
3781	73.35	126	42.46	146	38.9	3.39	373
3782	76.51	157	38.5	150	38.06	3.37	405
3783	49.51	99	40.16	98	38.79	3.32	259
3784	42.77	76	39.49	107	34.26	3.39	265

Table A.4: Table listing the different precipitate cross section areas observed in the HS-alloy for 18 seconds, 7 hours and 119 days of NA before AA. The thirty listed pictures were used to generate the data presented in section 4.2. The sign "-" in the table denote that the respective pictures were of too bad quality to contribute to the calculation of the mean cross sections presented in section 4.2.

18 s			7 h			119 d		
Picture number	# of CS #	CS (nm^3)	Picture number	# of CS #	CS (nm^3)	Picture number	# of CS #	CS (nm^3)
3729	42	6.59	3760	12	14.04	3791	31	8.51
3731	38	5.26	3761	9	16.41	3792	30	9.14
3733	38	6.46	3762	12	11.46	3793	18	9.86
3735	-	-	3763	9	14.08	3794	16	11.61
3736	26	7.8	3764	10	12.57	3795	26	11.38
3738	41	5.81	3765	18	11.55	3796	27	12.39
3739	24	7.97	3766	14	15.06	3797	18	11.42
3740	32	7.87	3767	8	15.30	3798	15	13.61
3741	-	-	3769	8	15.21	3799	26	10.81
3742	28	6.81	3770	13	13.86	3800	14	13.85

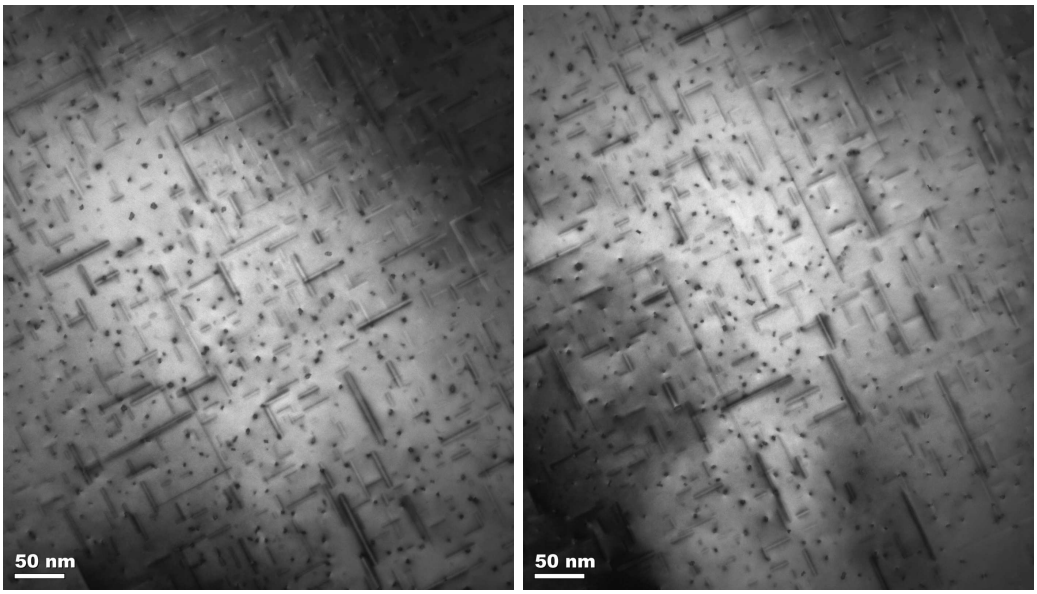

(a) *(b)*

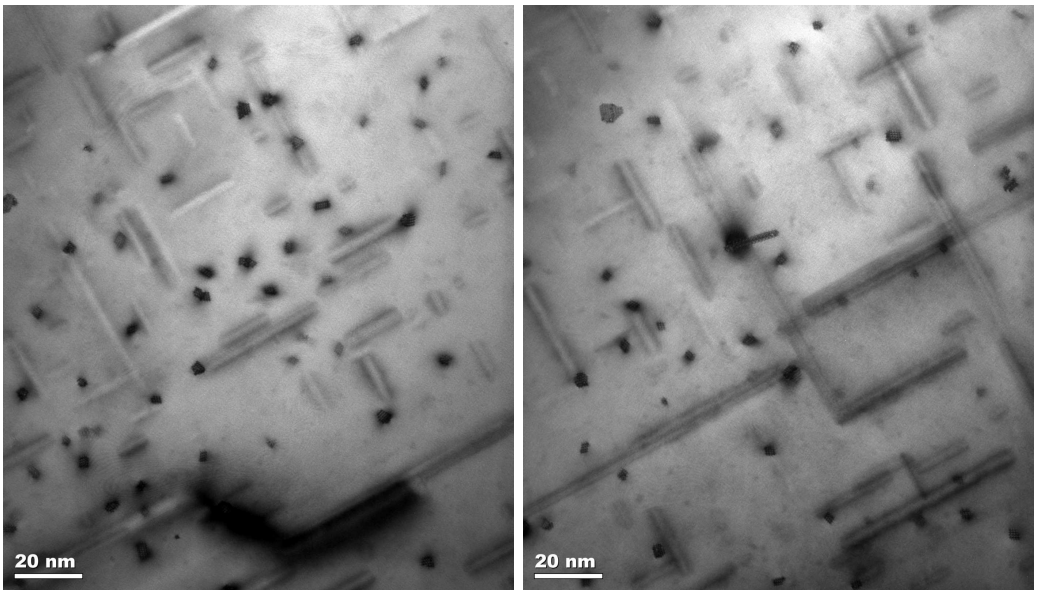

(c) *(d)*

Figure A.1: Examples of TEM-pictures taken of the HS-alloy being naturally aged 18 seconds before AA. Figure (a) and (b) are taken with low magnification, while picture (c) and (d) are taken with high magnification.

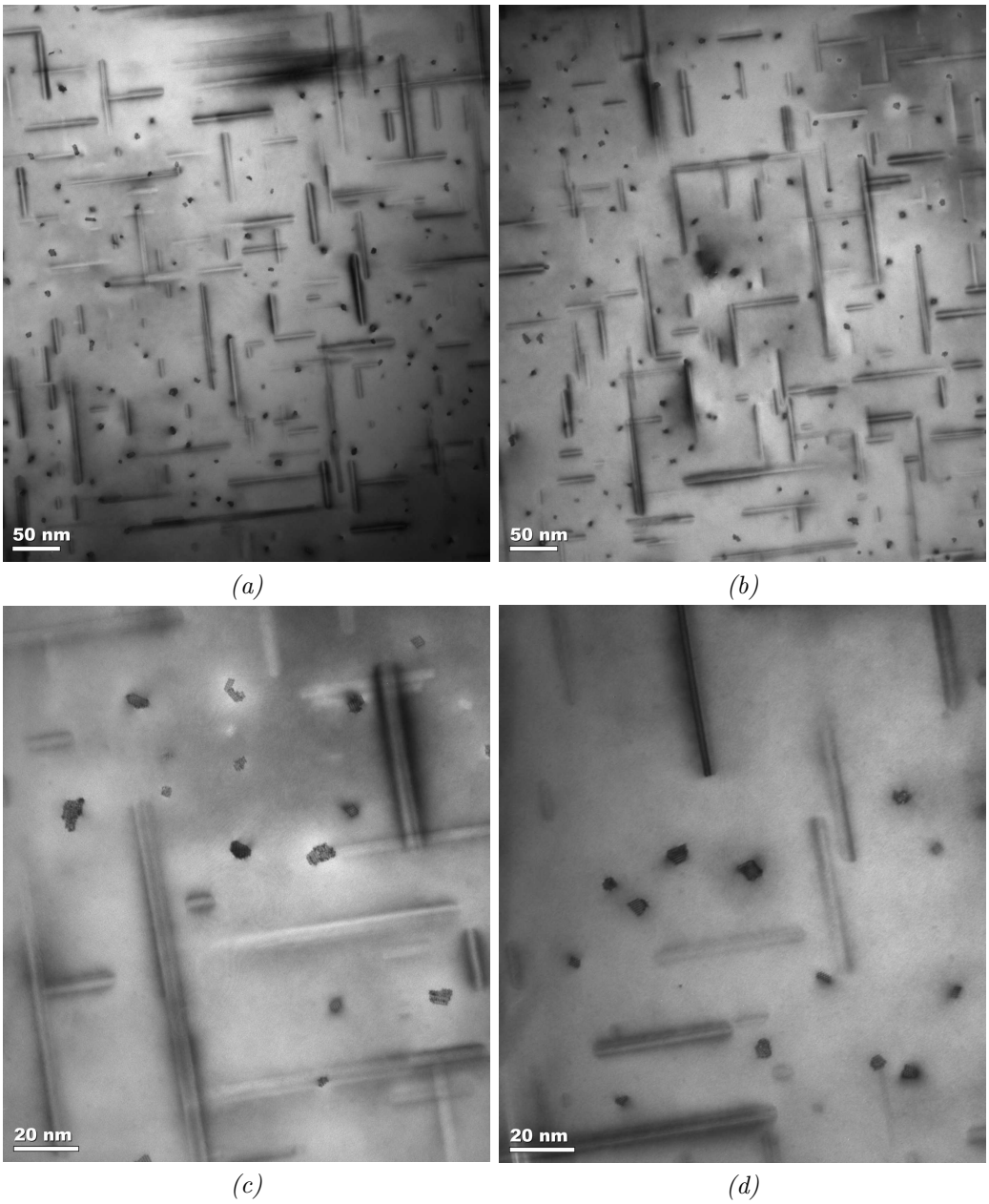

(a) *(b)*

(c) *(d)*

Figure A.2: Examples of TEM-pictures taken of the HS-alloy being naturally aged 7 hours before AA. Figure (a) and (b) are taken with low magnification, while picture (c) and (d) are taken with high magnification.

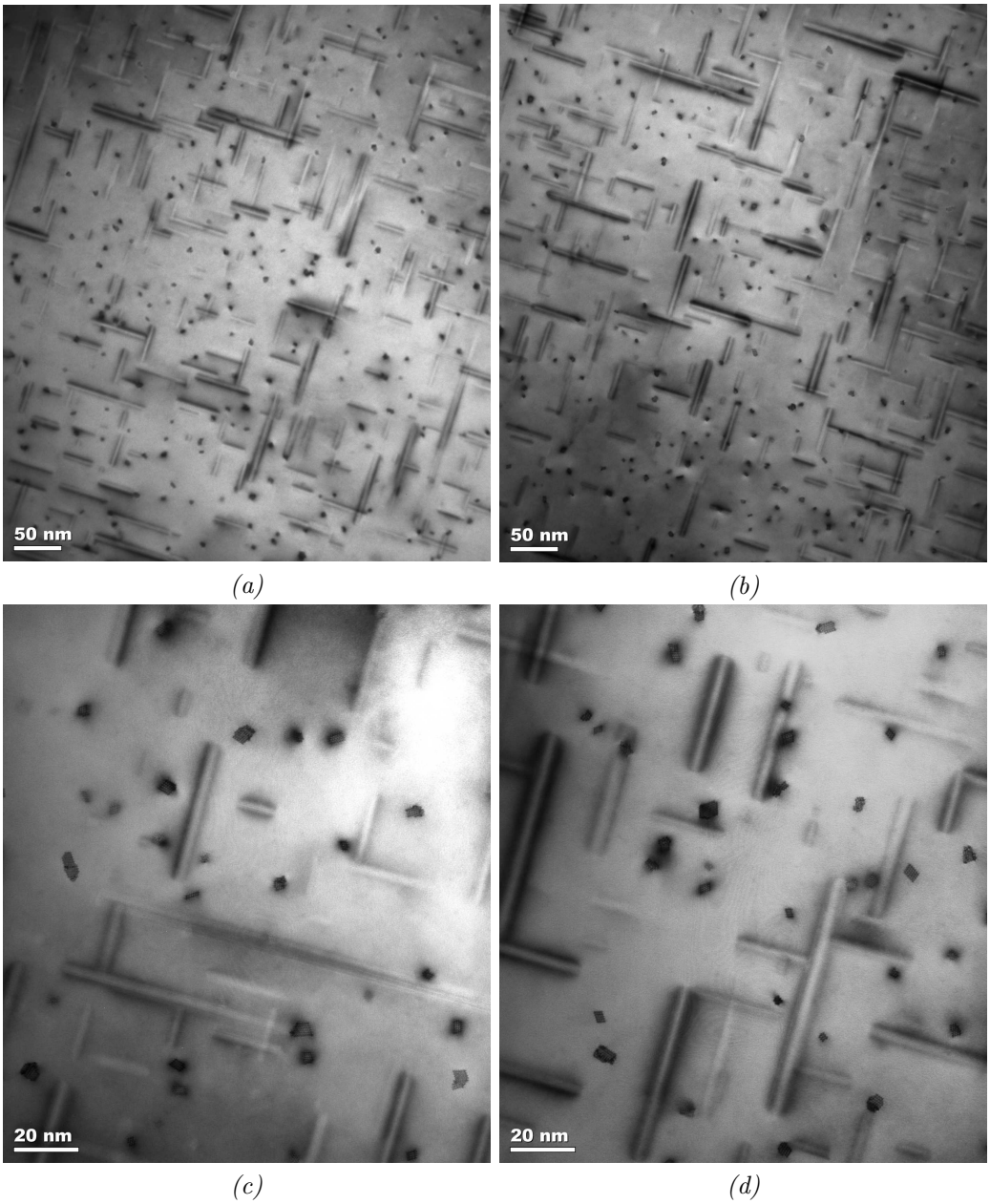

(a) *(b)*

(c) *(d)*

Figure A.3: Examples of TEM-pictures taken of the HS-alloy being naturally aged 119 days before AA. Figure (a) and (b) are taken with low magnification, while picture (c) and (d) are taken with high magnification.

A.2 The low solute alloy

Table A.5: Table listing the microstructural details about the LS alloy sample naturally aged for 12 seconds before AA. The ten listed pictures were used to generate the data presented in section 4.2.

Picture number	Thickness (nm)	# of needles [010] #	Length needles [010] (nm)	# of needles [001] #	Length needles [001] (nm)	Area picture ($10^5 \cdot$ nm^2)	# of needle cross sections [100] #
3882	76.72	40	58.62	50	35.41	3.44	71
3881	76.72	44	56.94	44	36.69	3.36	82
3883	79.25	35	46.52	31	44.73	3.35	88
3884	74.70	46	46.33	49	42.12	3.30	82
3886	71.53	43	50.42	50	36.13	3.36	96
3887	77.59	24	57.95	45	45.77	3.35	65
3888	75.59	29	53.56	36	50.18	3.36	80
3890	76.62	31	61.54	42	42.46	3.40	64
3891	78.77	37	52.81	45	36.83	3.35	90
3893	79.73	25	59.06	42	42.19	3.31	64

Table A.6: Table listing the microstructural details about the LS alloy sample naturally aged for 209 days before AA. The ten listed pictures were used to generate the data presented in section 4.2.

Picture number	Thickness (nm)	# of needles [010] #	Length needles [010] (nm)	# of needles [001] #	Length needles [001] (nm)	Area picture ($10^5 \cdot$ nm^2)	# of needle cross sections [100] #
4239	41.49	58	32.27	73	28.05	3.36	117
4240	46.66	53	30.81	47	38.04	3.35	140
4241	46.58	70	36.97	65	32.03	3.18	119
4242	46.58	69	36.06	58	33.45	3.26	125
4243	54.76	63	35.49	46	35.54	3.29	148
4244	50.04	52	39.27	54	37.04	3.23	147
4245	43.13	54	32.86	39	27.23	3.34	146
4246	35.54	44	31.88	49	39.73	3.29	94
4247	75.90	87	33.40	100	35.32	3.27	207
4248	49.78	49	46.00	42	37.94	3.29	111

Table A.7: Table listing the different precipitate cross section areas observed in the LS-alloy for 12 seconds and 209 days of NA before AA. The twenty listed pictures were used to generate the data presented in section 4.2.

18 s			7 h		
Picture number	# of CS #	CS (nm^3)	Picture number	# of CS #	CS (nm^3)
3897	7	16.09	4252	9	8.21
3898	7	20.68	4256	19	8.38
3902	4	20.21	4257	17	8.54
3903	8	14.94	4258	9	10.80
3904	6	18.23	4259	11	8.66
3905	4	22.35	4260	13	9.03
3906	7	15.39	4261	12	6.95
3908	4	25.17	4262	11	9.49
3909	8	17.41	4263	11	8.43
3910	7	16.24	4264	13	13.71

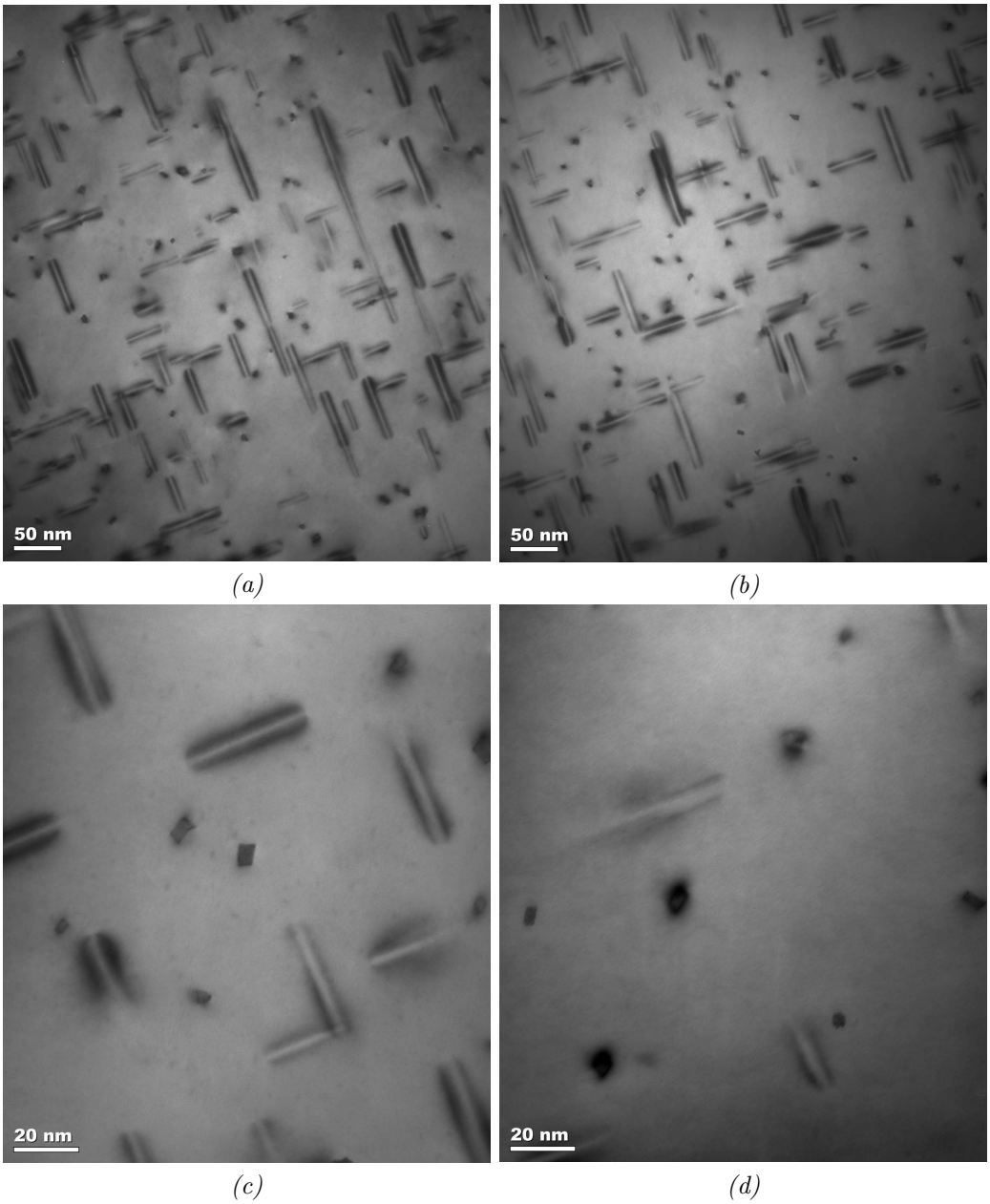

(a) *(b)*

(c) *(d)*

Figure A.4: Examples of TEM-pictures taken of the LS-alloy being naturally aged 12 seconds before AA. Figure (a) and (b) are taken with low magnification, while picture (c) and (d) are taken with high magnification.

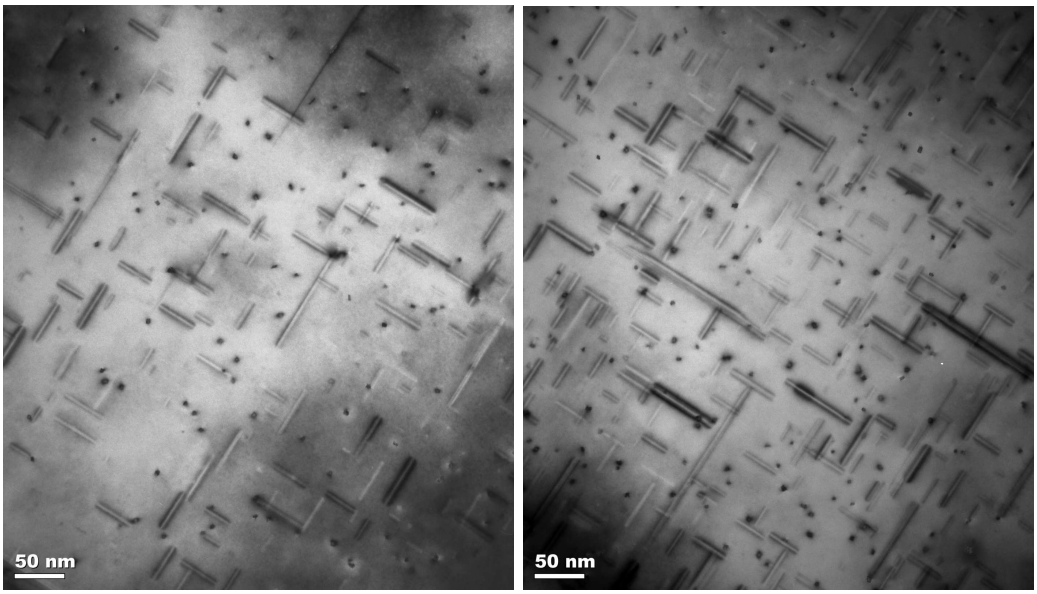

(a) *(b)*

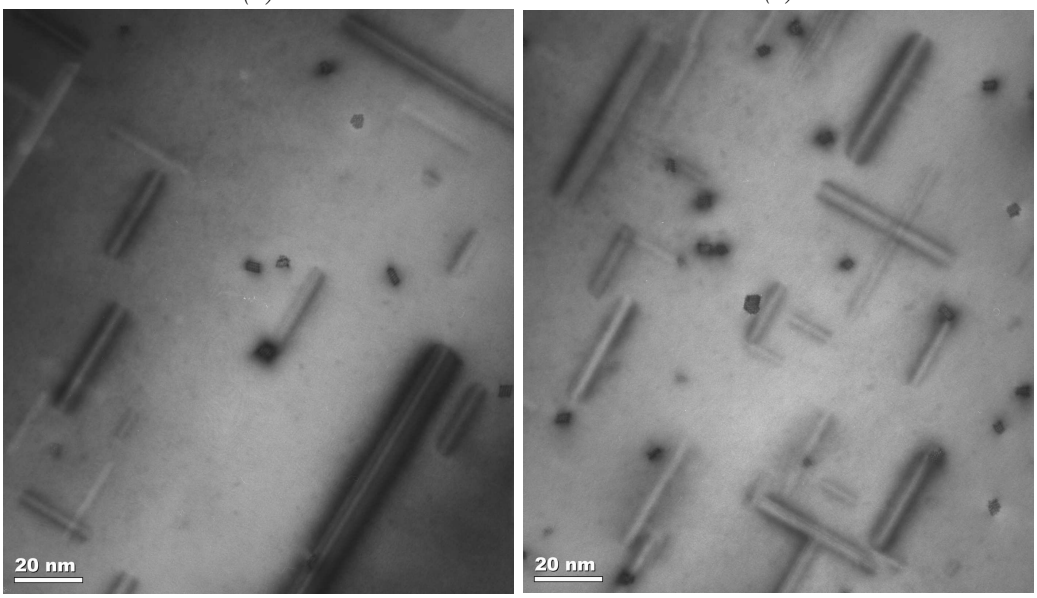

(c) *(d)*

Figure A.5: Examples of TEM-pictures taken of the LS-alloy being naturally aged 209 days before AA. Figure (a) and (b) are taken with low magnification, while picture (c) and (d) are taken with high magnification.

Appendix B

Article for submission

Draft version 09.06.11.

The Effect of Natural Aging on Precipitation in Al-Mg-Si Alloys

F.A. Martinsen [a,*], M. Torsæter [a], F.J.H Ehlers [a], R. Holmestad [a]

[a] *Department of Physics, Norwegian University of Science and Technology, N-7491 Trondheim, Norway.*

Abstract

The effect of clustering during natural aging of three different Al-Mg-Si alloys with equal Mg/Si-ratios, but different Mg+Si contents has been systematically studied in the present paper. Hardness measurements were performed both during natural aging (NA) and after artificial aging (AA) preceded by various NA times. This revealed the existence of three different clustering processes: (i) An initial process causing a slight hardness increase during NA, while a strong hardness increase during subsequent AA. (ii) A second process causing a significant hardness increase during NA while a clear decrease in hardness after subsequent AA. (iii) A third process causing a hardness increase both during NA and after NA+AA. The processes (i) and (ii) are both finished within ∼hours at room temperature, while process (iii) continues significantly longer (∼ months). Since the latter process has a positive effect on alloy hardness, it eventually leads to a reversal of the so-called negative NA effect observed for alloys of high solute content. The variations in hardness were verified by investigating selected alloy conditions by transmission electron microscopy (TEM). The results established that measures like the precipitate number density, size and volume fraction vary according to the NA+AA hardness curves. Based on comparisons with previously published results, it is suggested that reaction (i) is due to Si-Si clustering, reaction (ii) Mg-Mg clustering and reaction (iii) Mg-Si clustering.

Key words: aluminium alloys, natural aging, artificial aging, hardness measurements, transmission electron microscopy (TEM)
PACS: 81.40.Cd, 61.46.Bc, 82.80.-d

1. Introduction

Al-Mg-Si (6xxx series) alloys are frequently used for industrial purposes due to the ease in which they can be formed, welded, anodized and painted. They are medium strength materials that can be hardened through artificial aging (AA) at elevated temperatures (150°C-200°C), leading to the formation of precipitate particles that impede dislocation motion. Since a large energetical barrier needs to be overcome to form the equilibrium precipitate phase, β-Mg_2Si [1] and the pure Si particles, the process goes through a number of metastable structures [2]:

$$\begin{aligned} &\text{SSSS} \rightarrow \text{solute clusters} \rightarrow \text{GP zones} \rightarrow \beta'' \\ &\rightarrow \beta', U_1, U_2, \text{B}' \rightarrow \beta/\text{Si} \end{aligned} \tag{1}$$

Detailed information on the structurally well-developed intermediate phases, starting from GP zones, can be found elsewhere [3,4] - but the exact nature of the solute clusters is still debated [5]. These form during the early stages of AA heat treatment, but they are also reported to appear upon so-called natural aging (NA) at room temperature [6]. These NA clusters are of the utmost importance - since they affect the kinetics of precipitate formation throughout the precipitation sequence. As they impose such strong effects, and since a short period of NA is industrially unavoidable due to difficulties in relocating huge amounts of material in short times, the phenomenon requires a detailed study.

* Corresponding author. Adress: Department of Physics, Norwegian University of Science and Technology, N-7491 Trondheim, Norway. Tel.: +47 48239236.
Email address: fredrikamartinsen@gmail.com (F.A. Martinsen).

Most interestingly, it has been observed by Røyset et. al. [7] that the effect of intermediate NA before AA heat treatment varies according to the total solute content of the alloy. In alloys of Mg+Si>1wt% a *negative NA effect* was observed, while alloys of Mg+Si<1wt% displayed a *positive NA effect* on alloy hardness after AA. Microstructural studies by TEM [8] revealed that the negative NA effect was related to a lowering in number density of hardening precipitates, while APT studies of Chang et al. [9] revealed that the positive NA effect relates to a boost in precipitate formation during AA.

The negative NA effect is so-far the most well-known, as it takes place in the dense, most commonly applied Al-Mg-Si alloys. A simple way to avoid their hardness decrease, resulting from intermediate NA, would lead to huge profits for the aluminum industry. Alloys could then be strengthened at low cost - and aluminum alloys would compete more strongly against other materials in a wide range of applications. The problem is, however, that the NA effect is caused by nanoscale solute clusters that are not straight-forward to investigate. Their very small size, together with their coherent growth with the surrounding Al lattice, make them unsuitable for investigation by standard microscopic methods [10,6]. As a result, our knowledge about the NA clustering is still insufficient - even if the subject has been the topic of several studies.

The first researchers that aimed to investigate the eariest stages of phase separation in Al-Mg-Si alloys were Kovacs et al. [11] in 1972. They showed through simple resistivity measurements and comparisons with available data on Al-Si alloys that Si-Si clustering aided by quenched in vacancies was likely to be the first step of the process. This suggestion was in 1990 supported by Dutta and Allen [12] who, through differential scanning calorimetry (DSC) studies, concluded upon the formation of Si-Si clusters in the early stages of NA. Later, in 1994, Edwards et. al. [13] showed through DSC studies that two processes took place in this early stage of NA. By atom probe field ion microscopy (APFIM) they found evidence that these two processes could be connected to the formation of separate Mg and Si clusters.

With the advent of the three dimensional atom probe (3DAP), more in-depth studies of cluster sizes and compositions could finally be made [6,14]. These revealed that in addition to the separate Mg-Mg and Si-Si clusters, Mg-Si co-clusters are forming upon long NA storage times or slightly higher aging temperatures. This was later verified by 3DAP studies by De Geuser et. al. [15] in 2006 and Torsæter et. al. [16] in 2010, where all three kinds of clusters were observed in both studies.

The previously reported studies add some pieces to the puzzle, but an explanation of *why* the positive and the negative NA effects take place is still far from being found. Results obtained in different groups are difficult to compare due to the extreme sensitivity of early-stage clustering to variations in heat treatment procedure, Mg/Si ratio, Mg+Si content and possible additions of other impurity elements. Consequently, we will in this work report a comprehensive study displaying exactly how variations in NA storage time affect the alloy microstructure after AA. This is investigated both by hardness measurements and transmission electron microscopy (TEM). The study involves alloys of different solute content (high, medium, low), but the alloy Mg/Si ratio is kept fixed for all three. Our results verify many of the hypothesis made by other researchers - but a novel key observation is made: the negative NA effect is reversed upon long NA storage times. This means that resources spent in quickly transferring large amounts of aluminum from one oven to another are in vain - as hardness would be gained by just introducing a delay in the production process allowing the alloy to rest at room temperature for about two months before artificial aging heat treatment. In addition, this observation provides information allowing for a physically sound description of the NA clustering process.

2. Experimental

Three industrial Al-Mg-Si alloys with equal Mg/Si ratios, but different solute content (Mg+Si), were investigated in the present work. Their nominal compositions are given in Table 1, where they are labeled according to their level of solute: HS = high solute content, MS = medium solute content and LS = low solute content. All three alloys are seen to contain similar amounts of iron and manganese.

Table 1
Content of alloying elements in the different alloys in wt.%

Alloy type	Label	Al	Mg	Si	Fe	Mn
LS	6060	98.93	0.37	0.45	0.2	0.05
MS	6005	98.511	0.555	0.718	0.2	0.016
HS	6181	98.05	0.75	0.95	0.2	0.05

The original samples were long extrusion made billets with either circular or rectangular shape and were received from Hydro Al. Samples were made by cutting out ∼3x3 cm pieces of thickness < 3mm, and these were given a initial SHT of 540°C for one hour in a salt bath before be-

ing water quenched (WQ) to room temperature (RT). The samples were further divided into two groups, depending on whether or not they were going to be artificially aged. The first group of samples were only left for RT-storage and were regularly measured for hardness during the storage. The samples in the other group were left for various RT-storage times before they were subsequently artificially aged for 36 hours in an oil bath at 175° and then water quenched to RT. The samples were then further polished and measured for hardness. The temperatures in the oil and salt baths were measured to be within ±2° of the quoted value using a Digitron Instrumentation K-type thermocouple. The hardness measurements were carried out on a Matzuzawa-1S unit using a load of 1000 grams, 15 seconds loading time and a load speed of 100μm/second. The instrument was consistently manually calibrated each time it was being used in order to obtain comparable results. Two types of hardness measurements were made: ordinary measurements where the average over 10 indents results in a point on the hardness curve, and measurements denoted *continuous* - where the measurement value of each indent is plotted. The latter plots were made to map the very quick initial hardness changes for each alloy.

From the NA+AA hardness results, three samples from the HS alloy and two from the LS alloy were selected for investigations by TEM. Specimens were polished using a Stuers Kuth Rotor grinding device mounted with silicon carbide grinding paper, before they were electropolished using an electrolyte of one part nitric acid and two parts methanol. The electropolishing was carried out using a Stuers TenuPol-5 operated at 20 V with a light stop value of 120, a pump flow rate of 38 and with the electrolyte held between -20° and -30°C during polishing. The specimens were further investigated in a Philips CM30 TEM with a LaB_6 filament operated at 150 kV. Thickness measurements were performed using a Gatan model 601 parallel electron energy loss spectrometer (PEELS) equipped with an EL/P software. For each alloy condition, a series of ten TEM images (x 144000 magnification) were taken together with corresponding thickness measurements for the purpose of quantifying the average precipitate sizes and number densities. Pictures with x 491000 magnification were taken in order to calculate the average precipitate cross sectional areas. The reason for taking 10 images was to reduce the effects that possible inhomogeneities of precipitates would cause on the results.

3. Results

Natural aging: The hardness of the three alloys during natural aging can be seen in Figures 1a, 1c and 1e. The results extending over the whole interval of different NA times have datapoints representing the mean of ten indentations. Additional series are included for short NA times, denoted *continuous*, where one datapoint represents one indent with the hardness measurement machine.

The hardness of the HS alloy (Figure 1a) is seen to increase rapidly for short NA times before it gradually becomes proportional with the logarithm of time after about five hours. The hardness of the MS alloy (Figure 1c) is observed to increase slowly for short NA times, then increase rapidly between 30 min and 10 hours and furhter slowing down again after 10 hours. The LS alloy (1d) is observed to increase more or less proportionally with the logarithm of time during the entire investigated time interval with only a slight change in slope visible for short NA times.

Natural aging + subsequent artificial aging: The hardness variations of the three alloys as a function of NA time before the fixed AA heat treatment are shown in Figures 1b, 1d and 1f. The HS alloy (Figure 1b) is seen to decrease in hardness for NA storage times up to about five hours. For prolonged NA, the hardness is observed to increase, and this continues for all further NA times. The MS alloy (Figure 1d) is observed to increase in hardness for NA storage times up to 30 minutes. Further, the hardness decreases abruptly - before it stabilizes after about 10 hours NA. In this latter interval only a slight hardness increase is observed. The LS alloy (Figure 1f) is seen to increase in hardness with NA times up to two hours. Further, the alloy is observed to drop slightly in hardness, before it increases again upon prolonged intermediate NA times.

TEM-results: Based on the NA+AA curves (Figure 1b, 1d and 1f), three samples from the HS alloy and two from the LS alloy were selected for TEM analysis. The HS samples had been stored at RT for 18 seconds, 7 hours and 119 days before the fixed AA heat treatment, while the samples selected from the LS alloy had been naturally aged 18 seconds and 209 days before AA. It was found that all samples contained mainly the needle shaped β" phase, and only a few β' and B' precipitates were observed along grain boundaries. Representative TEM images for the LS alloy conditions are provided in Figure 2, and they show that the microstructure of the alloy becomes finer for prolonged intermediate NA times. For the HS alloy, rep-

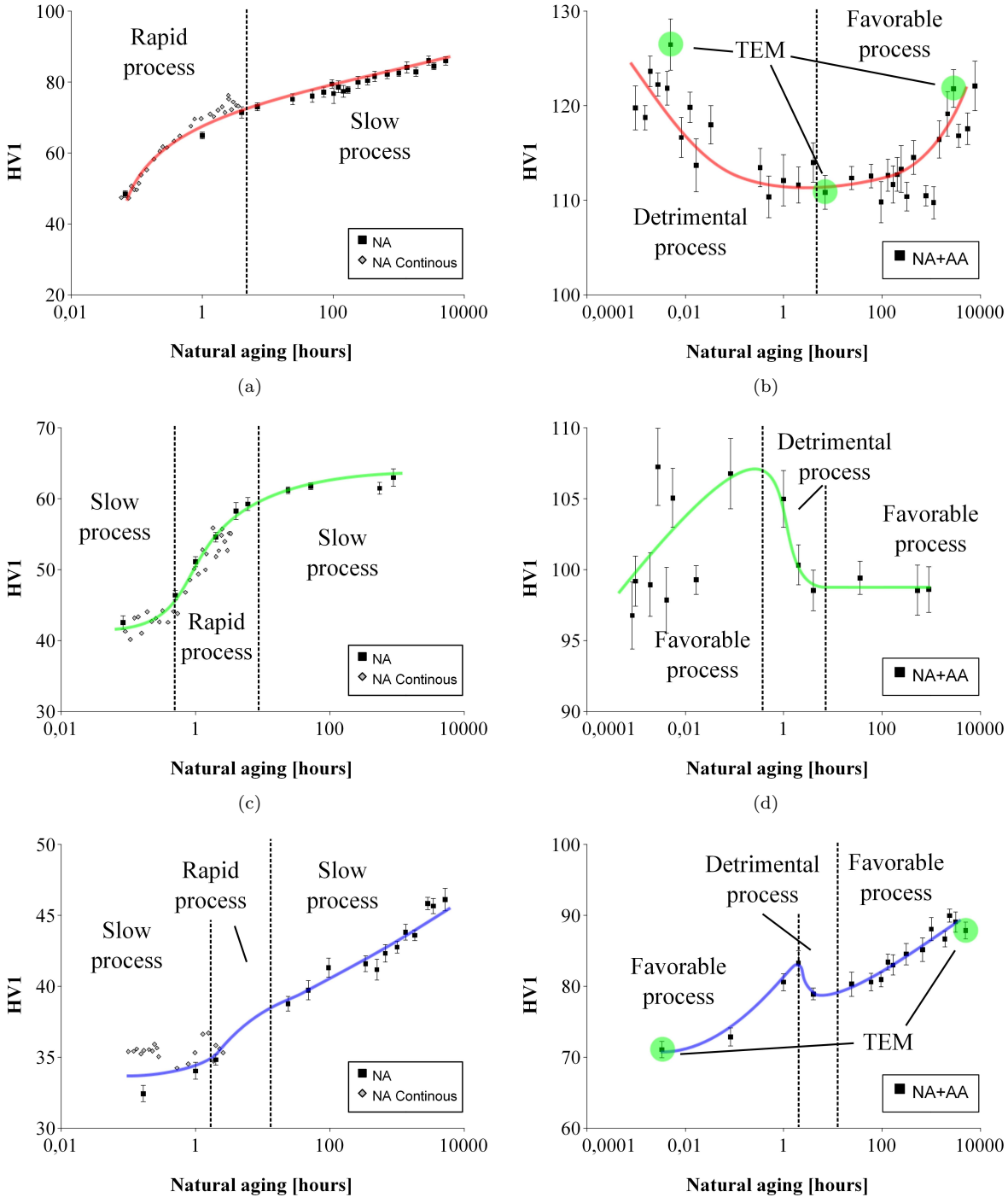

Fig. 1. The hardness results from the HS-alloys (a)-(b), MS-alloy (c)-(d) and LS alloy (e)-(f) plotted for both during NA (left) and after NA+AA (right). The colored lines are inserted as a guide for the eye, while the vertical dotted lines indicate where a change in slope of the curves are evident. These changes are seen to coincide for both NA and NA+AA hardness evolutions. This suggests that the effects appearing during NA are the ones causing the changes in the NA+AA curves. For figure (e) no evident changes are obserable, and the applied lines are drawn at equal times as in (f). The samples chosen for TEM-investigations are marked with dotted red rings.

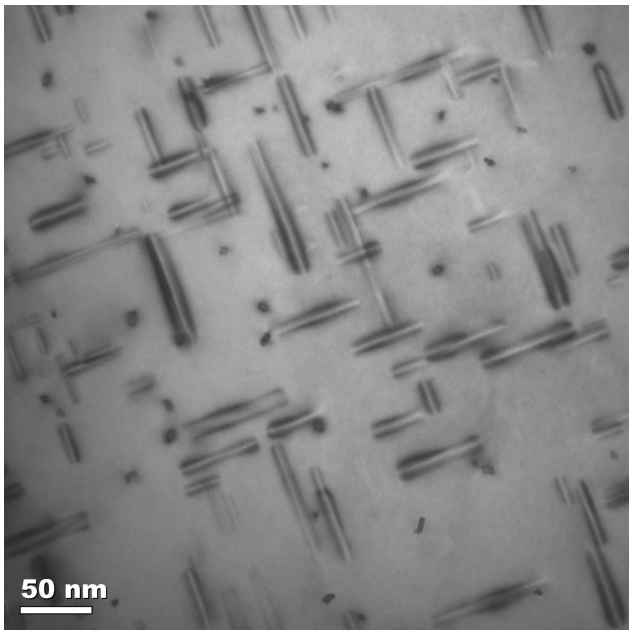

(a)

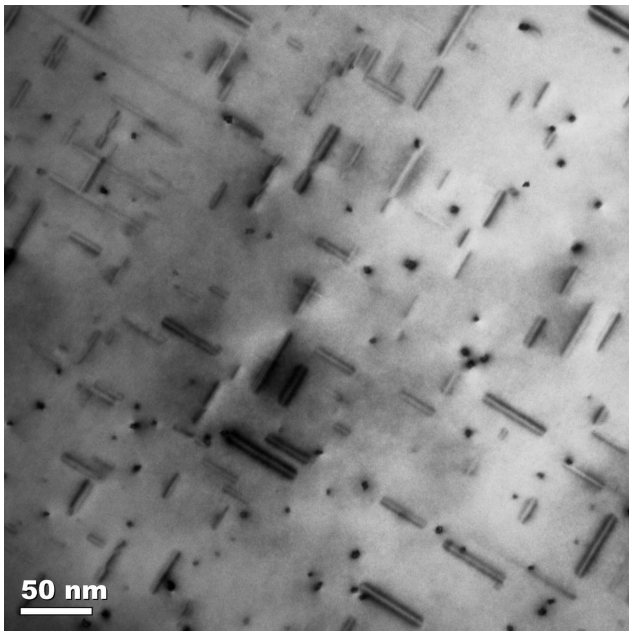

(b)

Fig. 2. TEM pictures of the LS alloy. Samples stored (a) 12 seconds and (b) 209 days at RT before AA. The sample in (a) can be observed to have a coarser microstructure than the one in (b).

resentative TEM images are given in Figure 3 - and they show that the microstructure qualitatively displays a clear *fine→coarse→fine* evolution for prolonged intermediate NA times.

A *quantification* of the microstructural details calculated based on TEM images can be seen in the plots in Figure 4. The volume fraction is here calculated by multiplying the other three quantities. As expected from qualitative observations, the precipitates of the HS alloy become larger and fewer if the sample is stored ∼hours compared to if it is stored for ∼seconds. For even longer NA storage times the precipitates in the HS alloy are observed to again become smaller and more numerous, but not as small and numerous as for the sample where NA storage was kept at a minimum. The volume fraction of precipitates for the various HS alloy conditions is seen to be almost equal for the samples stored 18 seconds and 7 hours, but it increases for the sample stored 119 days. For the LS alloy, the precipitates become smaller and more numerous for prolonged intermediate NA times - but the volume fraction is observed to be equal for the two investigated alloy conditions.

4. Discussion

4.1. *Three processes*

The hardness curves of the three alloys during NA (Figure 1a, 1c and 1e) can be directly compared with the hardness curves after NA+AA (Figure 1b, 1d and 1f). The TEM results obtained from chosen points of the latter curves (Figure 4) justify that the variations observed in the NA+AA curves actually mirror real microstructural changes in the alloys. The observation that there seems to be a correlation between the occurence of a process in both the NA and NA+AA curves justify the division of the curves into regions where different processes are believed to take place.

For the HS alloy a process is observed to happen between 0 and 5 hours of intermediate NA. This causes a rapid increase in the hardness during NA and a rapid decrease in hardness in the NA+AA curve. From TEM this process is found to lead to a coarsening of the microstructure. A second process is observed for prolonged NA times: the hardness during NA continues to increase, but the slope is less steep, and the NA+AA curve rises again. By TEM the process is found to lead to a finer microstructure.

For the MS alloy the clustering during NA can be divided into three parts: (i) A first reaction happening between 0 and 30 min of intermediate NA storage. It leads to a slight increase in hardness during NA, but causes a major increase in hardness after NA+AA. (ii) A second process happening between 30 minutes and 10 hours of intermediate NA storage. It leads to a large increase during NA, but a *de-*

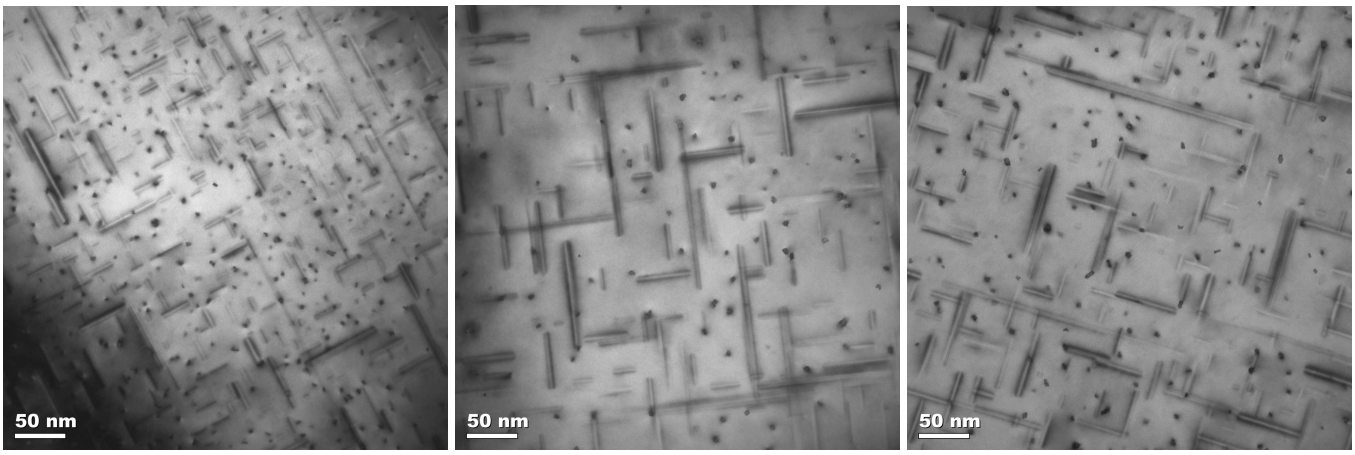

(a) (b) (c)

Fig. 3. TEM pictures of the HS alloy. Samples stored (a) 18 seconds, (b) 7 hours and (c) 119 days at RT before AA. The microstructure can be observed to follow a *Very fine→coarse→fine* pattern for prolonged intermediate NA times.

crease in the NA+AA curve. (iii) A third process observed to start after about 10 hours of intermediate NA and continue for all investigated prolonged NA times. It causes an increase in hardness during NA, but leads to a decrease in hardness for NA+AA.

For the LS alloy it is more difficult to divide the clustering processes into different parts. By interpreting the NA+AA hardness curve in the same way as for the MS alloy, however, one can explain some of the changes observed. The "bump" after 2-3 hours of intermediate NA storage can then be seen to correspond to the larger bump observed for the MS alloy. As there is much less solute in the LS alloy, the shift of the bump to longer NA storage times is as expected - since solute atoms statistically need to travel over longer distances to cluster in this alloy. The left part of the bump then indicates a fist process that lasts between 0 and 2 hours of intermediate NA, leading to no hardness increase during NA - but a visible increase in the NA+AA curve. The second process starts at the top of the bump, and ends at the bottom of it (after about 10 hours of intermediate NA). This process gives a visible hardness increase during NA and a visible *decrease* after NA+AA. Further, a thrid process takes place - starting after about 10 hours of NA and lasting throughout the investigated interval of intermediate NA storage times. It gives a hardness increase both during NA and after NA+AA.

As was acknowledged for the LS and MS curves, a striking resemblance is observed between the clustering behaviors in the various alloys. Assuming that the same "bump-interpretation" can be transferred to the HS alloy, the left part of the bump is here impossible to investigate. This is as expected, since this alloy is so packed with solute elements that statistically clustering can happen very quickly. The first measurements are thereby made at the top of the bump, meaning that the first process is already finished before measurements have started.

In summary, it is likely that three clustering processes can be distinguished for *all* Al-Mg-Si alloys: (A) Favorable process giving little hardness increase during NA, but providing an increase in hardness after NA+AA, (B) Detrimental process giving a rapid hardness increase during NA, but leading to a decrease in alloy hardness after NA+AA. (C) Favorable process giving a steady hardness increase during NA, and providing an increase in hardness after NA+AA. All three processes are observed to shift towards shorter NA times for increasing solute content, explaining why only the two last processes are observed for the HS alloy.

4.2. *A formation barrier*

Metastable phases appear earlier than the equilibrium phase in the precipitation sequence (1) because they are associated with a smaller formation barrier. This also applies to clusters, meaning that those associated with a small barrier will form before those associated with a larger one [17]. In literature it is reported that Si-Si and Mg-Mg clusters form first [14], and these are therefore likely to be associated with a lower formation barrier than the Mg-Si clusters that are reported to form later [6,18]. However, if an energy barrier needs to be surmounted to form the clusters, the same barrier must be surmounted to dissolve them. This stabilizes the clusters, and explains why only Mg-Si clus-

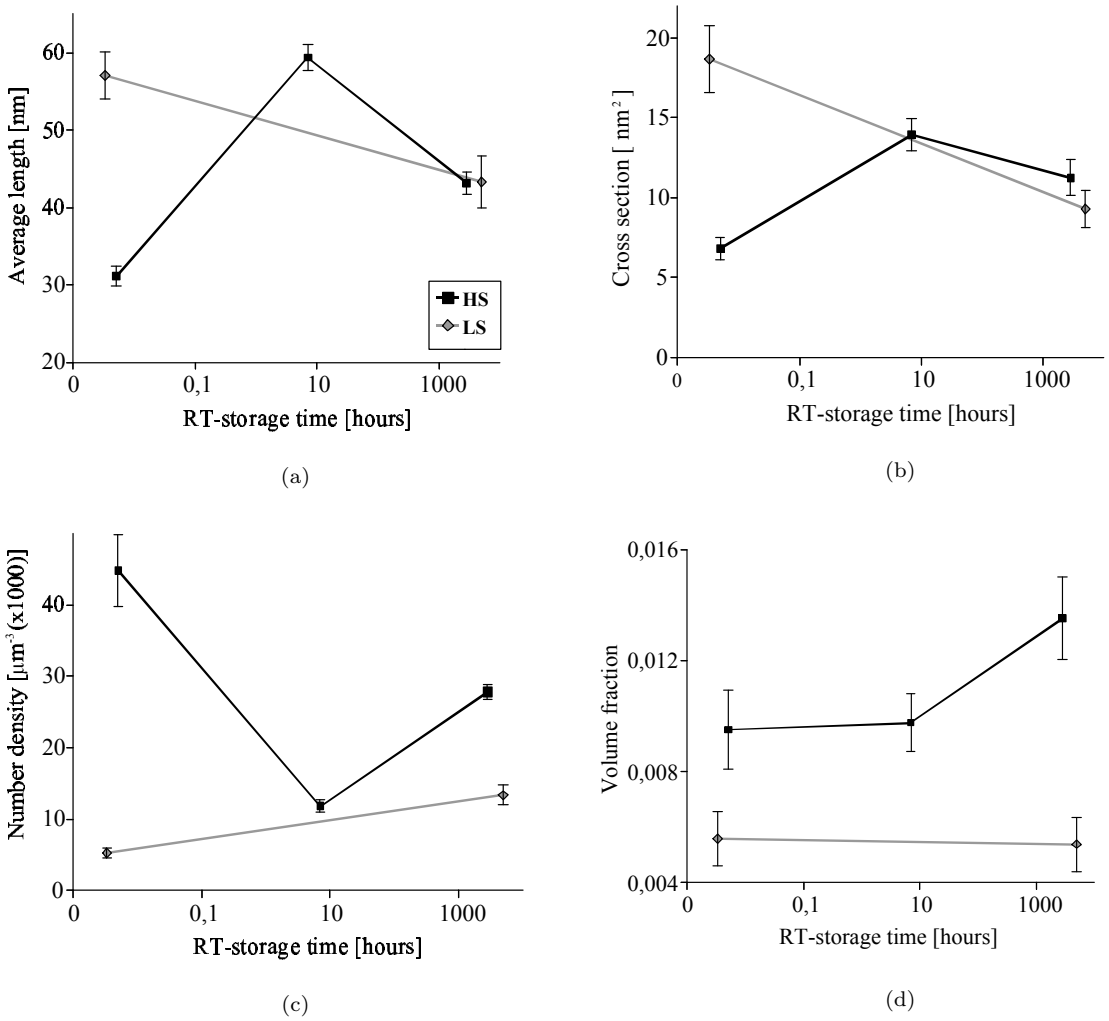

Fig. 4. An overview over the evolution in microstructure for the LS and the HS alloy as a function of NA time. (a) The variation in average precipitate length, (b) the variation in average cross section and (c) the variation in precipitate number density. The volume fraction variatioin displayed in (d) is found by multiplying the other three quantities.

ters survive heat treatment at 100°C [16]. It is also very likely that these slowly forming Mg-Si clusters enhance GP zone formation, as both structures are reported to have Mg/Si∼1 [6,16].

A recent study of Chang et al. [19] for the first time revealed three clustering peaks in DSC spectra, where the two first reactions happened very quickly - and the latter more gradually. This is in agreement with the three processes observed in our study, and by comparing to the previously reported sequence of clustering [14,15,13] it is likely that **process A** corresponds to Si-Si clustering, **process B** to Mg-Mg clustering and **process C** to Mg-Si clustering. This makes Mg-Mg clustering responsible for the detrimental effect of NA. The reversal of the negative effect can then be assumed to be related to the Mg-Si clustering. As this is slow and thereby barrier related, it forms more stable complexes - that are likely to dominate the alloy microstructure upon prolonged aging (by forcing less stable aggregations to give up solute atoms, and thereby growing on their expense). The reversal of the negative NA effect will thereby correspond to the point where the stable Mg-Si clusters outnumber their less stable competitors.

5. Conclusion

The effect of clustering during natural aging of three Al-Mg-Si alloys with equal Mg/Si-ratios, but different Mg+Si contents have been studied by hardness measurements and transmission electron microscopy (TEM). Based on the results, the following conclusions may be drawn:

- Clustering during NA of Al-Mg-Si alloys is found to happen through three different processes. These processes may be labeled A, B and C, and appear during NA in the same order as listed below:

  Process A: Found to cause a positive effect on hardness during NA and after NA+AA with unknown effect on the microstructure. The clustering is likely to be associated with a low formation barrier, as it happens quickly, and according to previously reported results on cluster compositions it is likely related to Si-Si clustering.

  Process B: Found to cause a major increase in hardness during NA, and a decrease in hardness after NA+AA. The process is observed to cause a major coarsening in microstructure after AA, and it is this that causes the lowering in strength of the material. The clustering is likely to be associated with a low formation barrier, as it happens quickly, and according to previously reported results on cluster compositions it is likely related to Mg-Mg clustering.

  Process C: Found to cause an increase in hardness both during NA and after NA+AA. As the clustering reaction is slow, it is likely to be associated with a relatively high energy barrier, causing the resulting clusters to become more stable than those formed in the quick processes A and B. The more stable product of the reaction is, however, likely to eventually dominate the microstructure, forcing less stable complexes to dissolve or transform into such phases. By comparing to previously reported results on cluster compositions, this reaction is likely to be related to Mg-Si clustering.

- A new precipitation sequence is suggested, adding the three above processes in an early part of the sequence. As the three clustering processes can overlap, the clustering reaction that at any stage dominates the alloy microstructure is written in boldface:

$$\begin{aligned} &\text{SSSS} \rightarrow \textbf{Si clusters} \rightarrow \text{Si clusters}, \textbf{Mg clusters} \\ &\rightarrow \text{Si clusters}, \text{Mg clusters}, \textbf{Mg-Si clusters} \\ &\rightarrow \text{GP zones} \rightarrow \beta'' \rightarrow \beta', U_1, U_2, \text{B}' \rightarrow \beta/\text{Si} \end{aligned} \quad (2)$$

- The precipitate types formed during AA are found to be independent of NA. For the investigated heat treatment of 1 hour SHT at 540°C and 36 hours at 175°C the resulting precipitate types are dominated by β".

References

[1] M. H. Jacobs.
The structure of the metastable precipitates formed during ageing of an Al-Mg-Si alloy . *Philosophical Magazine*, 26:1–13, 1972.

[2] G.A.Edwards, K. Stiller, G.L Dunlop, and M.J Couper.
The Composition of Fine-Scale precipitates in Al-MgSi-Alloys. *Materials Science Forum*, 217-222:713–718, 1996.

[3] S.J. Andersen, C.D. Marioara, R. Vissers, M. Torsæter, R. Bjørge, F.J.H. Ehlers, and R. Holmestad.
The Dual Nature of Precipitates in Al-Mg-Si Alloys. *Materials Science Forum*, 638-642:390–395, 2009.

[4] R. Holmestad, C.D Marioara, F. Ehlers, M. Torsæter, R. Bjørge, J. Røyset, and S.J Andersen.
Precipitation in 6xxx aluminum alloys. *Proceedings of the 12th International Conference on Aluminium Alloys, Yokohama, Japan, September 5-9*, 1:30–39, 2010.

[5] John Banhart, Cynthia Sin Ting Chang, Zeqin Liang, Nelia Wanderka Matthew D. H. Lay, and Anita J. Hill.
Natural Aging in Al-Mg-Si Alloys - A Process of Unexpected Complexity. *Advanced Engineering Materials*, 12, 2010.

[6] M. Murayama and K. Hono.
Pre-Precipitate Clusters and Precipitation Process in Al-Mg-Si Alloys. *Acta Materiala*, 47:1537–1548, 1999.

[7] Jostein Røyset, Tore Stene, Jan Anders Sæter, and Oddvin Reiso.
The Effect on Intermediate Storage Temperature and Time on the Age Hardenable Response of Al-Mg-Si Alloys. *Materials Science Forum*, 519:239–244, 2006.

[8] C.D Marioara, S.J Andersen, J. Jansen, and H.W Zandbergen.
The influence of temperature and storage time at RT on nucleation of the β'' phase in a 6082 Al-Mg-Si alloy. *Acta Materialia*, 51:789–796, 2003.

[9] C.S.T.Chang, I. Wieler, N. Wanderka, and J. Banhart.
Positive effect of natural pre-aging on precipitation hardening in Al-0.44 at%Mg-0.38 at% Si alloy. *Ultramicroscopy*, 109:585–592, 2009.

[10] John Banhart, Cynthia Sin Ting Chang, Zeqin Liang, Nelia Wanderka Matthew D. H. Lay, and Anita J. Hill.
The Kinetics of Natural Ageing in 6000 Alloys - a Multi-method Approach. *Proceedings of the 12th International Conference on Aluminium Alloys, Yokohama, Japan, September 5-9*, 1:381–388, 2011.

[11] I. Kovacs, J. Lendvai, and E. Nagy.
The Mechanism of Clustering in Supersaturated Solid Solutions of Al-Mg_2Ai Alloys. *Acta Metallurgica*, 30:975–983, 1972.

[12] I. Dutta and S.M. Allen.
A clorimetric study of precipitation in comercial aluminium alloy 6061. *Journal of Materials Science Letters*, 10:323–326, 1991.
[13] G.A.Edwards, K. Stiller, and G.L Dunlop.
APFIM investigation of fine-scale precipitation in aluminium alloy 6061. *Applied Surface Science*, 76/77:219–225, 1994.
[14] M. Murayama, K. Hono, M. Saga, and M. Kikuchi.
Atom probe studies on early stages of precipitation in Al-Mg-Si alloys. *Materials Science and Engineering A*, 250:127–132, 1998.
[15] F. De Geuser, W. Lefebvre, and D. Blavette.
3D atom probe study of solute atoms clustering during naturaal aging and pre-aging of an Al-Mg-Si alloy. *Philosophical magazine Letters*, 86:227–234, 2006.
[16] Malin Torsæter, Williams Lefebvre, Sigmund Andersen, Calin D. Marioara, John C. Walmsley, and Randi Holmestad.
Clustering Behaviour in Al-Mg-Si Alloys Investigated by APT. *Proceedings of the 12th International Conference on Aluminium Alloys, Yokohama, Japan, September 5-9*, 1:1385–1390, 2010.
[17] D. A. Porter, K. E. Easterling, and M. Y. Sherif.
Phase Transformations in Metals and Alloys. CRC Press, 3^{th} edition, 1961.
[18] A.K Gupta and D.J Lloyd.
Study of Precipitation Kinetics in a Super Purity Al-0.8 Pct Mg-0.9 Pct Si Alloy Using Differential Scanning Calorimetry. *Metallurgical and Materials Transactions A*, 30:879–884, 1999.
[19] C.S.T.Chang and J. Banhart.
Low-Temperature Differential Scanning Calorimetry of an Al-Mg-Si Alloy. *Metallurgical and Materials Transaction A*, 10, 2011.
[20] J. Banhart, M.D.H Lay, C.S.T Chang, and A.J Hill.
Kinetics of natural aging in Al-Mg-Si alloys studied by positron annihilation lifetime spectroscopy. *Physical Review B*, 83:014101, 1–13, 2011.